



POLITECNICO DI TORINO
MASTER THESIS

**A Thermomagnetic Energy Harvester
CERES PROJECT**

Candidate:
Fabio MATTIUSI

Supervisor:
Prof. Alessandro CHIOLERIO

Advisor: Prof. Candido Fabrizio PIRRI

Co-Advisor: Prof. Matteo COCUZZA

Collegio di Ingegneria Elettronica, delle Telecomunicazioni e Fisica

Master of Science
in
Micro and Nanotechnology for Integrated Systems
within the

IIT - Istituto Italiano di Tecnologia

Academic Year 2017-2018

“Energy and persistence conquer all things.”

Benjamin Franklin

“If you want to find the secrets of the universe, think in terms of energy, frequency and vibration.”

Nikola Tesla

“We both step and do not step in the same rivers. We are and are not.”

Heraclitus of Ephesus

Acknowledgements

First of all, I would like to thank Prof. Alessandro Chiolerio for offering me the great opportunity of carrying out the present master thesis at the Center for Future Sustainable Technologies within the Istituto Italiano di Tecnologia of Turin, for his guidance and support and for his esteem for me.

Then, I would like to specifically thank Erik Garofalo for his patience and kindness in helping me with every technical issue within the creation of the CERES Lab at IIT-Turin. For sure, without his knowledge, all the experimental activities related to CERES Project would have been impossible.

I would also thank all other people working at IIT-Turin, that in some way helped me during these 6 months of master thesis.

In particular, I really want to extend my gratitude to my Family, for allowing me to pursue my dreams undertaking this incredible and unique experience around Italy, France and Switzerland. For your continuous moral and economic support, thank you. Special thanks to my mother which always encouraged me and praised me in every step of this travel started almost 5 years ago, and especially during the years of the Master's Degree for all the times I thought I was not to be good enough. Actually this important achievement owes a little to her!

From the depths of my heart, thank to my girlfriend Carlotta, for all her love, patience and kindness to support and motivate me, during the entire period far from her.

To all the people, friends and not, which stayed beside me and participated with their respect along all my university life: thank you, your encouragement made me more determined.

To all the students, now true friends, found during this experience!

Abstract

The present Master Thesis work is a dissertation on the prototyping of the first ever demonstrated closed-loop direct thermomagnetic energy harvester. The research programme (CERES Project) has been conducted within the Center for Sustainable Future Technologies (CSFT) at Istituto Italiano di Tecnologia (IIT) of Turin. The three main phases reported here are: first, a description of the context and the physical background of this device, then, the experimental setup of the prototype, and finally, the analysis of the data collected during the first experiments. Moreover, a new matrix representation of the physical quantities involved is presented.

The CERES paradigm exploits the incredible thermomagnetic properties of ferrofluids, a suspension of magnetic nanoparticles dispersed in a fluid solvent. Since their magnetization is dependent on temperature, the interaction between a magnetic field and thermal gradients produces cycling magnetic forces, convertible into electric energy.

The experimental phase dealt first with the setup of a lab-scale first prototype of the CERES reactor, which features a toroidal geometry. In particular, the electronics needed to power up the system, starting from a power supply chain constituted of 8 suppliers. The latter were connected to two consecutive stages of 32 voltage regulators each: the first ones dropped the DC output voltage of the supplier from 12 V to 5 V, while the second ones dropped the voltage from 5 V to 2.3 V. In this way, it was possible to switch on all the 32 Peltier modules, that generate the thermal gradient among the inner and outer walls of the reactor, obtaining a hot side and a cold one. For what concerns the magnetic field, it was originated by more than 50 permanent magnets, placed near the Peltier cells of both inner and outer walls.

The second phase involved the implementation of a 16 measurements stations around the toroid. In details, 16 thermocouples were used to monitor and measure the temperature of the ferrofluid, and 16 thermistors (8 for each side) were used to monitor the wall temperature of both sides. Furthermore, all these devices were connected to a DAQ system by National Instruments®, coupled with a LabView™ software. Then, in order to collect the electrical energy obtained as output, the whole toroidal structure has been wrapped-up with a large number of coils, transforming the reactor in a sort of giant solenoid, able to exploit the magnetic field originated by moving NPs.

The third phase consisted of data collected in the previous phase, with a particular attention to the electrical (inductive and resistive) characterization of the extraction coils. From their analysis it was possible to notice the presence of interesting effects, like the increase of coils inductance when a small amount of FF was added to the reactor, together with a consequent reduction in the current extracted. Furthermore, almost all these phenomena reported an harmonic response, that could strongly confirm the CERES paradigm after future deeper analyses. In any case, the electrical power extracted from the system achieved a value of 12.64 μ W, and will be increased working with higher amounts of FF and improving the heat transfer characteristics of the CERES walls.

To conclude, the CERES system showed very interesting results, especially considering how innovative the system is and the short time over which this work was dedicated. However, in the next prototypes, these outstanding results can only be improved and spread over a large number of human applications.

Contents

Acknowledgements	iii
Abstract	v
1 Introduction	1
1.1 Introduction on waste energy	1
1.2 Introduction on CAS Systems	4
1.2.1 The DOUGHNUT	4
1.2.2 Some introductory definitions	4
1.3 Physical background of a CERES system	5
1.3.1 Magnetocaloric effect	5
1.3.2 Gibbs Free Energy	6
1.3.3 Ferrofluids	18
1.3.4 Gravitational Effects on Ferrofluids	21
1.4 Fluctuation Theorem	24
1.4.1 The Phase Space	25
1.4.2 Liouville Derivation of FT: the Transient Fluctuation Theorem	26
1.4.3 FT experimental demonstration	26
1.5 Exergy	29
1.5.1 Exergy concept	29
1.5.2 Exergy content in materials	30
1.5.3 Efficiency of exergy conversions	31
1.5.4 Exergy and information theory	32
1.5.5 Exergy, Information Theory and Fluctuation Theorem	33
1.5.6 Exergy in systems far from equilibrium	33
1.6 Conclusions	34
2 Experimental Setup	35
2.1 General Overview	35
2.2 FF: magnetism and properties	35
2.2.1 Magnetism	35
2.2.2 Constant volume	36
2.2.3 Pressure	36
2.2.4 Nanoparticles	37
2.3 CERES Reactor	40
2.3.1 Magnets	41
2.3.2 Peltier Modules	42
Peltier Effect	43
Seebeck Effect	43
Thomson Effect	44
2.4 Power Supply System	45

2.4.1	Power Supplies	45
2.4.2	1st Stage Voltage Regulators	46
2.4.3	2nd Stage Voltage Regulators	46
2.5	Extraction System	48
2.5.1	The Faraday's Law	48
2.5.2	Coils	50
2.5.3	Output Voltage Measurement System	52
2.6	Sensors	53
2.6.1	Thermocouples	53
2.6.2	Thermistors	55
2.7	Data Acquisition System	58
2.7.1	Hardware	58
2.7.2	Software	59
3	Data Analysis	63
3.1	General Overview	63
3.2	Thermal response of CERES system	63
3.2.1	Peltier modules directly polarized	63
3.2.2	Peltier modules inversely polarized	65
3.3	Impedance behaviour of CERES system	67
3.3.1	Inductive behaviour	67
3.3.2	Resistive behaviour	69
3.4	Current behaviour of CERES system	72
4	Conclusions	75
4.1	Efficiency of CERES system	75
4.2	Future optimizations of CERES 1.0 system	77
4.3	Future optimizations of CERES 2.0 system	78
A	Insights about physical background	79
A.1	Energy harvesting from FFs	79
A.2	Molecular Dynamics	82
A.3	Derivation of exergy	83
	Bibliography	87

List of Figures

- 1.1 The essential components necessary for the WHP energy recover technology [1]. 2
- 1.2 Percentages describing the amounts of technical potential (in MW) present in WHP, for different temperatures [4]. 2
- 1.3 Graphical representation of the Carnot efficiency η as a function of the temperature difference ΔT (here in $^{\circ}\text{C}$). It is possible to observe that the efficiency drastically drops at low values of temperature difference, while the maximum is reached at higher ΔT [1]. 3
- 1.4 Diagram depicting the magnetic-refrigerating cycle, where the heat is transferred from the central heat load towards the external environment. Starting from the top-left, the sample is at thermal equilibrium with the surrounding and the magnetic dipoles are randomly oriented, since no magnetic field is present; then a magnetic field is switched on, and the sample starts heating up, while the dipoles become aligned in the direction of the applied field. After the heat is transported to the surrounding environment by means of a heat-transfer medium (the dipoles are still aligned), but when also the magnetic field is removed, the dipoles orientations randomize, which translates into a further temperature reduction of the sample (below the temperature of the thermal bath). Possible heat-transfer materials are water, or for very low temperatures, He [8]. 5
- 1.5 Magnetic specific heat for different magnetic materials: **a)** $\text{LiNi}_2\text{P}_3\text{O}_{10}$ antiferromagnet for various applied magnetic field [23]. **b)** Ferrimagnetic MnCr_2S_4 single crystals under magnetic fields of different intensity [24]. **c)** Ferrimagnetic Fe_3Se_4 nanorods under magnetic fields of 20 kOe and 50 kOe and no applied field [25]. **d)** Normalized C_M for $\text{UAs}_{0.8}\text{Se}_{0.2}$, where the peaks at $T = 125$ K are insensitive to the magnetic field, while C_M at $T = 50$ K depends on the applied field [26]. 13
- 1.6 Magnetic specific heat of nanometric magnetite (black) and bulk magnetite (red) [27] [28]. The nano-magnetite shows no anomaly at Verwey transition, a low temperature (120 K) transition [29]. 13
- 1.7 Theoretical magnetic entropy variation due to the removal of a magnetic field of 10 kOe for systems with different arrangements of 7/2 spin atoms [32]. 15
- 1.8 **a)** Behaviours of ferromagnetism (blue), paramagnetism (green) and superparamagnetism (red). The latter shows the absence of both coercive and residual magnetic fields, contrary to what happens in the ferromagnetic behaviour. **b)** Behaviour of the coercive field H_c against the particle size [35]. 16
- 1.9 **a)** Behaviour of the ZFC and FC curves. **b)** Behaviour of the blocking temperature plotted against the applied magnetic field [36]. 16
- 1.10 Computed reduced ΔS_M as a function of $x = \mu_c H / (k_B T)$ with different dilution levels (numbers near the curves) of the magnetic clusters by the non-magnetic particles [37]. 17

1.11	Basic schematics of different FF energy harvesters: a) Peristaltic energy harvester [40]. b) FF harvester based on a springless proof mass and FF used as lubricant [41]. c) FF harvester based on the vaporization of the FF fluid to get the varying magnetic field [42]. d) FF harvester based on shaped magnetic cone with a conduit containing the FF coiled around it [42].	19
1.12	Basic schematic of the FF based energy harvester [43]: a) FF in absence of a magnetic field (dipoles are randomly oriented). b) FF in presence of a magnetic field (dipoles are aligned with the magnetic field). c) FF in presence of two permanent magnets (upper and lower), generating a magnetic flux across the wounded coil and an induced electric current transformed into an electric voltage drop by means of the load resistance.	19
1.13	Different responses (magnetic induction and frequency) according to varying height of the liquid [43]: a) Behaviour of the magnetic induction distribution inside the FF liquid. b) Behaviour of the modal frequencies f_{11} and f_{12} plotted against the liquid height (it is possible to notice how the frequency decreases with h).	21
1.14	Parametric map (left-side) and wavenumbers (right-side) relative to an infinite vertical layer of FF; the mixed gravitational and magnetic convection, vertical magneto-convection and thermo-magnetic convection are represented with a solid, dashed and dotted-dashed lines, respectively [46].	23
1.15	Thermo-gravitational flow when the magnetic field is zero [47]: on the left, a simple schematic view, while on the right the infrared image of a textolit wall; the temperature gradient between the textolit and aluminium walls is 40 °C.	23
1.16	Thermo-magnetic flow appearing inside a homogeneous magnetic fluid in presence of a magnetic field $H = 35$ kA/m is applied orthogonally to the image plane [47]: a schematic view (left) and the relative infrared image of the textolit wall (right). The thermal gradient between the textolit and aluminium walls is 40 °C.	24
1.17	Illustration of the phase space [52], showing the trajectories $\Gamma(t)$ starting at volume δV , and the corresponding antitrajectories $\Gamma^*(t)$ starting at δV^* ; the coordinates (\vec{q}, \vec{p}) are represented together with time t	25
1.18	Histogram representing the number of trajectories versus the dimensionless mean entropy production Ω_t/t . The experimental set consists of 540 trajectories of colloidal particles held in the optical trap at times $t = 10 \times 10^{-2}$ s (black bars) and $t = 2.0$ s (grey bars) after the initiation of the translation stage. Bin size is unitary: $\Omega_t/t = 1.0$ [50].	28
1.19	Exponential decreasing curve representing the number the ratio of produced entropy over the consumed entropy (left-hand of Equation 1.49) and the average entropy production (right-hand of Equation 1.49), both plotted against the time t . The results agree with the IFT [50].	28
1.20	The moving force related to the energy/matter flow is the quality, which continuously deteriorate while the flow goes on; in this way a precise direction in space and time can be defined. It is possible to observe that only a small part of the flowing energy is stored inside the system (equilibrium condition between the input and output energy/matter) [53].	29
1.21	The system A , at temperature T_0 and energy flow P [53].	33

2.1	Different types of magnetism in materials: A) In paramagnetism the magnetic moments are randomly aligned in absence of a magnetic field (this is also the case of ferromagnets above T_C); B) Ferromagnetism show all moments aligned and with the same intensity in absence of a magnetic field (or is the case of paramagnets in presence of an external magnetic field); C) Antiferromagnetism presents magnetic domains aligned in opposite direction, but with the same intensity, so that the total resulting magnetization is null; D) Ferrimagnetism is similar to antiferromagnetism, but in this case the opposite magnetic moments have different amplitudes, and consequently the resulting magnetization is not zero [58].	35
2.2	Theoretical and experimental FF pressure plotted against the distance of the permanent magnets [62].	37
2.3	Graphical representation of two interacting NPs, with radius R and reciprocal distance d_c between their centres [65].	38
2.4	Normalized size distribution of Fe_2O_3 particles. After the normalization, $w(R)dR$ is equal to the volume fraction of particles with radius R [65].	39
2.5	The CERES reactor: virtual rendering and real system.	40
2.6	The chemical structure of the PLA [66].	40
2.7	One of the ALNICO magnets, successively installed all around the CERES ring.	41
2.8	The power supply SPD 3606 by GW-INSTEK, used to push the motion of the FF at early stages.	42
2.9	The Peltier module that is used for the CERES Project; a module is composed of many junctions in series.	42
2.10	A scheme representing how the Peltier effect acts, considering n-doped and p-doped semiconductors: applying a voltage, it is possible to heat and cool the two sides of the module [68].	43
2.11	A scheme representing how the Seebeck effect acts, considering n-doped and p-doped semiconductors: applying a thermal gradient (heat and cool sides), it is possible to generate an induced electromotive force [68].	44
2.12	Here are reported some Seebeck coefficients for both metals and semiconductors [69].	44
2.13	The power supplies from Bel used for CERES Project, united in groups of 4, front-side and back-side.	45
2.14	Examples of voltage regulators LM7805 by Fairchild.	46
2.15	On the right, the ADP7157 linear voltage regulators standalone with the exposed pad (front-side and back-side), and on the left, one linear regulator soldered on the socket.	46
2.16	The schematic of the circuit implemented: the output of the power supply (12 V) is the input of the LM7805 (first stage of voltage regulators), which reduces the input voltage to 5 V (VOUT_1 in the schematic). At this point, the second stage of linear voltage regulators (ADP7157) lowers the 5 V at its input (VIN in the schematic) to 2.34 V (VOUT_2 in the schematic). The voltage divider, made by resistors $R = 10 \text{ k}\Omega$, adjusts the output voltage at the desired value. Moreover, the five capacitors $C = 10 \text{ }\mu\text{F}$ are required to have low noise.	47

- 2.17 The real implementation on a breadboard of the circuit reported in the schematic of Figure 2.16. It is possible to notice the two resistors, the five capacitors, the LM7805 with its dissipator (behind) and the ADP7157 mounted on its IC socket. In addition, the coloured jumpers are used to make the circuitry connections. Here, the cables coming from the power supply are missing just for clarity reasons. 47
- 2.18 The apparatus realized by Micheal Faraday for the first public demonstration of his experiment [70]. The left side wire is connected to a battery, while the right one is plugged to a voltmeter, in order to measure the induced EMF on the right wire. 48
- 2.19 The magnetic flux $\vec{\Phi}$ across closed surface Σ . $\vec{\Phi}$ is proportional to the number of lines of force of \vec{B} (the red arrows), the magnetic flux density, passing through Σ . As a consequence, the magnetic flux changes if the magnetic flux density varies, or if the surface reduces or enlarges. A further possibility is to tilt the surface, or better, change the angle θ between the field \vec{B} and the versor orthogonal to the surface Σ [73]. 49
- 2.20 The coils are rolled up along the entire ring, in the free space among two adjacent Peltier stations; moreover the coils were tilted a little bit in order to have a better coupling between the magnetic field and the coils, resulting in a greater induced EMF. Moreover, it is possible to notice three layers of coils in the poloidal direction (red cables), and one in the toroidal direction (black cable): one red cable and the black one will be used to give an additional push to the FF at starting motion, while the remaining red cables will be connected in series and then to the output measurement system. 50
- 2.21 A graphical representation of the magnetic field created inside a solenoid with $N = 7$ coils. It can be seen that the magnetic field intensity is bigger inside the coils (lines of force are quite dense), while outside decreases drastically, thus, increasing the length of the solenoid, the confinement of the \vec{B} field is better. Furthermore, inside the solenoid the lines of force related to the magnetic field are parallel. Image taken from [70]. 51
- 2.22 The Agilent E4980A LRC meter, with band-pass from 20 Hz to 2 MHz, and used to measure the inductive, capacitive and resistive behaviours of the extraction coils; in addition, the Agilent test fixture 16047A is inserted, in order to have a better coupling between coils and instrument. 52
- 2.23 The Keithley 2635A, a source meter used to measure the intensity of the current induced by EMF, and flowing across the extraction coils. 52
- 2.24 The circuitual representation of a traditional thermocouple. On the left it is possible to notice the so called *hot junction*, where the temperature is effectively measured, while the junction of Metal 1 and Metal 2 with the copper are said *cold junctions* and are used as reference temperature. This part of the thermocouple is connected with copper wires to the voltmeter, and the measured voltage can be translated into a corresponding temperature. In addition, assuming $T_{sense} > T_{ref}$, the positive electrode is listed firstly, followed by the negative one. Image taken from [70]. 53
- 2.25 The characteristic functions of some most used thermocouples. 54
- 2.26 One of the thermocouples used for the CERES system. A glass fibre acts as an insulator between the two wires; in addition, the pink plug is removed in each device to have a better connection with the DAQ Acquisition System. 54

- 2.27 The Peltier module was calibrated immersing the sensor into hot water ($\approx 100^\circ\text{C}$), and measuring the corresponding voltage ($\leq 2\text{ mV}$); the process was repeated until the water became cold ($\approx 0^\circ\text{C}$), where the voltage dropped to few hundreds of μV . All 16 thermocouples (TCs) followed this procedure, and the relative voltage values were plotted here. As can be seen, the voltage response of these thermocouples can be treated as strictly linear. 55
- 2.28 A picture of thermistor ND03N00103KCC by AVX (sold by RS), installed around the outer wall of the CERES ring. 56
- 2.29 A picture showing the typical response of a thermistor; in this case a NTC example is reported, since the resistance decreases with temperature. 56
- 2.30 A circuitual representation of the connection between the thermistor and the DAQ system, used for the acquisition of the temperature values. A dedicated channel of DAQ provides 5 V , then, the potential difference on the thermistor is read thanks to a voltage divider between a resistance $R = 10\text{ k}\Omega$ and the thermistor itself. 57
- 2.31 A picture of NI 6289 DAQ acquisition system used. 58
- 2.32 The Block Diagram window with the software realized in LabView. 60
- 2.33 An alternative view of the Front Panel window, where the data collecting in real time are substituted by graphs made with Matlab. The graphs show an entire acquisition lasted around 21 h: the upper ones refer to thermistors (TR), while the bottom ones to thermocouples (TC). 61
- 3.1 The average temperatures reached by the walls and the FF in DP (**D**irect **P**olarization). In blue the average of thermistors 1-8 (Outer Wall Temperatures, or OWT), in red the average of thermistors 9-16 (Inner Wall Temperatures, or IWT), in green the average of thermocouples 1-8 (Outer Fluid Temperatures, or OFT), and in black the average of thermocouples 9-16 (Inner Fluid Temperatures, or IFT). The first decrease on the left corresponds to the switching on of the medium fan (Peltier modules are turn-off), while the consequent rapid increase (point 1) is related to the switching on of the Peltier stations; the red curve reduces its temperature after the placement of the small fan at the center of the reactor, obtaining in this way a better thermal gradient on the walls (point 2). Point 3 represents the automatic switch off of the air conditioning, while point 4 indicates the air conditioning switched on. Other increases/reductions are mainly due to fluctuations in the automatic air conditioning of the lab. 64
- 3.2 Thermal gradients with Peltier modules used in DP. 65
- 3.3 The average temperatures reached by the walls and the FF in IP (**I**nverse **P**olarization). In blue the average of thermistors 1-8 (Outer Wall Temperatures, or OWT), in red the average of thermistors 9-16 (Inner Wall Temperatures, or IWT), in green the average of thermocouples 1-8 (Outer Fluid Temperatures, or OFT), and in black the average of thermocouples 9-16 (Inner Fluid Temperatures, or IFT). Point 1 represents the power on of Peltier modules, point 2 indicates the removal of the small fan from the center of the reactor, point 3 and 4 correspond to the turnin on and off (respectively) of the automatic air conditioning of the lab. The big decrease (point 5) corresponds to the switching off of the electronics (except the temperature sensors), while the subsequent rapid increase (point 6) relates to the new switching on of the Peltier modules (Figure 3.5 better represents this transient). 65
- 3.4 Thermal gradients with Peltier modules used in IP. 66

3.5	Thermal transients with Peltier modules used in IP.	66
3.6	The result of the addition of 1 mL of FF EFH1 inside the reactor filled with 1 L of water. It is clearly evident the presence of a straight step of the inductance measured on the extraction coil, moving from 54.87 μH to 54.91 μH , and saturating around 54.92 μH . Moreover, the experiment is done by giving a push to the added FF, by turning on the poloidal (inversely polarized with 1.85 A and 5 V) and toroidal (directly polarized with 3.10 A and 5 V) coils with a DC current generator.	67
3.7	The behaviour of the inductance in semilogarithmic scale. With this graphical representation, the initial stages can be observed in a better way: in particular, it can be noticed that signal is very stable around 54.94 μH , than it becomes a little bit perturbed by the power on of Peltier stations, successively the DC current starts flowing into the coils and the series inductance makes a decrease following a precise straight line, which slope drastically changes around 1000 s; in the end the signal stabilizes near 54.86 μH . The reasons of the first line must be searched in the Seebeck effect, influencing the electrical parameters of cables when their extremities are subjected to a thermal gradient, but becoming negligible in short time due to the high thermal conductivity of wires. The explanation of the second slope could more difficult, but a possible solution is to consider this variation as a result of the heating FF inside the reactor, which probably requires a certain time to initiate its cyclic motion. When the motion is completely set up, the inductance remains constant at the new value.	68
3.8	The inductive behaviour after one night of continuous acquisition; it is possible to see that the inductance stays almost constant, except in the initial and final stages.	69
3.9	The measure starts when the signal stabilizes, reaching a resistance value of 1.10 Ω ; then, the Peltier modules and the DC generator are powered up, so that the resistance rapidly increases (600 s, point 1), and 100 s after, the resistance variation attenuates, saturating near 1.22 Ω (point 2).	69
3.10	Resistive behaviour of CERES system when perturbed by hand agitation. Two spikes are present, and are related to the agitation introduced with the hands. The higher one corresponds to an agitation with the same direction of the FF motion, the smaller one relates to an agitation opposite with respect to motion.	70
3.11	Resistive behaviour of CERES system for a long measurement time. After the initial variations (due to hands agitation), the resistance shows a very slow transient towards 1.105 Ω	71
3.12	Resistive behaviour of CERES system with particular fluctuations after the addition of 1 mL of FF, around 600 s. The red curve is obtained by smoothing the scatter plot with Savitzky–Golay method, while the blue curve show a sinusoidal fitting. The green lines shown instead the temporal distance among successive peaks.	71
3.13	Graphical representation of an inverse chirp function drawn over the fluctuations appeared in the CERES system, after the addition of 1 mL of FF.	72
3.14	Behaviour of the current, after the addition of 2 mL of FF inside the reactor. The current drop is well visible at 750 s (point 1) and 890 s (point 2). Looking better, it is possible to distinguish two minor current drops at point 3 and point 4.	73
4.1	Equivalent circuits of the coils wrapped around the CERES system.	75

4.2	Graphical representation of a simple circuit involving an impedance Z containing DC and AC resistance terms, and EMF as voltage source.	76
4.3	Graphical rendering of a futuristic new geometry of CERES reactor.	78
A.1	Output voltage vs frequency responses curves for different parameters [43]: a) Varying the height, a constant output electric potential is got in all cases, but the peaks shift little towards left; 1 in=2.54 cm. b) Reducing the magnetic field, different output electric potentials are obtained and peaks shift towards left, for negative field. c) Increasing the mechanical excitation (acceleration), an greater output voltage is reached, with peaks little shifting towards left.	80
A.2	Distribution of the magnetic induction inside the liquid, according to three different situations a) , b) and c) [43].	81
A.3	Considering a frequency of 9 Hz and two acceleration levels (2.5 m/s^2 and 3 m/s^2), the following graphs are obtained [43]: a) Output voltage vs frequency showing the higher values of V_{out} obtained when the container is tilted by 90° , to increase the liquid surface. b) Power vs resistance curves indicate the presence of power peaks corresponding to an optimal resistance value.	81
A.4	The MD simulations for 343 500 simulated trajectories show a behaviour very similar to the experimental one depicted in Figure 1.19. The figure on the top-right represents the trapped particle (black filled circle) enclosed between the impenetrable walls, while the coloured shaded zone denotes the optical trap [50].	83
A.5	Behaviour of the ratio between entropy producing trajectories over entropy consuming trajectories from a set of 310 000 MD simulations [50].	83
A.6	The system A , with its parameters and the surrounding environments A_0 with its properties [53].	84
A.7	The system A , with its parameters placed inside a local system A_L , enclosed at its time within the surrounding environments A_0 with its properties [53].	86

List of Tables

1.1	Possible waste heat sources (left), and applications (right) [1].	3
1.2	Sum-up table of some interesting magnetic heat capacity values from Figures 1.5-1.6.	12
1.3	Here are reported the different quality values (fraction in percentage of Extra Superior Energy of total energy in question) for several energy forms, ordered from the one with the highest content of exergy towards the one with the lowest exergy content, which corresponds to the heat radiated from the Earth [53]. . .	30
1.4	Here are reported the quality values (computed from Equation 1.56) for different matter structures, ordered from the one with the highest content of exergy towards the one with the lowest exergy content [53].	30
2.1	The Curie temperatures of different ferromagnetic materials [59].	36
2.2	Density values for megnetite/oleic acid aggregates for different increasing temperatures [61].	36
2.3	Properties of EMG 911 and EFH1 FFs by <i>Ferrotec</i> [63][64].	37
2.4	Main sizes of CERES structure.	41
2.5	Properties of thermistor ND03N00103KCC by RS-AVX [75].	56
2.6	Properties of DAQ NI 6289 by National Instruments [77].	58
4.1	Main properties of CERES 1.0.	77
A.1	Here are reported several forms of exergy according to different kinds of thermodynamic potentials [53].	86

List of Abbreviations

AC	Alternating Current
ALNICO	ALuminium-NICKel-CObalt
AM	Additive Manufacturing
CAD	Computer-Aided Design
CAS	Colloidal Autonomous System
CERES	Colloidal EneRgEtic System
COP	Coefficient Of Performance
DC	Direct Current
DP	Direct Polarization
DOUGHNUT	aDatptive cOLloidal accUmulatinG/HarvestiNg UniT
EMF	ElectroMotive Force
FDM	Fused Deposition Modeling
FF	FerroFluid
FT	Fluctuation Theorem
IC	Integrated Circuit
IFT	Integrated Fluctuation Theorem
IP	Inverse Polarization
MCE	Magneto-Caloric Effect
MD	Molecular Dynamics
NASA	National Aeronautics and Space Administration
NP	NanoParticle
NTC	Negative Temperature Coefficient
PLA	Poly-Lactic Acid
PTC	Positive Temperature Coefficient
WHP	Waste Heat to Power
TFT	Transient Fluctuation Theorem

Dedicated to my Family...

Chapter 1

Introduction

1.1 Introduction on waste energy

In the United States, more than one third of all energy used in the country is related to the only industry, which corresponds to about 1.06×10^{19} J and consequently to a CO₂ emission around 1.68×10^{12} kg [1]. On the other side of the Atlantic Ocean, in Europe, the energy consumption in the industrial sector was 1.73×10^{19} J in 2015 [2] and a relative total CO₂ emission around 0.36×10^{12} kg [3].

In order to reduce both the energy consumption and emission, two ways are present:

1. Improve the actual industrial processes (or change them) to have better energy efficiency;
2. Capture and reuse the waste heat, present in all industrial processes and corresponding to 20 % to 50 % of all the energy used.

Large part of heat is lost via heat conduction, convection and radiation from hot machineries (or products), but especially it is dissipated from streams of hot exhausted gases and liquids (Table 1.1). The possible improvements of WHP (**W**aste **H**eat to **P**ower) technology can arise the energy efficiency from 10 % to 50 %. The three main components of this technology are the following ones, and clearly depicted in Figure 1.1:

1. Source of waste heat;
2. Recovery technology;
3. Use of the recovered energy.

The feasibility to recover the waste heat depends on some parameters, both related to the stream and heat to be transferred:

- heat quantity;
- heat temperature/quality;
- minimum allowed temperature;
- other logistic operations.

Starting from the first one, the heat quantity (amount of energy contained in a waste heat stream) can be derived by:

$$E = m \cdot h(t) \quad (1.1)$$

where E represents the waste heat loss, m the waste stream mass and $h(t)$ the waste stream specific enthalpy (a function of the temperature).

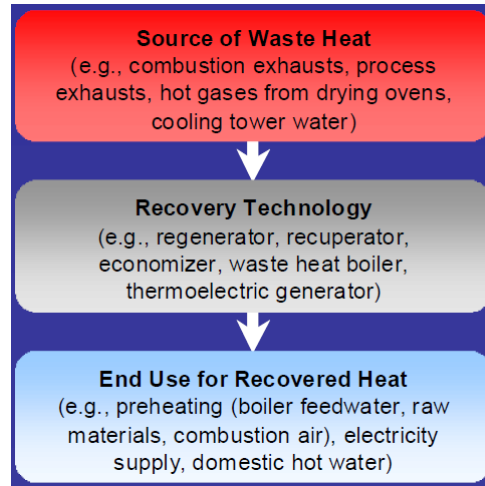


FIGURE 1.1: The essential components necessary for the WHP energy recover technology [1].

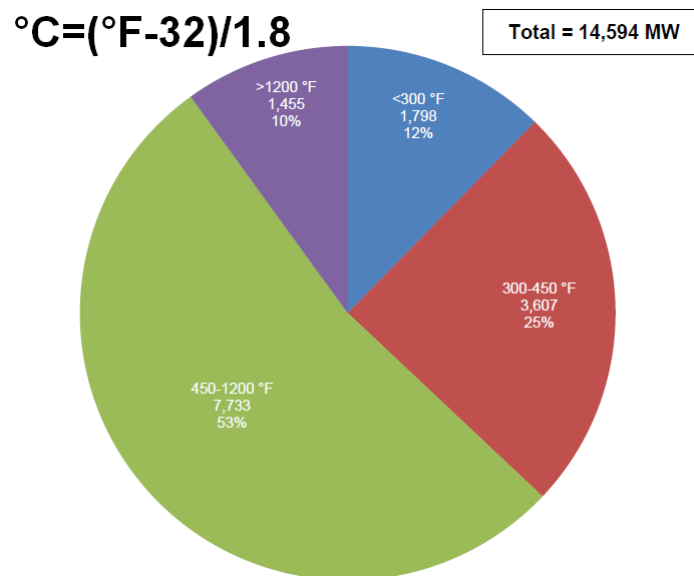


FIGURE 1.2: Percentages describing the amounts of technical potential (in MW) present in WHP, for different temperatures [4].

The heat quantity is an important parameter, but even more is the quality of the heat itself, increasing according to temperature T :

- Low quality: $T < 200\text{ }^{\circ}\text{C}$
- Medium quality: $200\text{ }^{\circ}\text{C} < T < 650\text{ }^{\circ}\text{C}$
- High quality: $T > 650\text{ }^{\circ}\text{C}$

The heat at low temperatures (and low quality) is present in very large quantities (60%), with respect to medium-high temperatures heat. However, the latter is able to produce the largest amount of technical potential (Figure 1.2), because of its higher heat quality. It is remarkable to remember that the power efficiency (or Carnot Efficiency) is based (and also limited) by the temperatures of the heat source and sink, as expressed by:

$$\eta = 1 - \frac{T_L}{T_H} \quad (1.2)$$

where T_H is the waste heat temperature, and T_L is the temperature of the heat sink. The behaviour of Equation 1.2 is reported in Figure 1.3.

Waste Heat Sources	Uses for Waste Heat
<p>Combustion Exhausts: Glass melting furnace Cement kiln Fume incinerator Aluminum reverberatory furnace Boiler</p> <p>Process off-gases: Steel electric arc furnace Aluminum reverberatory furnace</p> <p>Cooling water from: Furnaces Air compressors Internal combustion engines</p> <p>Conductive, convective and radiative losses from equipment: Hall-Heroult cells (reaction vessel for Aluminum smelting [5])</p> <p>Conductive, convective and radiative losses from heated products: Hot cokes Blast furnace slags</p>	<p>Combustion air preheating</p> <p>Boiler feedwater preheating</p> <p>Load preheating</p> <p>Power generation</p> <p>Steam generation for use in: Power generation Mechanical power Process steam</p> <p>Space heating</p> <p>Water preheating</p> <p>Transfer to liquid or gaseous process streams</p>

TABLE 1.1: Possible waste heat sources (left), and applications (right) [1].

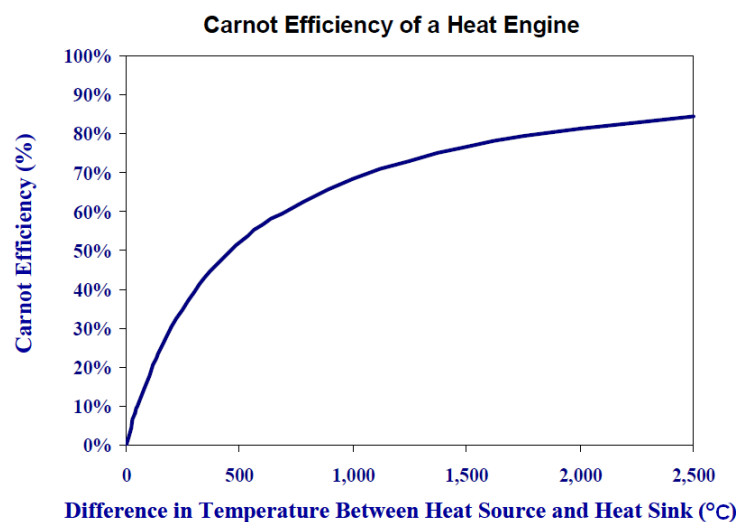


FIGURE 1.3: Graphical representation of the Carnot efficiency η as a function of the temperature difference ΔT (here in $^{\circ}\text{C}$). It is possible to observe that the efficiency drastically drops at low values of temperature difference, while the maximum is reached at higher ΔT [1].

In this energy recover environment, the most difficult part is the one related to save energy from heat waste at low temperatures; a possible solution could arrive from CERES systems, able to produce electric potential from gradients of temperature. In the next Sections these systems will be further analyzed.

1.2 Introduction on CAS Systems

CAS, or Colloidal Autonomous System [6], are colloidal devices, properly protected from the external harsh environment by a deformable skin, which are the most interesting promise in the field of modern and revolutionary robotics. They are totally different from the well-known and heavy robots used in the industrial processes, and include the main advantages coming from the soft-robotics, but with a look at improving their capabilities.

One of the supposed field of applications is the space exploration (from gas giant planets towards comets and asteroids), thanks to their autonomous systems coupled with energy harvesting/storage due to the smart fluids on which they are based. Other possible applications are the deepest zones of lakes and oceans, or post-disaster rescue searches, or even in surgery operations.

Another attractive characteristic is their ability in moving on unpredictable terrains, since they are liquid robots considered as adaptive platforms.

Furthermore, in order to develop a CAS which will work in an autonomous way, is necessary to integrate also an efficient energy harvesting system called CERES (Colloidal EneRgEtic System), based on a (ferro)fluid. The CERES idea should directly fulfill the NASA's challenge "Surviving Extreme Space Environments", while highly improving the current robotics and electronics state-of-the-art. As a consequence, the technical aim of this project is to identify the most efficient materials, structures and solutions to develop an autonomous and energy efficient system based on a fluid, and giving origin to the CERES itself.

1.2.1 The DOUGHNUT

The first step is to develop a prototype known as DOUGHNUT, or better a **D**aptive **c**olloidal **a**ccumulating/**H**arvesting **U**nit: this system is able to exchange only electromagnetic or thermal energy with the outer environment, enclosed inside a thin shell (acting as its skin), transparent to the type of energy which is being exchanged, and protecting at the same time the inner structures. The great adaptability of the system is due to its ability to reconfigure the internal components according to the energy nature and flux direction.

Moreover the CERES paradigm completely fulfils the survival in harsh space environments, one of the NASA's great challenges [6].

1.2.2 Some introductory definitions

In order to better understand the different concepts, here are reported some useful definitions used in the next pages:

- **Colloid**: "complex system lying between completely homogeneous systems (solutions) and completely heterogeneous systems (suspensions); it is composed by a fine phase dispersed in a solvent" [6].
- **Filler**: also known as dispersoid, is a particle with different chemophysical nature with respect to the carrier (*e.g.* the solvent).

- **Smart fluid:** collective liquid device with smart functionalities.
- **FF (FerroFluid):** is a colloidal suspension of magnetic NPs, or NanoParticles (there exist different states, according to the magnetic nature of the particle, like ferromagnetic or superparamagnetic).
- **CAS:** is constituted by different technologies, ranging from functional materials, in-situ instrument capability, energy storage, data processing, mobility and communication.

1.3 Physical background of a CERES system

1.3.1 Magnetocaloric effect

A magnetic colloidal fluid can thermodynamically couple magnetization and temperature, which is the basis of the so called MCE (**M**agneto-**C**aloric **E**ffect): briefly, a material heats up when placed in a magnetic field, while it cools down in absence of a the magnetic field. This effect was discovered for the first time by Emil Gabriel Warburg in 1881 [7], and is an intrinsic property of all materials; in case of a ferromagnetic material, it is possible to refer to the following refrigeration process, called adiabatic demagnetization (Figure 1.4). With this process, temperatures below 1 K can be reached, starting from cryogenic temperatures.

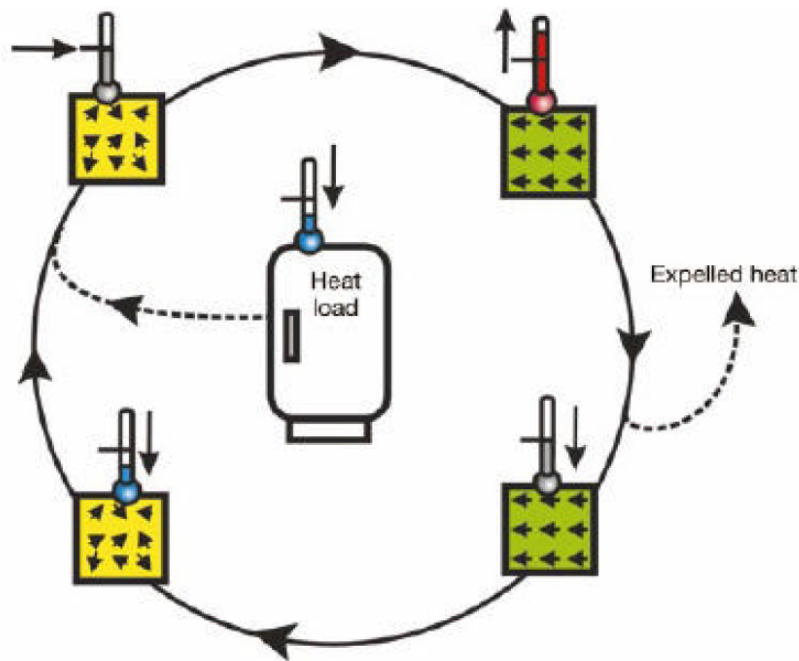


FIGURE 1.4: Diagram depicting the magnetic-refrigerating cycle, where the heat is transferred from the central heat load towards the external environment. Starting from the top-left, the sample is at thermal equilibrium with the surrounding and the magnetic dipoles are randomly oriented, since no magnetic field is present; then a magnetic field is switched on, and the sample starts heating up, while the dipoles become aligned in the direction of the applied field. After the heat is transported to the surrounding environment by means of a heat-transfer medium (the dipoles are still aligned), but when also the magnetic field is removed, the dipoles orientations randomize, which translates into a further temperature reduction of the sample (below the temperature of the thermal bath). Possible heat-transfer materials are water, or for very low temperatures, He [8].

1.3.2 Gibbs Free Energy

In thermodynamics, a system is fully described by its fundamental thermodynamic equation, also called Euler Equation [9]:

$$\begin{aligned} U(S, V, \mu, M, P) &= TS - pV - MH - EP + \mu_1 N_1 + \cdots + \mu_n N_n \\ &= TS - pV - MH - EP + \sum_{j=1}^n \mu_j N_j \end{aligned} \quad (1.3)$$

where here was treated a general case, considering a magnetic field and the chemical potentials of n different materials constituting the system; the physical quantities in Equation 1.3 are U the internal energy of the system, S the entropy of the system and M the magnetization of the magnetic sample, E the electric field, P its electrical polarization and μ the chemical potential of the chemical specie N .

It is remarkable to remember that the internal energy is a function of entropy S , volume V and magnetic and electric fields or, of the entropy, volume, magnetization and polarization (see Equation 1.4).

$$U = U(S, V, H, E) = U(S, V, M, P) \quad (1.4)$$

U can be rewritten into two differential forms, reported in Equation 1.5:

$$\begin{aligned} dU &= TdS - pdV - MdH - PdE \\ &= TdS - pdV - HdM - PdE \end{aligned} \quad (1.5)$$

If the five quantities of the following Equations 1.6a-1.6b-1.6c-1.6d-1.6e are known, they can be substituted into the Euler relation in order to obtain the complete information of the thermodynamic system considered.

$$p = p(S, V, \mu, M, P) \quad (1.6a)$$

$$T = T(S, V, \mu, M, P) \quad (1.6b)$$

$$N = N(S, V, \mu, M, P) \quad (1.6c)$$

$$H = H(S, V, \mu, M, P) \quad (1.6d)$$

$$E = E(S, V, \mu, M, P) \quad (1.6e)$$

If the system in question is paramagnetic, Equation 1.3 becomes:

$$U = NRT_0 \cdot \exp\left(\frac{S}{NR} + \frac{M^2}{N^2 M_0^2}\right) \quad (1.7)$$

At this point the Gibbs Free Energy, or Free Enthalpy of the system can be introduced. It is an important quantity to determine the thermodynamic properties of a (magnetic) system, eventually placed in a magnetic field H at absolute temperature T and pressure p ; as a consequence the Gibbs free energy G of the system is defined as in Equations 1.8a-1.8b:

$$G = U - TS + pV - MH - EP + \sum_{j=1}^n \mu_j N_j \quad (1.8a)$$

$$dG = Vdp - SdT - MdH - PdE + \sum_{j=1}^n \mu_j dN_j \quad (1.8b)$$

From the Euler equation it is also possible to move to Gibbs free energy [9], by means of the Equations below:

$$U = U(S, V, N) \quad (1.9a)$$

$$T = \frac{\partial U}{\partial S} \quad (1.9b)$$

$$-p = \frac{\partial U}{\partial V} \quad (1.9c)$$

$$G = U - TS + pV \quad (1.9d)$$

where it is clearly that variables U, V, S result in $G=G(T, p, N)$ (Equation 1.8b). It is remarkable to introduce here the Massieu equations (firstly derived by Massieu himself in 1869, before the ones developed by Gibbs in 1875 [9]), and which are very common in case of irreversible thermodynamics

$$S\left(\frac{1}{T}\right) = S - \frac{1}{T} = -\frac{F}{T} \quad (1.10a)$$

$$S\left(\frac{p}{T}\right) = S - \frac{p}{T}V \quad (1.10b)$$

$$S\left(\frac{1}{T}, \frac{p}{T}\right) = S - \frac{U}{T} - \frac{p}{T}V = -\frac{G}{T} \quad (1.10c)$$

Now it is possible to define another energetic parameter (already in Equation 1.10a), the so called Helmholtz Free Energy F , related to internal energy by Equation 1.11a, and used in case of systems with constant volume; in all other cases (with varying volume), the differential form of free energy is preferable applied (Equation 1.11b).

$$F = U - TS \quad (1.11a)$$

$$dF = -SdT - pdV - MdH - PdE \quad (1.11b)$$

On the other side, when the system is under constant pressure, the Gibbs free energy mentioned above is preferred. The equilibrium conditions can be analytically derived from the Gibbs representation [9], considering:

$$d^2G = d^2(U - TS + pV) = d^2U > 0 \quad (1.12)$$

and observing that the second derivative of Gibbs free energy are concave for both temperature and pressure:

$$\left(\frac{\partial^2 G}{\partial T^2}\right)_{p,N} \leq 0 \quad \left(\frac{\partial^2 G}{\partial p^2}\right)_{T,N} \leq 0 \quad (1.13)$$

At this point, it is possible to show that the first derivatives of the Euler equation (or of the Gibbs free energy, since among these two there is an equivalence) have a relevant physical significance leading to the definitions of V, M, P and S :

$$V(T, H, p, N, E) = + \left(\frac{\partial G}{\partial p}\right)_{T,H,N,E} \quad (1.14a)$$

$$M(T, H, p, N, E) = - \left(\frac{\partial G}{\partial H}\right)_{T,p,N,E} \quad (1.14b)$$

$$S(T, H, p, N, E) = - \left(\frac{\partial G}{\partial T} \right)_{H,p,N,E} \quad (1.14c)$$

$$\mu(T, H, p, N, E) = + \left(\frac{\partial G}{\partial N} \right)_{T,H,p,E} \quad (1.14d)$$

$$P(T, H, p, N, E) = + \left(\frac{\partial G}{\partial E} \right)_{T,H,p,N} \quad (1.14e)$$

On the other side, the second derivatives of Euler and Gibbs energies are descriptive of material properties (and of physical interest). An example is the second derivative of the Gibbs free energy, corresponding to the specific heat at constant pressure of the material, and computed in Equation 1.15a, while considering Equation 1.15b:

$$c_p(T, H) = T \left(\frac{\partial S}{\partial T} \right)_p = -T \left(\frac{\partial^2 G}{\partial T^2} \right)_p \quad (1.15a)$$

$$S = - \left(\frac{\partial G}{\partial T} \right)_p \quad (1.15b)$$

These results can be justified by introducing the concept of Hessian matrix \mathcal{H} of a real variables function f , defined on a subset Ω of \mathbb{R}^n containing the derivatives till at least the order 2:

$$f : \Omega \subseteq \mathbb{R}^n \rightarrow \mathbb{R}$$

$$\mathcal{H}_f(x) = \begin{pmatrix} \frac{\partial^2 f}{\partial x_1^2} & \frac{\partial^2 f}{\partial x_1 \partial x_2} & \cdots & \frac{\partial^2 f}{\partial x_1 \partial x_n} \\ \frac{\partial^2 f}{\partial x_2 \partial x_1} & \frac{\partial^2 f}{\partial x_2^2} & \cdots & \frac{\partial^2 f}{\partial x_2 \partial x_n} \\ \vdots & \vdots & \ddots & \vdots \\ \frac{\partial^2 f}{\partial x_n \partial x_1} & \frac{\partial^2 f}{\partial x_n \partial x_2} & \cdots & \frac{\partial^2 f}{\partial x_n^2} \end{pmatrix} \quad (1.16)$$

where is assumed that $\forall i, j \in \{1, 2, \dots, n\}$ with $n \in \mathbb{N}$, and $x = (x_1, x_2, \dots, x_n) \in \Omega$. A compact representation is reported just below:

$$\frac{\partial^2 f}{\partial x_i \partial x_j} = \frac{\partial}{\partial x_i} \left[\frac{\partial f}{\partial x_j} \right] \quad (1.17)$$

At this point the Schwarz Theorem, stating that a commutative rule applies, is introduced:

$$\frac{\partial^2 f}{\partial x_i \partial x_j} = \frac{\partial^2 f}{\partial x_j \partial x_i} \quad (1.18)$$

Now, the Hessian matrix of the Gibbs Free Energy $\mathcal{H}(G)$ can be built as follows:

$$\mathcal{H}(G) = \begin{pmatrix} \frac{\partial^2 G}{\partial T^2} & \frac{\partial^2 G}{\partial T \partial p} & \frac{\partial^2 G}{\partial T \partial H} & \frac{\partial^2 G}{\partial T \partial E} & \frac{\partial^2 G}{\partial T \partial N} \\ \frac{\partial^2 G}{\partial p \partial T} & \frac{\partial^2 G}{\partial p^2} & \frac{\partial^2 G}{\partial p \partial H} & \frac{\partial^2 G}{\partial p \partial E} & \frac{\partial^2 G}{\partial p \partial N} \\ \frac{\partial^2 G}{\partial H \partial T} & \frac{\partial^2 G}{\partial H \partial p} & \frac{\partial^2 G}{\partial H^2} & \frac{\partial^2 G}{\partial H \partial E} & \frac{\partial^2 G}{\partial H \partial N} \\ \frac{\partial^2 G}{\partial E \partial T} & \frac{\partial^2 G}{\partial E \partial p} & \frac{\partial^2 G}{\partial E \partial H} & \frac{\partial^2 G}{\partial E^2} & \frac{\partial^2 G}{\partial E \partial N} \\ \frac{\partial^2 G}{\partial N \partial T} & \frac{\partial^2 G}{\partial N \partial p} & \frac{\partial^2 G}{\partial N \partial H} & \frac{\partial^2 G}{\partial N \partial E} & \frac{\partial^2 G}{\partial N^2} \end{pmatrix} \quad (1.19)$$

$$\mathcal{H}(G) = \begin{pmatrix} \frac{\partial^2 G}{\partial T^2} & \frac{\partial V}{\partial T} & -\frac{\partial M}{\partial T} & -\frac{\partial P}{\partial T} & \frac{\partial \mu}{\partial T} \\ \frac{\partial V}{\partial T} & \frac{\partial^2 G}{\partial p^2} & -\frac{\partial M}{\partial p} & -\frac{\partial P}{\partial p} & \frac{\partial \mu}{\partial p} \\ -\frac{\partial M}{\partial T} & -\frac{\partial M}{\partial p} & \frac{\partial^2 G}{\partial H^2} & -\frac{\partial P}{\partial H} & \frac{\partial \mu}{\partial H} \\ -\frac{\partial P}{\partial T} & -\frac{\partial P}{\partial p} & -\frac{\partial P}{\partial H} & \frac{\partial^2 G}{\partial E^2} & \frac{\partial \mu}{\partial E} \\ \frac{\partial \mu}{\partial T} & \frac{\partial \mu}{\partial p} & \frac{\partial \mu}{\partial H} & \frac{\partial \mu}{\partial E} & \frac{\partial^2 G}{\partial N^2} \end{pmatrix} \quad (1.20)$$

where the second matrix is obtained thanks to the Schwarz Theorem (Equation 1.18), leading also to a symmetric matrix. Moreover, some useful thermodynamic relationships have been used, and are reported here [10][11][12]:

$$\left(\frac{\partial V}{\partial T} \right) = - \left(\frac{\partial S}{\partial p} \right) \quad (1.21a)$$

$$\left(\frac{\partial \mu}{\partial T} \right)_p = -\frac{S}{N} \quad \left(\frac{\partial \mu}{\partial p} \right)_T = \frac{V}{N} \quad (1.21b)$$

$$\chi_m = \left(\frac{\partial M}{\partial H} \right)_T \quad (1.21c)$$

$$\chi_e = \left(\frac{\partial P}{\partial E} \right)_T \quad (1.21d)$$

$$\left(\frac{\partial S}{\partial T} \right)_E = \frac{c_E}{T} \quad \left(\frac{\partial S}{\partial T} \right)_H = \frac{c_H}{T} \quad \left(\frac{\partial S}{\partial T} \right)_M = \frac{c_M}{T} \quad \left(\frac{\partial S}{\partial T} \right)_V = \frac{c_V}{T} \quad \left(\frac{\partial S}{\partial T} \right)_p = \frac{c_p}{T} \quad (1.21e)$$

$$\pi_{mp} = \frac{1}{N} \left(\frac{\partial M}{\partial T} \right)_{p,H,N} \quad \pi_{mV} = \frac{1}{N} \left(\frac{\partial M}{\partial T} \right)_{V,H,N} \quad (1.21f)$$

$$\gamma_m = \frac{1}{V} \left(\frac{\partial V}{\partial H} \right)_{T,p,N} \quad \rho_m = \frac{1}{N} \left(\frac{\partial M}{\partial p} \right)_{T,H,N} \quad (1.21g)$$

$$\pi_{ep} = \frac{1}{N} \left(\frac{\partial P}{\partial T} \right)_{p,E,N} \quad \pi_{eV} = \frac{1}{N} \left(\frac{\partial P}{\partial T} \right)_{V,E,N} \quad (1.21h)$$

$$\gamma_e = \frac{1}{V} \left(\frac{\partial V}{\partial E} \right)_{T,p,N} \quad \rho_e = \frac{1}{N} \left(\frac{\partial P}{\partial p} \right)_{T,E,N} \quad (1.21i)$$

$$\frac{\partial}{\partial T} \left(\frac{\partial G}{\partial T} \right) = -\frac{\partial S}{\partial T} \quad \frac{\partial}{\partial p} \left(\frac{\partial G}{\partial p} \right) = \frac{\partial V}{\partial p} \quad (1.21j)$$

$$\frac{\partial}{\partial E} \left(\frac{\partial G}{\partial E} \right) = -\frac{\partial P}{\partial E} \quad \frac{\partial}{\partial H} \left(\frac{\partial G}{\partial H} \right) = -\frac{\partial M}{\partial H} \quad \frac{\partial}{\partial N} \left(\frac{\partial G}{\partial N} \right) = \frac{\partial \mu}{\partial N} \quad (1.21k)$$

In particular, it is possible to see the definition of magnetic and electric susceptibilities (Equations 1.21c-1.21d), the definition of different specific heats with constant electric or magnetic field, magnetization, volume and pressure (Equation 1.21e) where is always present the derivative of entropy with respect to temperature (what is changing is only the parameter remaining constant in the process); in addition, in Equations 1.21f-1.21g show respectively the pyro-magnetic coefficients π_m at constant pressure and volume, the magneto-strictive coefficient γ_m and the piezo-magnetic coefficient ρ_m [13][14]; Equations 1.21h-1.21i define the electrical counterparts of coefficients introduced by magnetic Equations 1.21f-1.21g, so the pyro-electric coefficients π_e at constant pressure and volume, the electro-strictive coefficient γ_e and the piezo-electric coefficient ρ_e [14].

For what concerns the behaviour of the chemical potential μ , it increases with pressure and concentration, reduces with temperature [15][16]; the behaviour with respect to the magnetic field depends on the magnetic property of the material [17].

The final Hessian matrix can be now rewritten considering the coefficients just derived:

$$\mathcal{H}(G) = \begin{pmatrix} \frac{c_x}{T} & \alpha_T V & -\pi_{mx} N & -\pi_{ex} N & -\frac{S}{N} \\ \alpha_T V & \frac{\partial^2 G}{\partial p^2} & -\rho_m N & -\rho_e N & \frac{V}{N} \\ -\pi_{mx} N & -\rho_m N & -\chi_m & -\frac{\partial P}{\partial H} & \frac{\partial \mu}{\partial H} \\ -\pi_{ex} N & -\rho_e N & -\frac{\partial P}{\partial H} & -\chi_e & \frac{\partial \mu}{\partial E} \\ -\frac{S}{N} & \frac{V}{N} & \frac{\partial \mu}{\partial H} & \frac{\partial \mu}{\partial E} & \frac{\partial \mu}{\partial N} \end{pmatrix} \quad (1.22)$$

At this point it could be quite useful to introduce the concept of phase transition, which is central in the condensed-matter physics. Phase transition usually refers to a discontinuous change in the properties of a system, in particular in many cases the systems show a symmetry change: this means that after the transition, the system's properties can show a different behaviour, usually depending on the direction, changing from isotropy to anisotropy (and viceversa). Generally speaking, parameters like pressure, temperature, chemical potential, magnetic and electric fields can drive a phase transition, but in most cases the leading parameter is the temperature: the phase transition occurs at the critical temperature T_c , which differentiates a lower temperature region with high order (and low symmetry) from a higher and disordered temperature zone with high symmetry [18]. Furthermore, an entropy change is always related to a phase transition, and also according to the continuity of the derivatives of G at the phase transition, it is possible to determine the order of the transition (*e.g.* the type of the change):

- **I order transition:** the first derivative is discontinuous at phase transition, so also the volume, the entropy and the magnetization are discontinuous; in this case heat is always released by the system undergoing the transition. Some examples of this phase transition are the solid-liquid-vapour transitions for water and other materials [19] or the nonpyroelectric-pyroelectric transitions at T_c in ferroelectrics [20], or even the solid-solid (martensitic) transitions in crystals [21][22].
- **II order transition:** the first derivative is continuous at phase transition, but the second derivative is discontinuous, so also the volume, the entropy and the magnetization are discontinuous; in this case the specific heat shows a peaked anomaly, while the thermal expansion coefficient has a step at the transition. Examples of this second case are the paramagnetic-ferromagnetic and the conducting-superconducting transitions in metals at low temperatures [20].

Considering the heat capacity C_γ , with γ being the constant parameter (Equation 1.23a), and applying the second law of thermodynamics (Equation 1.23b), the heat capacity is rewritten into Equation 1.23c:

$$C_\gamma = \left(\frac{\delta Q}{dT} \right)_\gamma \quad (1.23a)$$

$$dS = \left(\frac{\delta Q}{T} \right) \quad (1.23b)$$

$$C_\gamma = T \left(\frac{\partial S}{\partial T} \right)_\gamma \quad (1.23c)$$

Knowing that the state variable S is a function of T , H and p , the total differential of S is reported here in Equation 1.24:

$$dS = \left(\frac{\partial S}{\partial T} \right)_{H,p} dT + \left(\frac{\partial S}{\partial H} \right)_{T,p} dH + \left(\frac{\partial S}{\partial p} \right)_{T,H} dp \quad (1.24)$$

For the sake of completeness, here are reported some equations useful to get Equation 1.26, in particular Equations 1.23c-1.25a-1.25e; $\alpha_T(T, H, p)$ represents the bulk thermal expansion coefficient:

$$\left(\frac{\partial S}{\partial H} \right)_{T,p} = \left(\frac{\partial M}{\partial T} \right)_{H,p} \quad (1.25a)$$

$$\left(\frac{\partial S}{\partial p} \right)_{T,H} = - \left(\frac{\partial V}{\partial T} \right)_{H,p} \quad (1.25b)$$

$$\left(\frac{\partial S}{\partial M} \right)_{T,p} = - \left(\frac{\partial H}{\partial T} \right)_{M,p} \quad (1.25c)$$

$$\alpha_T(T, H, p) = - \frac{1}{V} \left(\frac{\partial V}{\partial T} \right)_{H,p} \quad (1.25d)$$

$$\alpha_T(T, H, p) = - \frac{1}{V} \left(\frac{\partial S}{\partial p} \right)_{T,H} \quad (1.25e)$$

If the system undergoes an adiabatic process (in this case $dS = 0$), the Equation 1.24 can be manipulated into Equation 1.26, where $C_{H,p}$ is the heat capacity under constant pressure and

magnetic field:

$$\frac{C_{H,p}}{T}dT + \left(\frac{\partial M}{\partial T}\right)_{H,p} dH - \alpha_T V dp = 0 \quad (1.26)$$

If the the adiabatic process is also isobaric ($dp = 0$), the Equation 1.26 can be rewritten into Equation 1.27a, which shows how the temperature change due to a change of the magnetic field (this is really the magneto-caloric effect). The Equation 1.27b is simply the integral form of Equation 1.27a.

$$dT = -\frac{T}{C_{H,p}} \left(\frac{\partial M}{\partial T}\right)_{H,p} dH \quad (1.27a)$$

$$\Delta T = -\int_{H_0}^{H_1} \frac{T}{C_{H,p}} \left(\frac{\partial M}{\partial T}\right)_{H,p} dH \quad (1.27b)$$

Equations 1.25a-1.25b-1.25c represent the Maxwell Equations. From Equation 1.25a it is possible to compute the magnetic entropy change ΔS_M related to a change ΔH in the magnetic field:

$$\Delta S_M = S_M(H_2, T) - S_M(H_1, T) = \int_{H_1}^{H_2} \frac{\partial M(H, T)}{\partial T} dH \quad (1.28)$$

If the magnetic field change is from $H_1 = 0$ to $H_2 = H$, the Equation 1.29 is obtained:

$$\Delta S_M = S_M(H, T) - S_M(0, T) = S(H, T) - S(0, T) = \Delta S \quad (1.29)$$

The magnetic entropies $S_M(H \neq 0, T)$ and $S_M(H = 0, T)$ are computed from Equation 1.30, where C_M represents the magnetic heat capacity:

$$S_M(H, T) = \int_0^T \frac{C_M(H, T)}{T} dT \quad (1.30)$$

	Temperature	Magnetic field	Specific Heat capacity
LiNi₂P₃O₁₀	7 K	0 kOe to 30 kOe	16 J mol ⁻¹ K ⁻¹
MnCr₂S₄	10 K	100 kOe	5.8 J mol ⁻¹ K ⁻¹
Fe₃Se₄	300 K	Almost independent	31 J mol ⁻¹ K ⁻¹
UAs_{0.8}Se_{0.2}	50 K	0 kOe	4.5 J mol ⁻¹ K ⁻¹
	50 K	90 kOe	3 J mol ⁻¹ K ⁻¹
	125 K	Almost independent	18.8 J mol ⁻¹ K ⁻¹
Fe₃O₄ NP	300 K	...	180 J mol ⁻¹ K ⁻¹
Fe₃O₄ bulk	300 K	...	160 J mol ⁻¹ K ⁻¹
Fe bulk	300 K	...	25.7 J mol ⁻¹ K ⁻¹

TABLE 1.2: Sum-up table of some interesting magnetic heat capacity values from Figures 1.5-1.6 .

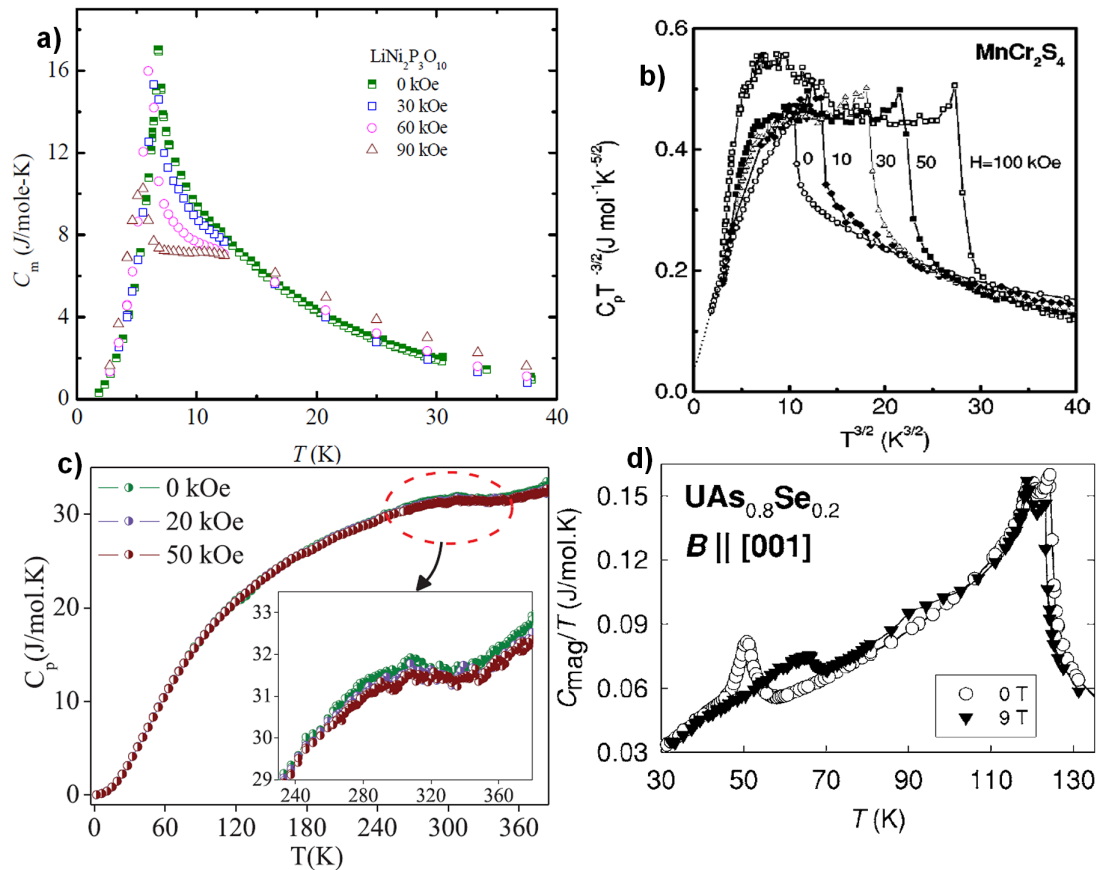


FIGURE 1.5: Magnetic specific heat for different magnetic materials: **a)** $\text{LiNi}_2\text{P}_3\text{O}_{10}$ antiferromagnet for various applied magnetic field [23]. **b)** Ferrimagnetic MnCr_2S_4 single crystals under magnetic fields of different intensity [24]. **c)** Ferrimagnetic Fe_3Se_4 nanorods under magnetic fields of 20 kOe and 50 kOe and no applied field [25]. **d)** Normalized C_M for $\text{UAs}_{0.8}\text{Se}_{0.2}$, where the peaks at $T = 125$ K are insensitive to the magnetic field, while C_M at $T = 50$ K depends on the applied field [26].

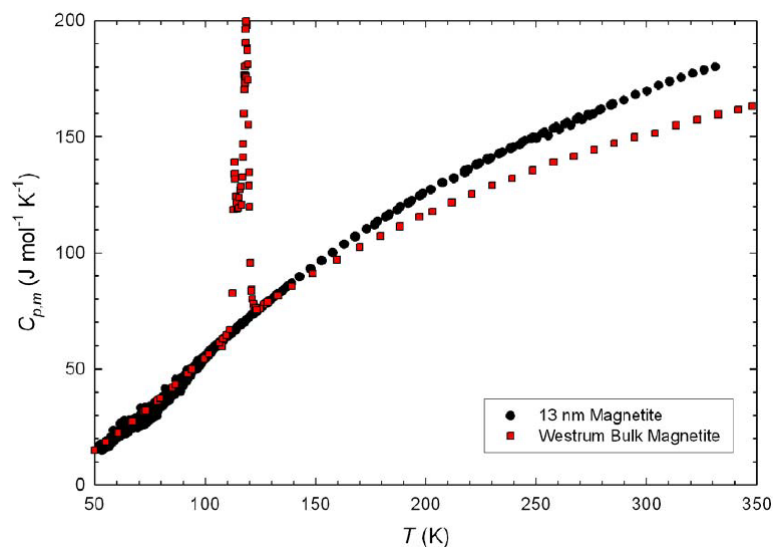


FIGURE 1.6: Magnetic specific heat of nanometric magnetite (black) and bulk magnetite (red) [27] [28]. The nano-magnetite shows no anomaly at Verwey transition, a low temperature (120 K) transition [29].

Possible applications of magnetic NPs are based on the heating of a fluid by efficient magnetic induction, for cancer treatments [30], or for power dissipation inside a FF liquid based on the rotational relaxation of a magnetic domain [31]. In nano-composite magnetic materials, MCE can be improved: considering the works of McMichael et al. (1992) and Shull (1993a, 1993b), a super-paramagnetic system consisting of mono-dispersed and non-interacting magnetic clusters (containing a certain number of magnetic atoms) homogeneously dispersed in a non-magnetic matrix; the mean field approximation (in the classical limit) can be useful for the description of the system.

A classical system has a magnetic entropy change due to the variation of the external magnetic field, which in case of a ferromagnet in proximity of the critical temperature T_c can be computed with the Equation 1.31 (Oesterreicher-Parker equation):

$$\Delta S_M = -1.07R \left(\frac{g_J \mu_B J H}{k_B T_c} \right)^{2/3} \quad (1.31)$$

where g_J is the g-factor (specific for each atom), J the total magnetic moment of the atom, C_J is the Curie constant (Equation 1.32a), μ_B is the Bohr's Magneton and R the gas constant.

$$\Delta C_J = -\frac{N\mu^2}{3k_B} \quad (1.32a)$$

$$\mu_B = \frac{e\hbar}{2m_e} = 9.274\,009\,49 \times 10^{-24} \text{ J/T} \quad (1.32b)$$

Here N represents the number of magnetic moments inside the system, while μ is the magnetic moment. If μ becomes larger, and at the same time N decreases, so that the saturation magnetic moment $M_0 = N\mu$ stays constant, ΔS_M enlarges together with MCE. This can be explained with the fact that ΔS_M has a squared dependence on μ and only a linear dependence on N . The MCE shows a maximum for:

$$x_{max} = \frac{\mu_c H}{k_B T} \simeq 3.5 \quad (1.33)$$

to which correspond an optimal cluster size for given T and H , but also a certain ΔS_M , given by:

$$\Delta S_M = -0.272 \cdot \frac{M_0 H}{T} \simeq 3.5 \quad (1.34)$$

A sum rule can be obtained by integrating from zero to H and temperature T in range 0 to ∞ :

$$\int_0^\infty \Delta S_M dT = -M_0 H \quad (1.35)$$

Thank to Equation 1.35, it is possible to determine the behaviour of $\Delta S_M(T)$, from which can be derived that for materials with the same saturation magnetic moment M_0 , the ones with the higher ΔS_M at a specific temperature will have a smaller variation in the magnetic entropy in the remaining temperature range.

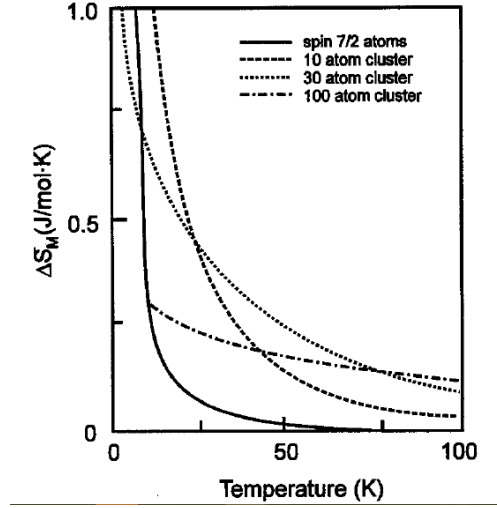


FIGURE 1.7: Theoretical magnetic entropy variation due to the removal of a magnetic field of 10 kOe for systems with different arrangements of 7/2 spin atoms [32].

In Figure 1.7 are reported the results for single atoms and clusters with different sizes; it is possible to see that the behaviour of the clustered atoms is in accordance with the experimental one measured for the single atom [33]. Moreover the δS_M is clearly enhanced at high temperatures and in clustered systems, as predicted by Equation 1.35.

A step further can be done if considering that cluster magnetic moments are dependent on the temperature; so, Equation 1.31 (where μ was supposed independent on T) will be transformed into Equation 1.36:

$$\Delta S_M = -\frac{n\mu_c^2 H^2}{6k_B T^2} \cdot \left(1 - \frac{T}{\mu^2} \frac{\partial \mu_c}{\partial T}\right) \quad (1.36)$$

Important to notice that the second term in the parentheses of the latter equation is quite relevant in proximity of the Curie point of a magnetic cluster, which gives an additional contribution to ΔS_M in this region.

When the particles size reduces up to the nanometric range, the Curie temperature is substituted by a blocking temperature T_B , the magnetite NPs (diameter size ≈ 5 nm) show a superparamagnetic behaviour also at room temperature [34]. Superparamagnetism occurs in NPs when the Néel-Brown relaxation time (time comprised between two magnetization thermal fluctuations, Equation 1.37a) is much shorter than the time needed to measure the magnetization of the particles themselves: so, the net magnetization of the NPs result to be zero in average.

$$f = f_0 \exp\left(-\frac{E_a}{k_B T}\right) \quad (1.37a)$$

$$E_a = K_{eff} \cdot V \quad (1.37b)$$

where E_a is the energy barrier separating the switching of the particle from the two possible magnetizations, $K_{eff} = 356 \text{ kJ/m}^3$ is the effective magnetic anisotropy constant (proportional to the NP volume V , and much larger than the corresponding bulk one, $K_{bulk} = 13.5 \text{ kJ/m}^3$) [34]. Moreover superparamagnetism can be easily distinguished from ferromagnetism and paramagnetism (Figure 1.8).



FIGURE 1.8: **a)** Behaviours of ferromagnetism (blue), paramagnetism (green) and superparamagnetism (red). The latter shows the absence of both coercive and residual magnetic fields, contrary to what happens in the ferromagnetic behaviour. **b)** Behaviour of the coercive field H_c against the particle size [35].

If T is lowered below T_B under an applied H field, the NPs become blocked in a specific state. In particular, in zero-field-cooling (ZFC), the magnetic moment increases while temperature is reduced, but when a certain T_B is achieved, the magnetization starts decreasing; in field-cooling (FC) the magnetic moment decreases when reducing T (Figure 1.9).

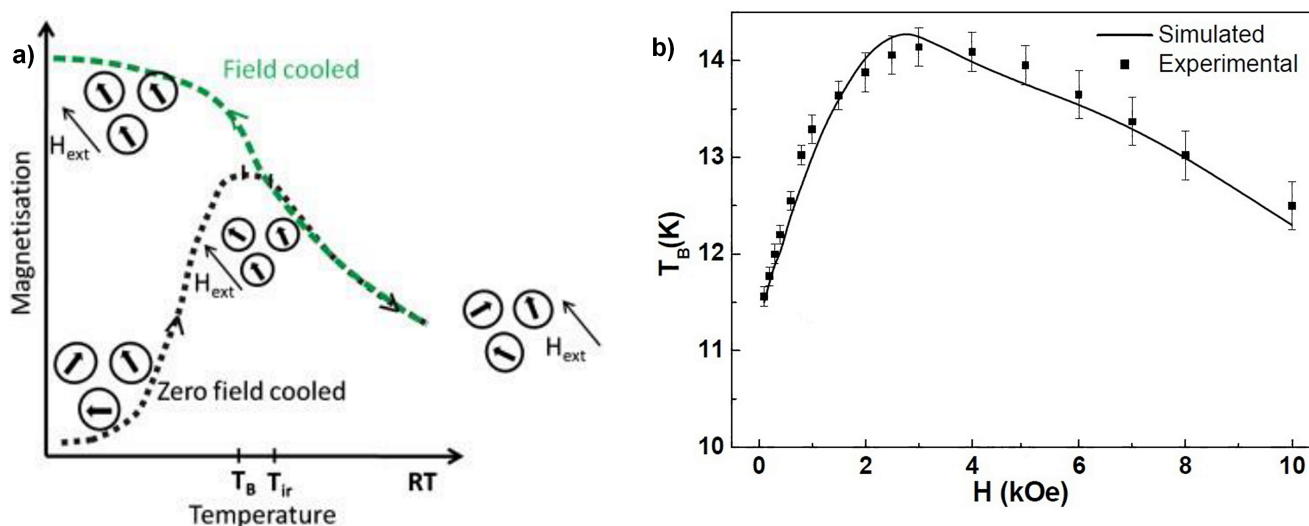


FIGURE 1.9: **a)** Behaviour of the ZFC and FC curves. **b)** Behaviour of the blocking temperature plotted against the applied magnetic field [36].

When the temperature is decreased, the energy barrier E_a reduces, as well the thermal fluctuations of the magnetization, until below T_B the particle becomes blocked. In addition, an increasing magnetic field is theoretically able to reduce the blocking temperature, because it provides the energy required for the flipping of the magnetization. In the first left-side, the literature shows that T_B increases with the applied field, since the Zeeman energy is much smaller than the thermal energy [36]. Instead at higher magnetic field, the magnetization decreases much slower than thermal dependence and the theoretical behaviour is recovered. Furthermore, since the volume is larger in large NPs, the blocking temperature T_B is greater in large particles.

Recalling Equation 1.33, the optimal size of a magnetic cluster is in the nanometric range, given $T=300$ K and $H=10 \div 50$ kOe. A possible drawback is the formation of chains, which increases the sizes of the magnetic clusters and leading to a reduction of the magnetic entropy

variation (Figure 1.10). This reduction depends on the dilution level of the magnetic clusters inside the non-magnetic particles, that is to say that dilution value corresponds to the ration between the non-magnetic particles and the magnetic ones. As a consequence, for large clusters ΔS_M enlarges when the dilution increases, while for small clusters ΔS_M decreases with increasing dilution.

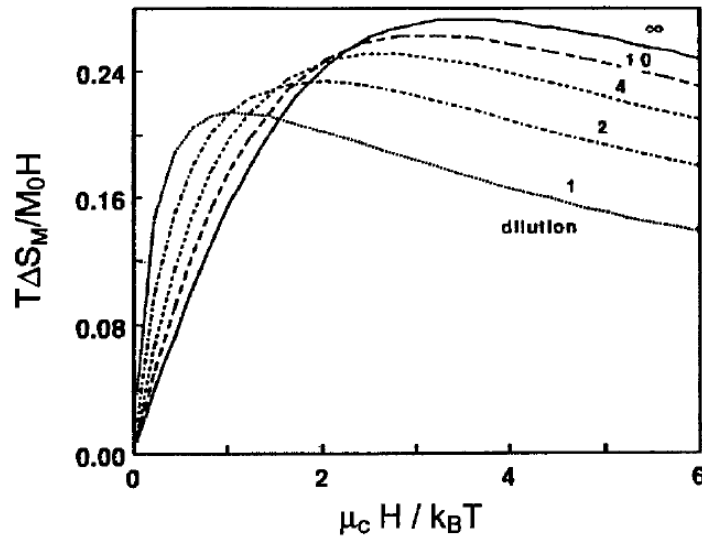


FIGURE 1.10: Computed reduced ΔS_M as a function of $x = \mu_c H / (k_B T)$ with different dilution levels (numbers near the curves) of the magnetic clusters by the non-magnetic particles [37].

There are several methods and techniques to measure the MCE; in particular they are:

- **Pulse techniques:** this method directly measures (with thermocouples) the change in the temperature of the material when a magnetic field generated by an electromagnet is applied or removed; this method was proposed by Weiss and Forer in 1926.
- **Magnetization measurements:** variations on the dependence of the magnetic field on the magnetization permit to measure ΔS_M with Equations 1.28-1.29 and MCE with Equation 1.38.

$$\Delta T = -\frac{T \cdot \Delta S_M}{C_{p,H}} \quad (1.38)$$

- **Heat capacity measurements:** it was used for the first time by Brown and Gschneider to measure MCE and ΔS_M , but to determine heat capacity and $S(T, H)$ dependences too [38].

1.3.3 Ferrofluids

FFs, developed for the first time in 1960's for space applications [39], can be used to harvest energy, giving the possibility to implement a low-power consumption micro-generator, especially for electronics where battery replacement has high costs and is quite difficult.

In literature it is possible to find several methods to harvest energy from a FF, so some of them are reported in the list below, and one FF generator will be described in details:

- **Peristaltic pumping:** Monroe et al. [40] developed a micro-generator based on a peristaltic pulse of an aqueous FF (dispersed magnetite NPs around 7 nm ÷ 10 nm) at low frequencies (< 10 Hz); the liquid is coupled with copper-wire solenoid placed at a distance of 45 cm away from the pump: the open circuit voltage induced at the output was measured to be $\pm 20 \mu\text{V}$.
- **Springless proof mass:** in this article [41] a springless proof mass (simply an array of rectangular permanent magnets) is used together a FF, acting as a lubricant, both contained inside an Aluminum channel; when the magnets move laterally, due to low frequency external vibrations, an electromotive force is induced in the copper windings placed under the channel itself: the measured output voltage can reach 470 mV at 3g acceleration at 12 Hz. Moreover, the maximum power at the output is 71.26 μW with a resistive load of 40.8 Ω .
- **FF vaporization:** the idea of [42] was to develop FF power generator recycling the waste heat coming from electronic devices, in order to vaporize aqueous FF, creating a pumping mechanism with the generated bubbles; the bubbles create a varying magnetic flux, flowing across a coil, and producing an induced current.
- **Thermal gradient:** a second idea introduced in [42], regards a way to produce electrical power thanks to the FF motion activated by convection currents generated by a thermal gradient; the conduit has a particular shape and is coiled around a cone-shaped magnet. In this way, when heated up, the FF moves producing an output current, and then FF is cooled down with an opportune heat sink (can be ice, water...).
- **Mechanical excitation:** in this last case, a FF is mechanically excited in order to produce surface and rotational waves with large amplitudes, so a varying magnetic flux is produced and an output electromotive force (e.g. a voltage) is obtained [43].

The latter will be now analysed in details: this type of generator is based on the sloshing of a FF column contained inside a seismically excited tank to transform the mechanical motions into electricity. One of the advantage over the traditional electromagnetic generators (based on solid magnets), is the ability of FF to easily adapt to different shapes and injected into hard-to-access locations, together with the scalability.

FF are active materials, or better, they are colloidal liquids composed of nanometric particles which behave as permanent magnetic dipoles, able to show electromechanical coupling mechanisms used to generate an electrical potential as a result of a mechanical stimulus.

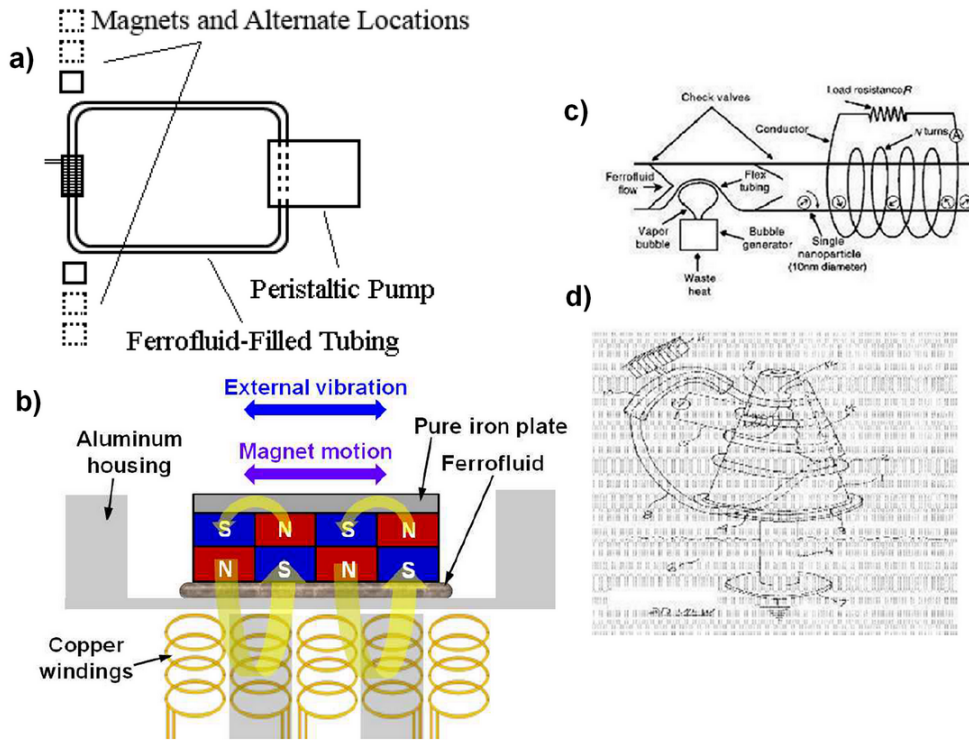


FIGURE 1.11: Basic schematics of different FF energy harvesters: **a)** Peristaltic energy harvester [40]. **b)** FF harvester based on a springless proof mass and FF used as lubricant [41]. **c)** FF harvester based on the vaporization of the FF fluid to get the varying magnetic field [42]. **d)** FF harvester based on shaped magnetic cone with a conduit containing the FF coiled around it [42].

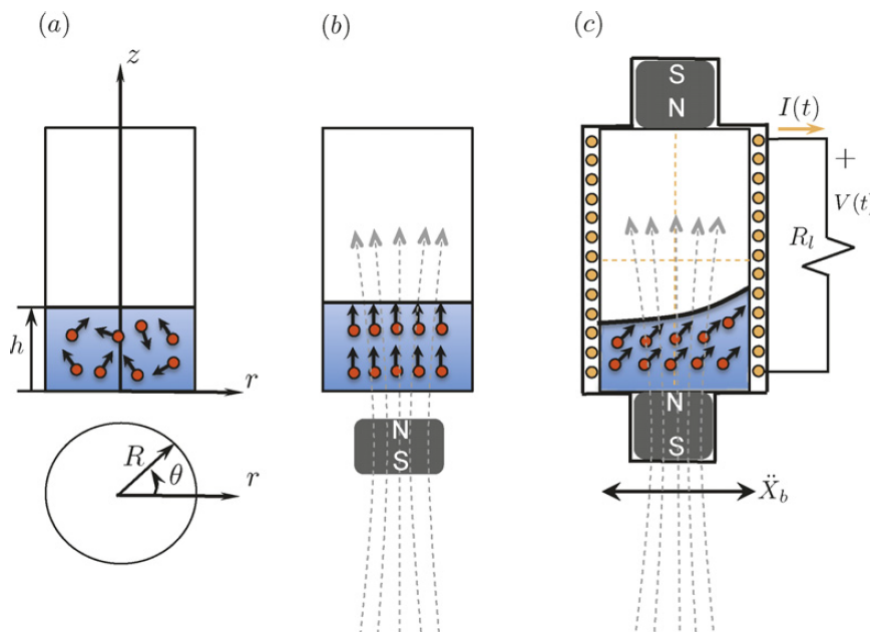


FIGURE 1.12: Basic schematic of the FF based energy harvester [43]: **a)** FF in absence of a magnetic field (dipoles are randomly oriented). **b)** FF in presence of a magnetic field (dipoles are aligned with the magnetic field). **c)** FF in presence of two permanent magnets (upper and lower), generating a magnetic flux across the wounded coil and an induced electric current transformed into an electric voltage drop by means of the load resistance.

When the external magnetic field is absent, the dipoles are randomly oriented inside the carrier fluid, and the resulting net magnetization is equal to zero. Otherwise when the external magnetic field is switched on, the dipoles become parallelly aligned in the direction of the field, and a non-zero net magnetization appears. At this point, the carrier fluid is subjected to mechanical excitations with a frequency that should match one of the modal frequencies of the fluid itself (notice that the number of modal frequencies is practically infinite): at resonance surface waves with large amplitude (either horizontal and rotational) are excited. It is exactly the sloshing of the FF liquid that produces a variation in the orientation of the magnetic dipoles, leading to the creation of a time-varying magnetic flux. The latter is the responsible of the induces electromotive force in the coil wound around the tank, generating an electric current described by the Faraday's Law.

The mechanic excitations with different intensities and frequencies are produced by means of an electrodynamic shaker, while two permanent magnets placed at bottom and top sides of the tank generate the magnetic field; for the FF, magnetite NPs (Fe_3O_4) are very commonly used diluted in an aqueous (or organo-metallic) solvent, and surfactants are added to the colloid to improve its stability, avoiding the unwanted agglomeration of the ferrous nanoparticles (≈ 10 nm) [44].

Resonant motions are necessary to create large amplitudes of the surface waves, which are needed to obtain a relevant variation in the magnetic flux through the coil; assuming small surfaces waves and neglecting the effects of the surface tension, the resonances occur in proximity of the undumped modal frequencies of fluid (Equation 1.39):

$$f_{mn} = \frac{1}{2\pi} \sqrt{\frac{g^* k_{mn}}{R} \cdot \tanh\left(\frac{k_{mn} h}{R}\right)} \quad (1.39)$$

where h is the liquid height, R is the radius of the tank, m and n denotes the different oscillation modes, k_{mn} represents the roots of $J_m(k_{mn} r/R) dr|_{r=R} = 0$ (Bessel functions of first type and order m), and g^* denotes the effective acceleration due to magnetic and gravitational fields (Equation 1.40). If m is even, the waves are symmetrical (rotational) about the origin, so the resulting net magnetic flux is quite small, on the contrary, when m is odd, the produced waves are **asymmetrical** (horizontal) with a nodal diameter through the origin orthogonal to the excitation direction.

$$g^* = g - \frac{\chi}{\rho\mu_0} \frac{dB(z)}{dz} dB|_{z=h} \quad (1.40)$$

Here g denotes the gravitational acceleration, μ_0 is the vacuum magnetic permeability and $B(z)$ is instead the magnetic induction along the normal line linking the upper and lower permanent magnets. It is quite remarkable the fact that over a given height h , the modal frequencies can be decreased if the radius of the container is enlarged (and viceversa): this possibility of tuning the modal frequency of the harvester towards low-frequency excitations, which are very common in nature. Moreover, the frequencies decrease when increasing the height of the liquid, since the gravitational effective field g^* reduces due to higher values of h for a given magnetic field. It is remarkable the fact that the experimental values are just slightly underestimated because the viscous damping effects were neglected in the theoretical description (Figure 1.13).

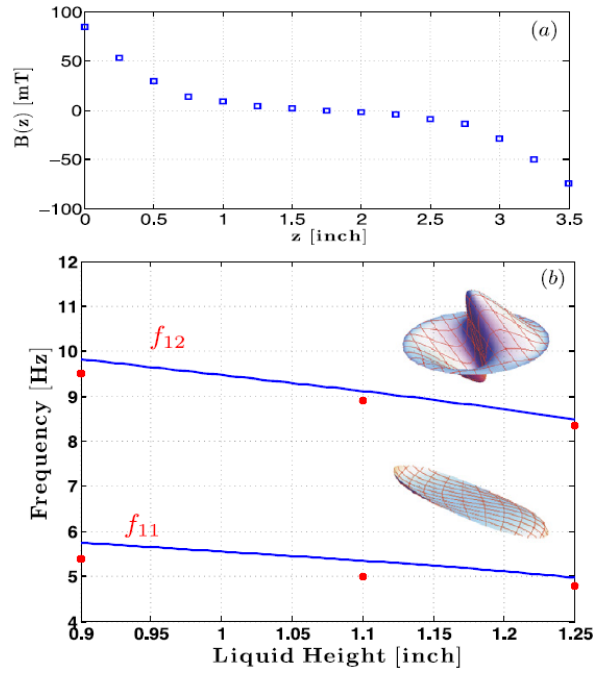


FIGURE 1.13: Different responses (magnetic induction and frequency) according to varying height of the liquid [43]: **a)** Behaviour of the magnetic induction distribution inside the FF liquid. **b)** Behaviour of the modal frequencies f_{11} and f_{12} plotted against the liquid height (it is possible to notice how the frequency decreases with h).

Once the spectrum range within which the two modal frequencies are contained, the tank can be shaken with harmonic mechanical excitations with low-frequencies varying in that specific range. So a steady-state output voltage of the harvester can be measured with an open-circuit configuration.

Figure A.1a shows that the height has practically zero influence on V_{out} for given magnetic field and input acceleration. The reason of this behaviour lays in the fact that the largest waves (and deformations) occur at the surface, so the dipoles close to liquid surface are the most critical ones for the harvesting process; in particular the number of magnetic dipoles is mainly defined by the cross-section of the tank and by the percentage of dipoles per unit volume of the fluid. It is important to notice that peaks on the left side of Figure A.1a are related to f_{11} (symmetric mode), and the two other small peaks on the right are the ones of f_{12} (asymmetric mode).

The dependence of the output voltage on other parameters, like the height of FF or the distance of the magnets from the tank, is shown in Section A.1.

However, even if FF based harvesters are feasible, up to now their power levels (≈ 20 mV \div 30 mV) are still small compared to the traditional electromagnetic energy harvesters.

1.3.4 Gravitational Effects on Ferrofluids

Magnetic colloids, such as FFs, are nano-materials that present a large magnetic susceptibility, higher of some orders of magnitude than natural substances [44]. These nano-materials show stronger/lower thermal convection due to a competition among the magnetic field and the gravitational one, in particular resulting in gravitational sedimentation of the colloidal magnetic particles by the effect of the fluid density stratification. In this way, if the gravitational effect (*i.e.* the sedimentation) should be limited (or ideally removed), more accurate

experiments must be performed in microgravity conditions in order to determine the transport coefficients of the fluid [44].

The magnetic flow can be destabilized by the presence of a buoyancy force, generating the so-called gravitational convection (a type of natural convection). The natural convection is due to thermal gradients affecting the density and the relative buoyancy of the fluid: denser (and heavier) parts will fall, while less dense (and lighter) parts will rise, provoking fluid movements [45]. In the case of a FF and of an external magnetic field, a thermo-magnetic convection can happen in presence of a temperature difference which induces different magnetic body forces (the cooler part will have an higher magnetization than the warmer part). In order to better describe the problem, the Grashof numbers (dimensionless parameters, Equations 1.41a-1.41b) for the gravitational (Gr) and the magnetic (Gr_m) fields, are introduced. When the ratio Gr_m/Gr is small (small values of Gr_m and high values of Gr), the dominating mechanism is the thermo-gravitational one; but if Gr_m/Gr increases, the thermo-magnetic convection arises and can also become dominant [46].

$$Gr = \frac{\rho^2 \beta \theta g d^3}{\eta^2} \quad (1.41a)$$

$$Gr_m = \frac{\rho \mu_0 K^2 \theta^2 d^2}{\eta(1 + \chi)} \quad (1.41b)$$

where β is the thermal expansion coefficient, K the pyromagnetic coefficient, χ the differential magnetic susceptibility, $2d$ the thickness of a fluid layer, and 2θ the temperature difference between the hot and cool walls.

The time (diffusion time [44]) needed by the gravity to create sedimentation layers is described by Equation 1.42 (h is the height of an enclosure, while D is the diffusion coefficient):

$$t_D = \frac{h^2}{D} \quad (1.42)$$

the magnetic phase gradients due to the sedimentation originate convective motions in colloids, which occur with a faster t_D (smaller than three orders of magnitude) when subjected to normal gravity. If the magnetic particles aggregate, the diffusion time will become even shorter.

The advantage of the thermo-magnetic convection is the ability to provide a way for the heat transfer in all cases where it is difficult, like miniaturized devices and micro-gravity conditions.

When the gravitation effect dominates (top-left side of Figure 1.14), the thermal map of the fluid is reported in Figure 1.15.

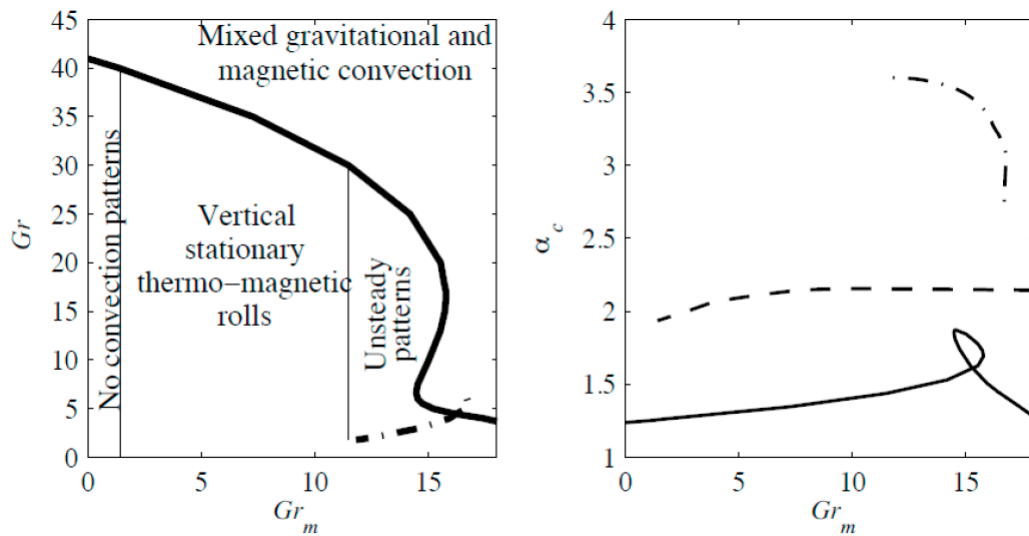


FIGURE 1.14: Parametric map (left-side) and wavenumbers (right-side) relative to an infinite vertical layer of FF; the mixed gravitational and magnetic convection, vertical magneto-convection and thermo-magnetic convection are represented with a solid, dashed and dotted-dashed lines, respectively [46].

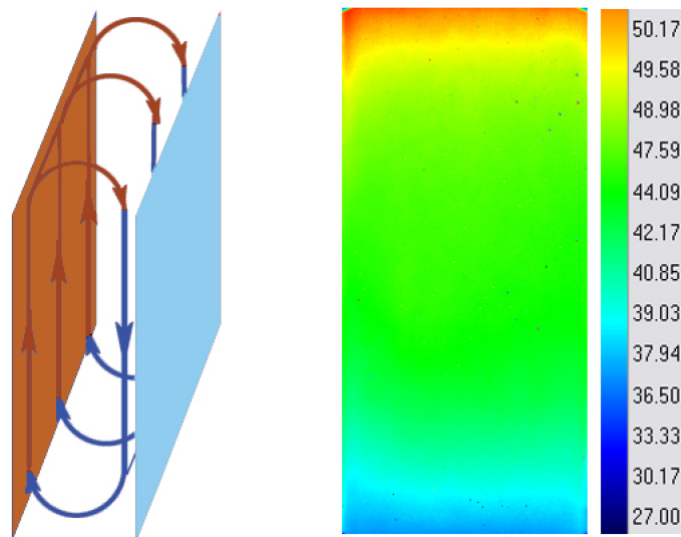


FIGURE 1.15: Thermo-gravitational flow when the magnetic field is zero [47]: on the left, a simple schematic view, while on the right the infrared image of a textolit wall; the temperature gradient between the textolit and aluminium walls is 40°C .

On the other side, when the gravitational effects are negligible and/or the magnetic effects are large (Gr_m is dominant), magnetic rolls appear in the thermal map, showing the direction of the heat transfer (Figure 1.16).

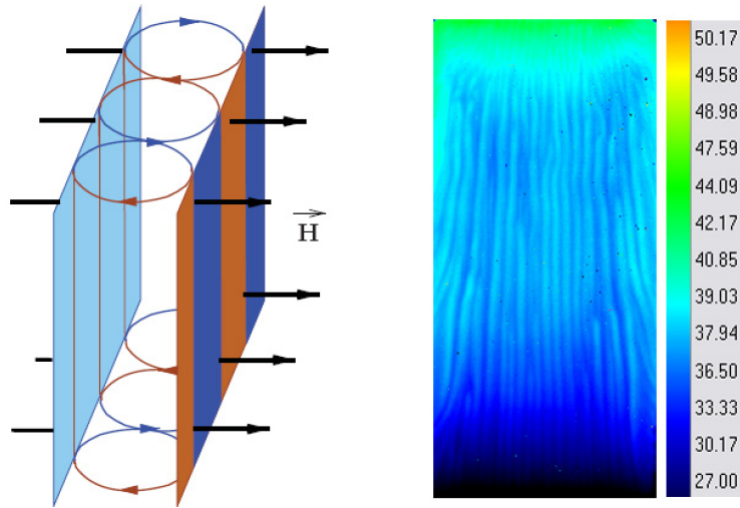


FIGURE 1.16: Thermo-magnetic flow appearing inside a homogeneous magnetic fluid in presence of a magnetic field $H = 35 \text{ kA/m}$ is applied orthogonally to the image plane [47]: a schematic view (left) and the relative infrared image of the textolit wall (right). The thermal gradient between the textolit and aluminium walls is 40°C .

1.4 Fluctuation Theorem

Since the time of Boltzmann, the reason why reversible microscopic motion equations were able to lead to an irreversible macroscopic behaviour was a paradox for the mechanical statistics along the whole XIX century. For Boltzmann himself, the solution of the paradox was simply: *“as soon as one looks at bodies of such small dimension that they contain only very few molecules, the validity of this theorem [the second law of thermodynamics and its description of irreversibility] must cease”*. [48]

But in the 1990's, Evans and Searles presented their FT (Fluctuation Theorem) [49], giving a formulation for the probability of observing violations (*i.g.* fluctuations) of the Second Thermodynamic Law in thermostated dissipative non-equilibrium systems, which must be small in size and observed for very short period.

If a time reversible thermostated system is considered, then the following Equation 1.43 appears:

$$\Sigma(t) = -\beta J(t) F_e V = \int_V \frac{\sigma(\vec{r}, t)}{k_B} dV \quad (1.43)$$

where V is the system volume, F_e is the external dissipative field (*e.g.* the optical force of Equation 1.53 [50]), J is the dissipative flux and $\beta = 1/(k_B T)$; then, after the non-equilibrium steady state has been reached, the fluctuations of the averaged irreversible entropy production over time (Equation 1.44) will satisfy Equation 1.45:

$$\bar{\Sigma}_t \equiv \frac{1}{t} \int_0^t \Sigma(s) ds \quad (1.44)$$

$$\lim_{t \rightarrow \infty} \frac{1}{t} \ln \left(\frac{p(\bar{\Sigma}_t = A)}{p(\bar{\Sigma}_t = -A)} \right) = A \quad (1.45)$$

The numerator in the latter equation indicates a probability $\bar{\Sigma}_t$ inside the range A and $A+dA$, while the denominator indicates a probability $\bar{\Sigma}_t$ comprised among $-A$ and $-A-dA$; important to notice that Equation 1.45 is valid for F_e of arbitrary magnitude.

1.4.1 The Phase Space

When considering the trajectories $\Gamma(t)$ of a system, a useful representation can be done in terms of coordinates \vec{q} and momenta \vec{p} , taking into account all the particles forming the system (solvent+solute) together with the thermal bath; the resulting graph is called (\vec{q}, \vec{p}) space.

The initial state (\vec{q}_0, \vec{p}_0) at $t = 0$ moves towards a final state (\vec{q}_t, \vec{p}_t) after a time t , and this represent a trajectory $\Gamma(t)$, which is solution of the Newton's motion equations. As Loschmidt stated [51], these equations can be reversed in time, for each trajectory (solution of motion equations) there exists an antitrajectory $\Gamma^*(t)$ (it is simply a time-reversed trajectory) which is itself solution of those equations. The time evolution of $\Gamma^*(t)$ is from the initial state $(\vec{q}_t, -\vec{p}_t)$ to a final state $(\vec{q}_0, -\vec{p}_0)$: as a consequence, $\Gamma(t)$ and $\Gamma^*(t)$ are a couple of conjugate trajectories linked together by time reversal.

Now, a set of trajectories starting from an infinitesimal volume $\delta V \equiv \delta\vec{q}_0\delta\vec{p}_0$ around the initial state (\vec{q}_0, \vec{p}_0) , and another set of antitrajectories starting inside an infinitesimal volume $\delta V^* \equiv \delta\vec{q}_t\delta\vec{p}_t$ around the initial state $(\vec{q}_t, -\vec{p}_t)$. So, the probability $P(\delta V)$ of observing trajectories started at δV with respect to the probability $P(\delta V^*)$ of observing antitrajectories started at δV^* can be expressed by the following ratio:

$$\Omega_t(\vec{q}_t, \vec{p}_0) \equiv \ln \left[\frac{P(\delta V)}{P(\delta V^*)} \right] \quad (1.46)$$

The system is obviously thermodynamically reversible if the probabilities $P(\delta V) \equiv P(\delta V^*)$, resulting in $\Omega_t = 0$.

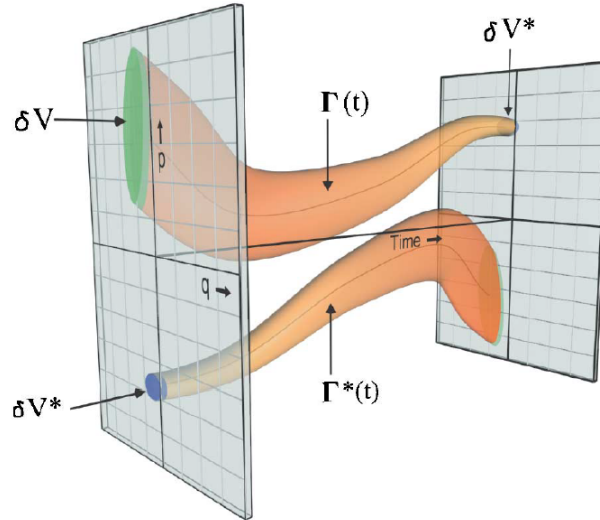


FIGURE 1.17: Illustration of the phase space [52], showing the trajectories $\Gamma(t)$ starting at volume δV , and the corresponding antitrajectories $\Gamma^*(t)$ starting at δV^* ; the coordinates (\vec{q}, \vec{p}) are represented together with time t .

1.4.2 Liouville Derivation of FT: the Transient Fluctuation Theorem

It is possible to derive a more useful expression of the FT, called TFT, or Transient Fluctuation Theorem; the presented approach is the one followed by Liouville [49], which derived the relationship of Equation 1.47:

$$\frac{p(\bar{\Omega}_t = A)}{p(\bar{\Omega}_t = -A)} = \exp(At) \quad (1.47)$$

The latter can be applied to any valid ensemble or dynamic combination.

1.4.3 FT experimental demonstration

The well-known Second Law of Thermodynamics states that the produced entropy must be larger or equal to zero, and applies to systems infinite in size and for large observation periods. In this latter case, the entropy production is irreversible even if the microscopic motion equations are fully time reversible. Moreover entropy is an extensive property, and as a consequence it increases with observation time and system size, and Equation 1.47 degenerates into the thermodynamic limit.

Otherwise, if the system size are scaled down to nanometric size (comparable with the physical dimensions of atoms), classical thermodynamics cannot more applied. In this case, the experiment made by Carberry et al. [52], where a colloidal particle is held inside an optical trap.

The particle of a transparent sphere of micro-meter dimensions, whose refractive index should be larger than the one of the surrounding environment, and placed within a laser beam spot. When the rays are refracted, they show different intensities in the sphere volume, producing a force ($\approx 10 \times 10^{-12}$ N) on the particle, and pushing the particle towards the region of higher light intensity. The potential energy of the system is:

$$\frac{1}{2}k(\vec{r} \cdot \vec{r}) \quad (1.48)$$

which shows that the optical trap is harmonic near the focal point; \vec{r} represents the vector position of the particle with respect to the origin, while k indicates the trapping constant (can be adjusted varying the optical power). At this point, all the trajectories of the particle are recorded, and for each trajectory the entropy production is analysed. For this analysis, the TFT (Equation 1.47) can be more advantageous than simple FT, since here transient responses of a system are recorded; in fact, the FT represents how happens the transition from the time-reversible microscopic equations of motion to the macroscopic ones. Furthermore, an integrated form of FT, IFT or Integrated Fluctuation Theorem, reported in Equation 1.49, is even more useful to estimate quantitatively the results, in particular the ratio of the frequency of consuming entropy trajectories over the producing entropy trajectories.

$$\frac{p(\bar{\Omega}_t < 0)}{p(\bar{\Omega}_t > 0)} = \langle \exp(-\bar{\Omega}_t) \rangle_{\Omega_t > 0} \quad (1.49)$$

The experiment is based on the activity of Wang et al. [50]: they considered a particle held in a stationary optical trap with strength constant k_0 for a time long enough to be sure that its position can reach an equilibrium distribution. Then, at $t=0$, the strength constant is immediately increased up to k_1 , resulting in a more confined particle; the particle's position is again traced while relaxing into its new equilibrium distribution. In this way, the function Ω_t is estimated, since it changes with t according to both TF and IFT. Ω_t represents, in the

more general case, the dissipation function, and in this case it denotes the entropy production, while its average value $\langle \Omega_t \rangle$ corresponds to the irreversible produced entropy (always a positive quantity). Moreover, it possible to enlighten the fact that, if a system is in motion, accordingly with the second law of thermodynamics, the dissipation function is positive and leads to a production of entropy. On the contrary, a motion opposite to the second law of thermodynamics, is related to a negative dissipation function corresponding to an entropy consumption.

In colloidal systems, the inequality in the time scales of motion between colloids and solvent particles can lead to some bad simulations; an idea is to consider that the colloidal particle can be approximated during its motion by the inertialess Langevin equation, a first order stochastic differential equation. The large number of freedom degrees related to solvent particles can be rewritten into viscosity and temperature (macroscopic material properties), while the striking effect of solvent molecules on colloidal particles is described by a fluctuating random force. The resulting coordinates used to define the system are only the vector positions of the colloidal molecules, since the (\vec{q}, \vec{p}) are recasted into \vec{r} . Also in this case the trajectories start from \vec{r}_0 moving towards \vec{r}_t during time interval t , and the corresponding antitrajectories follow the opposite path from \vec{r}_t to \vec{r}_0 . As done before, the probabilities are $P(\vec{r}_0, \vec{r}_t)$ (for the trajectories), and $P(\vec{r}_t, \vec{r}_0)$ (for the antitrajectories); the corresponding ratio is derived in Equation 1.50:

$$\Omega_t(\vec{r}_0, \vec{r}_t) = \ln \left[\frac{P(\vec{r}_0, \vec{r}_t)}{P(\vec{r}_t, \vec{r}_0)} \right] \quad (1.50)$$

Another possibility is to use the Green's function to obtain the probability of observing a particle at position \vec{r}' inside a trap with strength k , known its earlier position \vec{r} at time t ; the corresponding Green's function becomes $G(\vec{r}', k; \vec{r}_0, t)$. If the observation time drastically increases, the probability function degenerates into the Boltzmann's equilibrium distribution $P_B(\vec{r}', k)$; for the forward and backward propagating trajectories, Equations 1.51a and 1.51b are respectively obtained:

$$P_B(\vec{r}_0, \vec{r}_t) = P_B(\vec{r}_0, k_0) \cdot (\vec{r}_t, k_1; \vec{r}_0, t) \quad (1.51a)$$

$$P_B(\vec{r}_t, \vec{r}_0) = P_B(\vec{r}_t, k_0) \cdot (\vec{r}_t, k_1; \vec{r}_0, t) \quad (1.51b)$$

The dissipation function of Equation 1.50 can now be expressed by the simplified Equation 1.52:

$$\Omega_t = \frac{1}{2k_B T} (k_0 - k_1) (\vec{r}_t^2 - \vec{r}_0^2) \quad (1.52)$$

The entropy production of a particle while moving for time t along a trajectory is computed as in Equation 1.53:

$$\Omega_t = \frac{1}{k_B T} \int_0^t \vec{v}_{opt} \cdot \vec{F}_{opt} ds \quad (1.53)$$

According to [50], the particle position is firstly recorded for 2 s in absence of any stage translation in order to get its average values of \vec{r}_t , then at $t = 0$ the stage translations are started ($-v_{opt} = 1.25 \mu\text{m/s}$) keeping the sampling rate fixed at 1 kHz; particles are recorded for $t = 10$ s, so their steady-state velocity is reached. Figure 1.18 shows more than 500 transient trajectories automatically got with this method: looking at the left side of the graph (i.g. for small $\approx 10 \times 10^{-2}$ s), the curve is nearly symmetric and centred around $\Omega_t = 0$; when time becomes longer than few seconds, the curve becomes less symmetric while moving towards positive values of Ω_t . The latter means that the probability of observing consuming entropy events

decreases with increasing observation time, and classical thermodynamic behaviour is completely recovered.

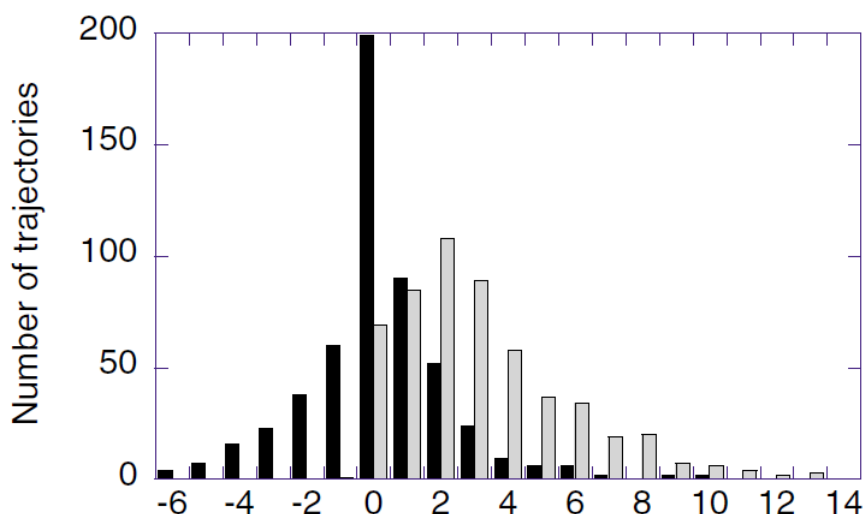


FIGURE 1.18: Histogram representing the number of trajectories versus the dimensionless mean entropy production Ω_t/t . The experimental set consists of 540 trajectories of colloidal particles held in the optical trap at times $t = 10 \times 10^{-2}$ s (black bars) and $t = 2.0$ s (grey bars) after the initiation of the translation stage. Bin size is unitary: $\Omega_t/t = 1.0$ [50].

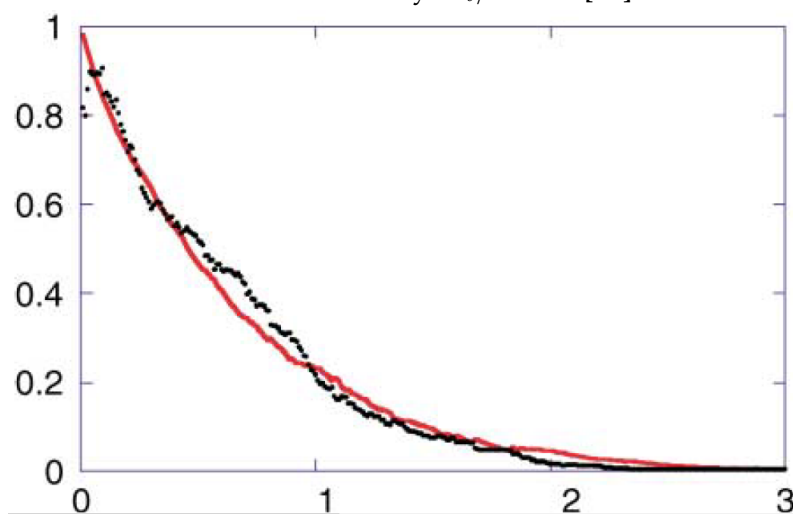


FIGURE 1.19: Exponential decreasing curve representing the number the ratio of produced entropy over the consumed entropy (left-hand of Equation 1.49) and the average entropy production (right-hand of Equation 1.49), both plotted against the time t . The results agree with the IFT [50].

The IFT of Equation 1.49 can be plotted for this experiment in Figure 1.19, where the black line represents the left-side of the equation, while the red one is related to the right-side of the equation. The behaviour is clearly a decreasing exponential when time increases, and the two lines show a good approximation, even if an unpredicted error occurs for very small values of t , maybe due to limits of the detector to discriminate between small positive and small negative values of Ω_t ($|\Omega_t| < 10 \times 10^{-4}$). The results of Figure 1.19 can be derived by means of MD (Molecular Dynamics) simulations, better explained in Section A.2. However, considering again a CERES system, the FT theorem is quite useful to describe the concept of negative entropy change, related to microscopic thermodynamic fluctuations, and

to introduce the new concept of exergy. In next Section 1.5, this concept will be explained, and will be linked to the CERES system, since it works in accumulator-mode (A-mode) (or in harvesting-mode, H-mode) according to exergy creation (or destruction), which is associated with entropy consumption (or production).

1.5 Exergy

It is well known that energy cannot be created and destroyed but only transformed into other forms of energy; same thing is valid for the matter. The results of the conversions is the reduction of the quality, even if the quality can be locally improved, but at the cost that elsewhere the quality is deteriorated in a greater way. The successive reduction of the quality could be assumed as another fundamental law of physics. In Figure 1.20 is described how the energy/matter flows across a system, changing the quality level of the system itself.

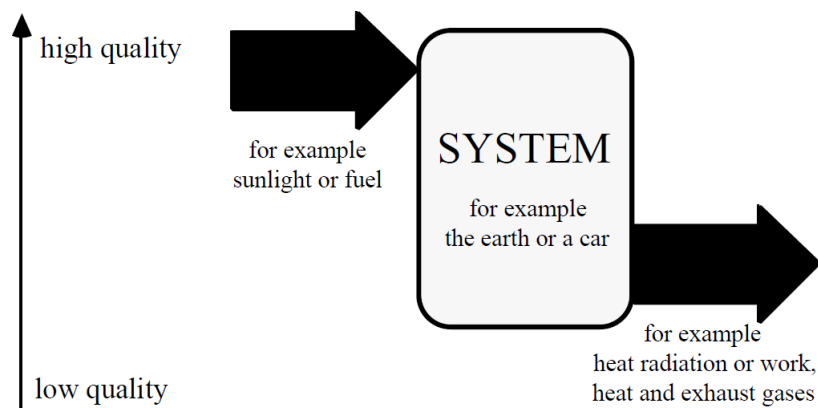


FIGURE 1.20: The moving force related to the energy/matter flow is the quality, which continuously deteriorate while the flow goes on; in this way a precise direction in space and time can be defined. It is possible to observe that only a small part of the flowing energy is stored inside the system (equilibrium condition between the input and output energy/matter) [53].

During the flow, the conversion of energy/matter yields necessarily to the production of entropy, whose amount is strongly influenced by the conversion rate (higher the conversion rate, higher is the entropy produced). Also the presence of losses during the conversion is a source of increasing entropy, which means that the process is irreversible: in ideal cases, reversible process could be settled, but in real world this is practically impossible, so the losses should be minimized as much as possible.

Furthermore, the concept of entropy is usually seen with a bad connotation, arising from the fact that it defined a lack of quality. For this reason, a new opposite concept was introduced, the negentropy or negative entropy $-S$. Its principle meaning is the amount of quality; when the quality reduces, also the negentropy decreases.

1.5.1 Exergy concept

The concept, and the term, of exergy was suggested by Zoran Rant in 1953 to determine the useful amount of energy able to perform a mechanical work [54]. But a complete definition of exergy was given by H. D. Baehr:

“Exergy is that part of energy that is convertible into all other forms of energy” [55].

In other words, exergy denotes the maximum mechanical work that can be extracted from the

	Form of Energy	Quality Index (exergy percentage)
Extra Superior	Potential Energy	100
	Kinetic Energy	100
	Electrical Energy	100
Superior	Chemical Energy	About 100 (corrected)
	Nuclear Energy	95 (corrected)
	Sunlight	93 (corrected)
	Hot Steam	60
	Districting Heating	30
Inferior	Waste Heat	5
Valueless	Heat radiation from Earth	0

TABLE 1.3: Here are reported the different quality values (fraction in percentage of Extra Superior Energy of total energy in question) for several energy forms, ordered from the one with the highest content of exergy towards the one with the lowest exergy content, which corresponds to the heat radiated from the Earth [53].

Form of Matter	Quality Index (exergy percentage)
Matter in an ordered form	100
Matter as commercial form	almost 100
Mixtures of elements	approximately 90
Rich mineral deposits	50-80
Ore approximately	50
Poor mineral deposits	20-50
Mineral dissolved in seawater or soil	approximately 0

TABLE 1.4: Here are reported the quality values (computed from Equation 1.56) for different matter structures, ordered from the one with the highest content of exergy towards the one with the lowest exergy content [53].

system placed in a certain environment; in particular this work is a sort of fully ordered energy (with $S=0$), that can be also transformed into other forms of energy. The exergy concept can be extended up to include matter and other concepts coming from thermodynamics, like the Gibb's Free Energy, Helmholtz's Free Energy and enthalpy. Sometimes exergy is used to measure the deviation of a system from its equilibrium state with the surrounding environment.

In the following Table 1.3, various energy forms and their relative quality indexes are reported; it is possible to notice how the the heat has the lower values of quality. Instead in Table 1.4 are reported different forms of matter and their relative percentage of exergy (quality). Furthermore, in Section A.3 is reported a detailed derivation of exergy.

1.5.2 Exergy content in materials

The exergy content of a material can be computed by means of the chemical potentials and the concentrations of the elements present in the system in actual and ground states.

In order to determine the exergy amount of materials, temperature and pressure are supposed

to be constant and in equilibrium with environment A_0 , so from Equation A.10:

$$E = \sum_i n_i (\mu_i - \mu_i^0) \quad (1.54)$$

Moreover, in chemistry the chemical potential μ_i is defined as follows:

$$\mu_i = \mu_{i0} + RT_0 \ln(a_i) \quad (1.55)$$

where a_i represents the activity for a specific element i , while μ_i^0 denotes the chemical potential reference state of for the same element i . Furthermore the activity is proportional to the concentration c_i . By using both Equations 1.55 and the proportionality of a_i with c_i , the following relationship is obtained:

$$E = \sum_i n_i (\mu_i^0 - \mu_{i0}^0) + RT_0 \sum_i n_i \ln \left(\frac{c_i}{c_{i0}} \right) \quad (1.56)$$

The latter expression can be rewritten into Equation 1.57 if only one single element is present:

$$E = n \left[\mu^0 - \mu_0^0 + \ln \left(\frac{c}{c_0} \right) \right] \quad (1.57)$$

1.5.3 Efficiency of exergy conversions

Generally speaking, a process in which exergy is converted shows a conversion rate $v \neq 0$ and is driven by a gradient $g \neq 0$; assuming a linear behaviour:

$$v = \varepsilon g \quad (1.58)$$

where ε is a constant independent of g . Equation 1.59 indicates the produced entropy (per unit of time) due to the conversion process has a quadratic dependence on v :

$$\frac{dS}{dt} = \chi \varepsilon^2 \quad (1.59)$$

χ is independent on v , and its minimum value χ_0 corresponds to the minimum possible value of entropy production per unit time for the conversion from the initial to the final form of energy:

$$\left(\frac{dS}{dt} \right)_{min} (v) = \chi_0 \varepsilon^2 \quad (1.60a)$$

$$T_0 \left(\frac{dS}{dt} \right)_{min} (v) = T_0 \chi_0 \varepsilon^2 \quad (1.60b)$$

The product of T_0 with Equation 1.60a leads to a minimum exergy destruction per unit time. The maximum exergy per unit time that can be converted is:

$$v - T_0 \chi_0 v^2 \quad (1.61)$$

At this point, the maximal exergy efficiency related to the conversion rate v is presented here:

$$\eta_{max}(v) = 1 - \frac{v}{v_0} \quad (1.62)$$

where v_0 is defined as the characteristic power of the conversion process:

$$v_0 = \frac{1}{T_0 \chi_0} \quad (1.63)$$

By merging together Equations 1.61-1.62 and introducing in Equation 1.64 a relative exergy efficiency η_{rel} for conversion process with $v \neq 0$:

$$\eta_{ex} = \eta_{rel} \cdot \eta_{max}(v) \quad (1.64)$$

1.5.4 Exergy and information theory

Thermodynamics is that branch of physics dealing with systems formed by many particles: having a full and detailed comprehension about the motion of all the particles is practically impossible, but thank to the statistical mechanics, a way to get information on average properties (coming from the motion of particles forming the material under question) there exists. In particular this is referred to the Information Theory developed by Shannon, and based on the concept of incomplete information in a specific system. However, Edwin Thompson Jaynes solved the problem of how treat the available and incomplete information [56], and these concepts can be extended also to other fields of study, even if they were especially developed for statistical mechanics.

Considering a system made of N particles, the number of possible states Ω has an exponential behaviour with respect to the number of particles forming the system; the probability of the j -th state is P_j , which must satisfy the following fundamental principle of probability:

$$P = \sum_{j=1}^{\Omega} P_j = 1 \quad (1.65)$$

From Equation 1.65 can also be derived the entropy:

$$S = -k_B \sum_{j=1}^{\Omega} P_j \ln(P_j) \quad (1.66)$$

Then, moving at equilibrium states described by probabilities P_j^0 , the entropy reaches its maximum value, expressed in Equation 1.67:

$$S_{eq} = S_{max} = -k_B \sum_{j=1}^{\Omega} P_j^0 \ln(P_j^0) \quad (1.67)$$

Instead, the negentropy is defined as follows:

$$S_{eq} - S = k_B \left[\sum_{j=1}^{\Omega} P_j \ln(P_j) - \sum_{j=1}^{\Omega} P_j^0 \ln(P_j^0) \right] \quad (1.68)$$

In order to determine the information content in binary units (bits), Equation 1.69 should be used:

$$I = \frac{1}{\ln 2} \left[\sum_{j=1}^{\Omega} P_j \ln(P_j) - \sum_{j=1}^{\Omega} P_j^0 \ln(P_j^0) \right] \quad (1.69)$$

In this way, a system consisting of N particles with only two available states each, gives $\Omega = 2^N$ total states, each with probability $P_j^0 = 2^{-N}$ at equilibrium; complete information corresponds to $I = N$. It follows that negentropy and information are related by Equation 1.70:

$$S_{eq} - S = k_B \ln 2 \cdot I \quad (1.70)$$

From the latter it is possible to notice that one bit of information corresponds to a negentropy value equal to $\Sigma = 1.0 \times 10^{-23}$ J/K. Considering now Equation A.13, the relation between exergy E and I is:

$$E = T_0(S_{eq} - S) = k_B \ln 2 \cdot T_0 I \quad (1.71)$$

where the exergy related to one single bit of information (at room temperature) is $E = 2.9 \times 10^{-21}$ J.

In conclusion it is important to underline that the term information can be also used with the meaning of information capacity or measure of order (structure), rather than the common real information.

1.5.5 Exergy, Information Theory and Fluctuation Theorem

The equations presented in the previous section can be analysed more deeply in order to observe some hidden behaviours, also related to CERES itself. From Equation 1.47 it is possible to see how the entropy variation can decrease (the negentropy instead will increase), and by referring to Equation 1.70, also the information I will consequently improve: in the end, the exergy of the system under question will arise (Equation 1.71). On the contrary, if the entropy change is positive, information I will decrease, together with exergy.

From this should be clear that in A-mode the exergy will be accumulated thanks to a phase change process activating the energy storage, while in H-mode the exergy will be destroyed when necessary (converted to kinetic or electromagnetic energy, for example). This exergy creation/destruction are linked to a very interesting concept, enlightened by R.D. Robinett and D.G. Wilson [57]: representing the thermodynamics with a hamiltonian, they stated that exergy at physical level is equivalent to exergy at information level. In this way it is possible a direct conversion between information and exergy, so that an exergy destruction (extraction of work) corresponds to an erasing of a state (*e.g.* information decreases).

1.5.6 Exergy in systems far from equilibrium

If a system A (Figure 1.21) should be kept far from equilibrium only if it is crossed by an energy flow, and the received energy from one system is passed away to another system.

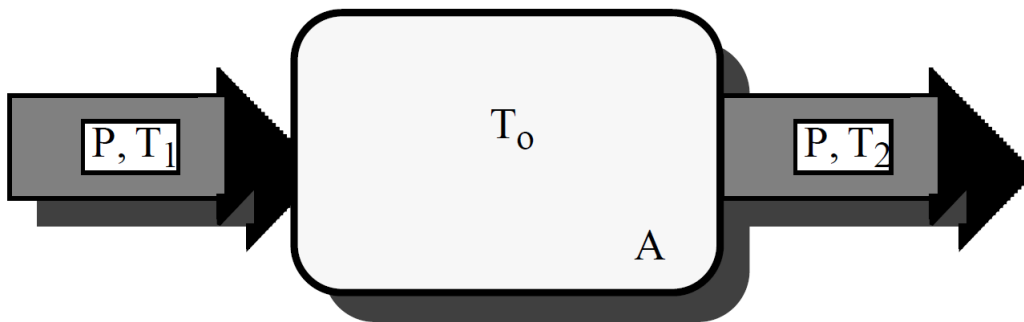


FIGURE 1.21: The system A , at temperature T_0 and energy flow P [53].

In addition, the energy inlet (at T_1) transports small values of entropy, while the energy outlet (at T_2) has higher values of entropy. Considering a power flow P and an average temperature T_0 for the system A , the net exergy gain W per unit time will be:

$$W = T_0 P \left(\frac{1}{T_2} - \frac{1}{T_1} \right) \quad (1.72)$$

Equation 1.72 is a fundamental relationship to maintain systems far from equilibrium.

In living organism, the death represents the equilibrium conditions, and these organism (human beings included) are always far from the equilibrium (until they will live) by consuming (chemical) energy extracted when feeding themselves and converting it into waste (usually under the form of simple heat radiated towards the environment). But if the deviation from equilibrium conditions is not so large, and the system is placed among steady-state giver and steady-state receiver, it moves towards a stationary state described by by a minimal entropy production (Equation 1.73):

$$\frac{\delta}{\delta X_i} \left(\frac{dS}{dt} \right) = 0 \quad (1.73)$$

where $X_i = X_i(\vec{x}, t)$ is a whatever intensive variable within system A .

The negentropy flow of a catalytic system (enclosed into a shell) can be settled is possible, and the fluctuations can be used as starting point for producing structures (and order) where a chaotic state is present: in this way the life occurred and developed for the first time on Earth millions of years ago.

1.6 Conclusions

The aim of this brief report about the CERES systems and DOUGHNUTs, is to present how they can be produced and the way they should operate. A particular attention was given on the physical principles which are the basis of the CERES, especially the ones related to the ferrofluids contained inside a protective shell. The advantages of using a liquid (smart) material are revolutionary, in particular for the space exploration of giant gas planets thanks to the ability of the DOUGHNUT to operate in two different modes: as energy accumulator depending on the internal state of the fluid, or as energy harvester using a thermal gradient (or an external electromagnetic field).

Even if research progress in this revolutionary field is quite advanced about how a smart fluid system should theoretically work, however, from a practical point of view no experiment has been conducted in order to develop a complete autonomous system. In this way, the next step to be carried on should be an attempt to make some steps forward into the world of liquid robotics.

Chapter 2

Experimental Setup

2.1 General Overview

The CERES Systems consists of a quite complex experimental setup, where different apparatus and devices have to coexist. In particular the overall system must have a power supply network, used to turn on the thermal gradients, the measurement devices and the acquisition system.

2.2 FF: magnetism and properties

2.2.1 Magnetism

In Paragraph 1.3.2, Equation 1.7 was supposed for a paramagnetic system, but since the FF used will be based on magnetite, the system will be ferromagnetic up to the Curie Temperature T_C . In details, there are three types of magnetism, known as ferromagnetism, ferrimagnetism and antiferromagnetism, whose ferromagnetism denotes the strongest interactions. In each type the magnetic domains inside the material are all aligned along the same direction, resulting in a net magnetization; in Figure 2.1 the different situations are reported.

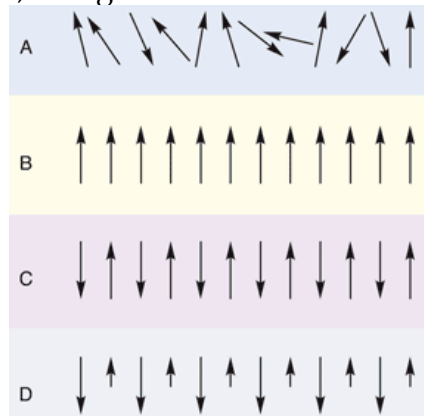


FIGURE 2.1: Different types of magnetism in materials: **A)** In paramagnetism the magnetic moments are randomly aligned in absence of a magnetic field (this is also the case of ferromagnets above T_C); **B)** Ferromagnetism show all moments aligned and with the same intensity in absence of a magnetic field (or is the case of paramagnets in presence of an external magnetic field); **C)** Antiferromagnetism presents magnetic domains aligned in opposite direction, but with the same intensity, so that the total resulting magnetization is null; **D)** Ferrimagnetism is similar to antiferromagnetism, but in this case the opposite magnetic moments have different amplitudes, and consequently the resulting magnetization is not zero [58].

FFs are ferromagnetic (below T_C), and since in our case we will use magnetite, which remains ferromagnetic in a large range of temperature, the system will not become paramagnetic. In Table 2.1 are reported the Curie temperatures of some ferromagnetic materials widely used, included Fe_2O_3 present in the FF that we will use.

Material	Curie Temperature [K]
Co	1388
Fe	1043
Fe_2O_3	948
Ni	627
CrO_2	386
Gd	292

TABLE 2.1: The Curie temperatures of different ferromagnetic materials [59].

2.2.2 Constant volume

The volume of the FF subjected to a thermal gradient can be considered nearly constant since, according to [60] the thermal expansion coefficient α is very small and constant in range 100 K to 300 K:

$$\alpha = (1.2 \pm 2) \times 10^{-4} \text{ K}^{-1}$$

Moreover, the density of magnetite NPs slightly decreases in range 10 °C to 80 °C, and is reported in Table 2.2:

Temperature [°C]	Density [kg/m ³]
10	2462
20	2458
30	2453
40	2448
50	2443
60	2439
70	2434
80	2429

TABLE 2.2: Density values for magnetite/oleic acid aggregates for different increasing temperatures [61].

2.2.3 Pressure

The pressure inside a tube filled with FF will depend on the distance of the FF from the permanent magnets placed around the tube. Figure 2.2 indicates how the FF pressure reduces when increasing the distance from the magnets (regardless of their polarity).

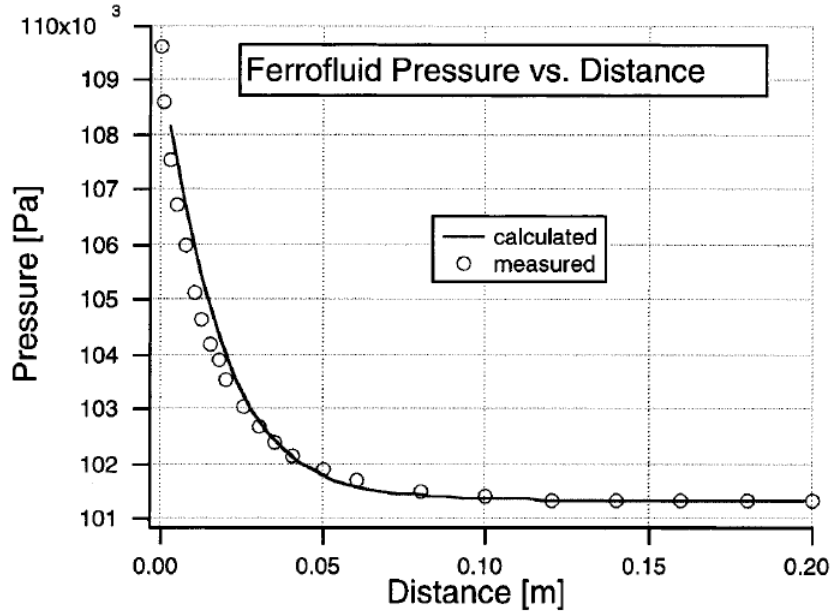


FIGURE 2.2: Theoretical and experimental FF pressure plotted against the distance of the permanent magnets [62].

2.2.4 Nanoparticles

For our experiment we will use two types of FFs by *Ferrotec*, EMG 911 and EFH1, with average particle dimensions around 10 nm (other properties in Table 2.3).

FFs Properties	EMG 911	EFH1
<i>Appearance</i>	Black-brown fluid	Black-brown fluid
<i>Carrier Liquid</i>	Light hydrocarbon oil	Light hydrocarbon oil
<i>Nominal Particle Diameter</i>	10 nm	10 nm
<i>Magnetic Particle Concentration</i>	2.0 % vol	7.9 % vol
<i>Flash Point</i>	89 °C	92 °C
<i>Pour Point</i>	−94 °C	−94 °C
<i>Volatility (1 h @ 50 °C)</i>	9.0 %	9.0 %
<i>Relative Magnetic Permeability @ 20 Oe</i>	--	2.6
<i>Saturation Magnetization</i>	11 mT	44 mT
<i>Viscosity @ 27 °C</i>	6 mPa s	≤12 mPa s
<i>Initial Magnetic Susceptibility</i>	0.5	2.64
<i>Density</i>	$0.89 \times 10^3 \text{ kg/m}^3$	$1.21 \times 10^3 \text{ kg/m}^3$
<i>Surface Tension</i>	68 mN/m	29 mN/m

TABLE 2.3: Properties of EMG 911 and EFH1 FFs by *Ferrotec* [63][64].

Focusing on the EMG 911 characterization made by *Tobias Kruse et al.* [65], it is possible to analyse the behaviour of cluster formation in FFs. Considering the particles nominal radius $R=0.2 \text{ nm}$, and supposing a surfactant layer thickness $s = 0.2 \text{ nm}$, the distance between the two centres of the NPs is $d_c = 2(R + s) \approx 10 \text{ nm}$ (Figure 2.3).

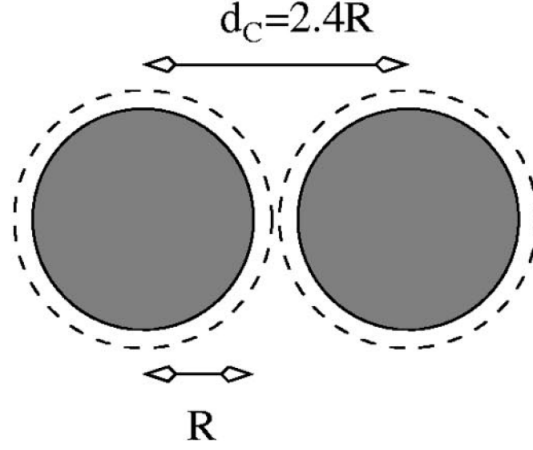


FIGURE 2.3: Graphical representation of two interacting NPs, with radius R and reciprocal distance d_c between their centres [65].

In FFs, the interaction energies depend on both particles radii and distances, and particularly the magnetic dipole-dipole interaction should be the responsible for the clusters formation (also at long range). When considering two particles with parallel magnetic dipole moments at saturation magnetization, whose radii are R_1 and R_2 at mutual distance d_c , the interaction energy will be:

$$E_{\parallel}^{dd} = -2 \cdot \frac{\mu_0}{4\pi} \cdot \frac{\mu_1 \mu_2}{d_c^3} \propto \left(\frac{R_1 R_2}{d_c} \right)^3 \quad (2.1a)$$

$$\mu_i = \frac{4}{3}\pi \cdot \left(\frac{M_p}{\mu_0} \right) \cdot R_i^3 \quad (2.1b)$$

where μ_i represents the magnetic dipole moment of i -th particle and M_p the relative saturation magnetization. Generally, the dipole-dipole interaction is negligible for small particles, while becomes relevant for larger particles, showing a stronger tendency to form clusters. This agglomeration behaviour can be described by an aggregation parameter λ (Equation 2.2), determined by the ratio among the magnetic dipole-dipole interaction and the thermal energy:

$$\lambda = \frac{1}{2} \cdot \frac{|E_{\parallel}^{dd}|}{k_B T} \quad (2.2)$$

from which it is possible to see that the aggregation will increase with larger particle sizes and lower temperatures (less thermal agitation). A simple numerical analysis can be performed supposing two particles with radii $R_1=R_2=4.5$ nm, $d_c=10$ nm and $M_p=402.5$ mT:

$$|E_{\parallel}^{dd}| = 3 \times 10^{-21} \text{ J} = 0.019 \text{ eV} \quad (2.3)$$

which is less than thermal energy $E_{th} = 0.026$ eV. Since $E_{\parallel}^{dd} < E_{th}$, the dipole-dipole interaction is not sufficient to create thermally stable clusters; this translates into an average aggregation parameter $\bar{\lambda} \approx 0.37$. However, in order to have thermal stability is required that $\lambda \geq 1$: this means that such small particles can only form clusters with large particles, whose radius can be determined transforming Equation 2.2 into Equation 2.4a, and then getting also Equation 2.4b, which defines the minimum radius length to have particles aggregation at a given temperature T :

$$\lambda = \left(\frac{R_1 \cdot R_2}{d_c \cdot R_{limit}} \right)^3 \quad (2.4a)$$

$$R_{limit} = \sqrt[3]{\frac{9\mu_0 k_B T}{4\pi M_p^2}} \quad (2.4b)$$

In case of room temperature, $R_{limit} \leq 2.8$ nm. As a consequence, particles with radius lower than R_{limit} can never form aggregates with other particles, whatever is their size, and holding the condition $\lambda \geq 1$. The higher the boundary on thermal stability, the lower the fraction of particles able to form clusters (achieving the dipole-dipole interaction). Considering again $R_1 = 4.5$ nm, $\lambda \geq 1$ can be reached only if particle comes close to a second particle with $R_2 > 9$ nm, for $\lambda \geq 4$ even $R_2 > 440$ nm (assuming $d_c \geq R_1 + R_2 + 1$ nm). This means that only a quite reduced portion of particles is able to form clusters, while the great majority of them remain monodispersed. On the contrary, the experimental measurement performed by Kruse (Figure 2.4) denotes that all particles contribute to the aggregates: there should be an additional mechanism providing the necessary bonding energy, which corresponds to the Van der Waals interaction.

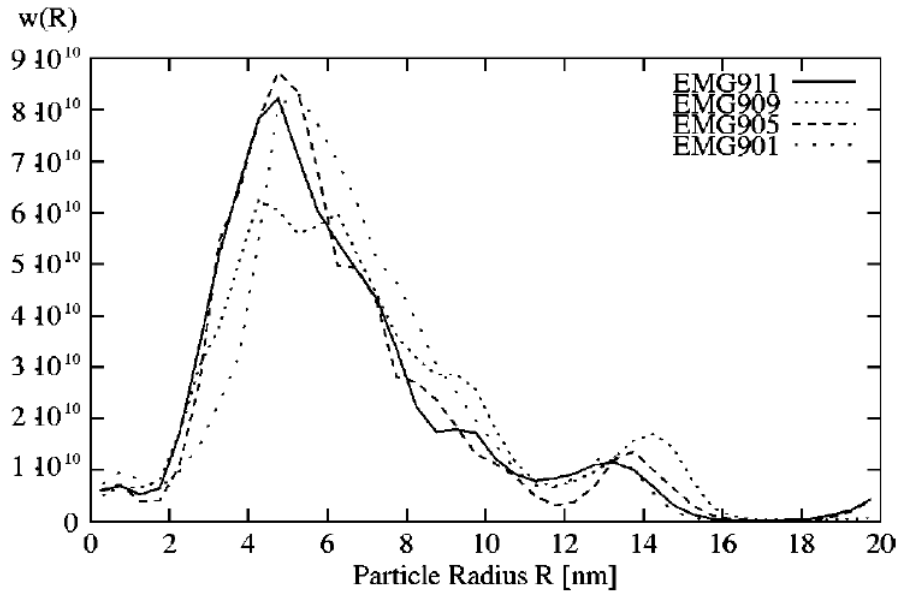


FIGURE 2.4: Normalized size distribution of Fe_2O_3 particles. After the normalization, $w(R)dR$ is equal to the volume fraction of particles with radius R [65].

When aggregate have short surface-to-surface distances ($2s = d_c - R_1 - R_2$), the Van der Waals interaction can overcome the magnetic dipole-dipole interaction; in particular:

$$E_{Waals} = -\frac{A_H}{6} \left[\frac{2R_1 R_2}{d_c^2 - (R_1 + R_2)^2} + \frac{2R_1 R_2}{d_c^2 - (R_1 - R_2)^2} + \ln \left(\frac{d_c^2 - (R_1 + R_2)^2}{d_c^2 - (R_1 - R_2)^2} \right) \right] \quad (2.5)$$

where the Hamaker constant A_H ranges from 0.19 eV to 1.9 eV. Always considering $R_1 = R_2 = 4.5$ nm and $d_c = 10$ nm, and that $A_H \geq 0.19$ eV, the following inequality is obtained:

$$|E_{Waals}| = 4.5 \times 10^{-21} \text{ J} = 0.028 \text{ eV} \quad (2.6)$$

resulting that $|E_{Waals}| > |E_{||}^{dd}|$, so $|E_{Waals} + E_{||}^{dd}| \geq 0.047$ eV which leads to Equation 2.7:

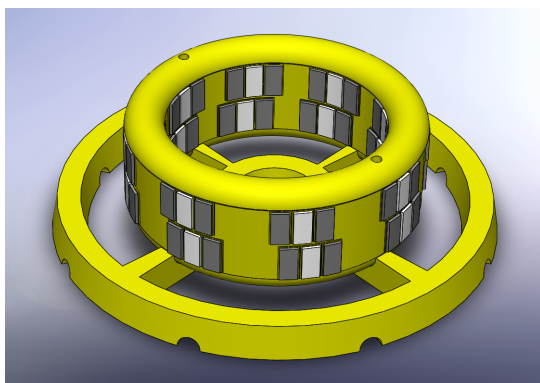
$$\lambda_{total} = \frac{|E_{Waals} + E_{||}^{dd}|}{2k_B T} \approx 1 \quad (2.7)$$

In this case, thermal stability is reached even at room temperature, since the generalized aggregation parameter is nearly 1, still depending on the particle size and increasing with size. As consequence, also small NPs can become thermally stable and start forming clusters.

In conclusion, the first step in cluster formation in FFs at long particle distances is dominated by thermal energy and dipole-dipole interactions, while the small particles can aggregate once they are close together only if there is an additional interaction energy (*i.g.* Van der Waals energy), necessary to achieve thermal stability. Surely, also the carrier liquid and particle coating have an important microscopic role in the aggregation of clusters, probably depending of their chemical and physical properties.

2.3 CERES Reactor

The fundamental part of the system is for sure the CERES reactor. This device consists of a 3D printed torus made of PLA. In this first prototype the lateral walls are vertical and not curved as in an ideal torus, since they are simpler to be printed. Moreover, the ring is placed on a circular support, itself made of PLA. In Figure 2.5(a) is reported the virtual rendering of the CERES system, made with Solidworks™. Both the structures were previously designed



(a) Virtual rendering of CERES system.



(b) The 3D printed CERES system.

FIGURE 2.5: The CERES reactor: virtual rendering and real system.

with a CAD, in this case SolidWorks, and then printed by Politronica (Figure 2.5(b)). As already said, the material used is PLA, with a FDM (Fused Deposition Modeling) machine for rapid prototyping, one of the most utilized technique in the modern field of AM (Additive Manufacturing).

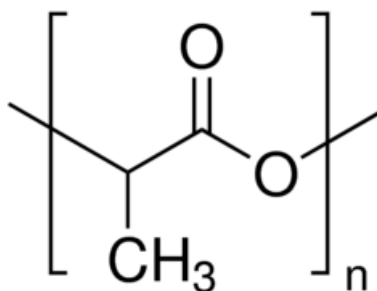


FIGURE 2.6: The chemical structure of the PLA [66].

The size of the PLA filament was around 250 μm , and the whole 3D-printing process lasted around 38 h. In Table 2.4 are reported the most relevant dimensions of the structure.

Parameters	Size
<i>External radius</i>	140 mm
<i>Internal radius</i>	110 mm
<i>Height</i>	85 mm
<i>Cavity</i>	20 mm
<i>Wall thickness</i>	5 mm
<i>Bottom/lid height</i>	20 mm

TABLE 2.4: Main sizes of CERES structure.

2.3.1 Magnets

The permanent magnets (Figure 2.7) are made of a particular alloy, called ALNICO (ALuminium-NICKel-COBalt). The magnets present the shape of a parallelepiped, whose dimensions are:

$$30 \pm 0.1 \text{ mm} \times 15 \pm 0.1 \text{ mm} \times 3 \pm 0.1 \text{ mm}$$

The magnetization of each magnets is axial through the thickness, at an height of 3 mm. These magnets will be attached on the outer walls of the CERES ring, and will be very useful to create a cyclic motion inside the reactor. Quite probably, the magnets will be substituted by solneoids in the next prototypes.

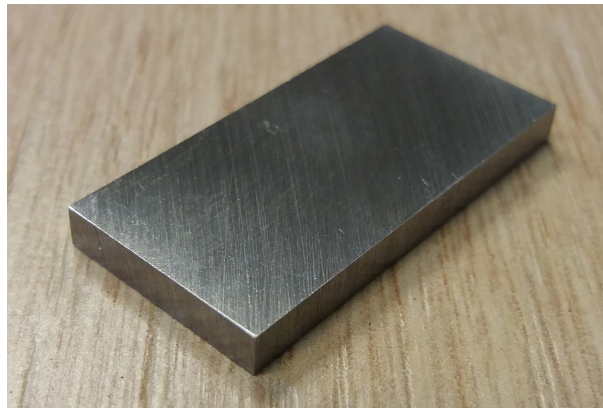


FIGURE 2.7: One of the ALNICO magnets, successively installed all around the CERES ring.

Moreover, in order to facilitate the starting motion of the FF during the experiments, an independent power supply (Figure 2.8) is connected to two solenoids made by the coils (one is toroidal with respect to the reactor, and the other one is poloidal).



FIGURE 2.8: The power supply SPD 3606 by GW-INSTEK, used to push the motion of the FF at early stages.

2.3.2 Peltier Modules

A Peltier module is a particular device acting as a sort of heat pump able to transfer heat from one side to the other one, by means of an electrical energy consumption; the direction of the heat flux is determined by the direction of the current. In Physics, this effect is known as *Peltier effect*, opposite to the *Seebeck effect*. The thermoelectric effects will be explained just below, referring to [67].

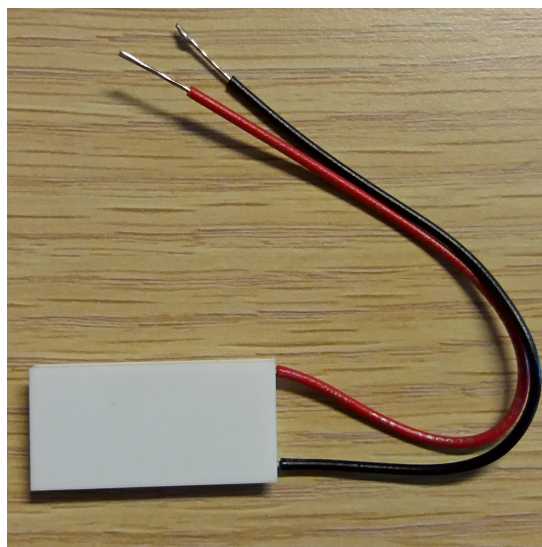


FIGURE 2.9: The Peltier module that is used for the CERES Project; a module is composed of many junctions in series.

The Peltier modules will be placed on the inner and outer walls of the reactor, alternated by permanent magnets; when power up, they will create a thermal gradient in the FF, starting its cyclic motion inside the CERES system.

Peltier Effect

In 1834, the French physicist Jean Charles Athanase Peltier (1785-1845) discovered that, when a current was flowing across the junction between two dissimilar conductors A and B (or semiconductors), heat was generated or removed at the junction itself.

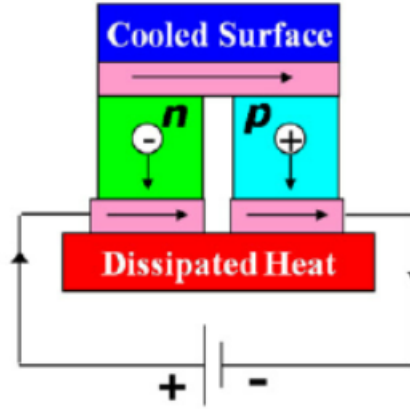


FIGURE 2.10: A scheme representing how the Peltier effect acts, considering n-doped and p-doped semiconductors: applying a voltage, it is possible to heat and cool the two sides of the module [68].

Each material has its own *Peltier coefficient* π [V], which represents the amount of heat carried per unit of charge, and is defined as follows:

$$\pi = I/Q \quad (2.8)$$

In particular, $\pi > 0$ if A is heated and B is cooled, otherwise $\pi < 0$ if A is cooled and B is heated.

Seebeck Effect

This effect was originally discovered by Alessandro Volta in 1794, but it was named Seebeck effect after Thomas Johann Seebeck independently rediscovered it in 1821. In his experiments, Seebeck observed that inside a circuit made of two dissimilar conductors, with junctions at different temperatures, was possible to measure an electric potential difference (voltage), driving a current in the closed circuit **caltech**. The voltage produced is proportional to the thermal gradient by means of the Seebeck coefficient S [$\mu\text{V}/\text{K}$], also known as thermopower, and reported in Equation 2.9:

$$V_{emf} = S \cdot \Delta T = S \cdot (T_{hot} - T_{cool}) \quad (2.9)$$

In 1851 Gustav Magnus discovered that the Seebeck voltage was independent of the temperature distribution inside the conductors, denoting the thermopower as a thermodynamic state function. Moreover, this is also the physical way to produce a thermocouple, a device used to measure the temperature, and for this aim used to measure the temperature of the FF inside the CERES reactor, as presented later in Section 2.6.1.

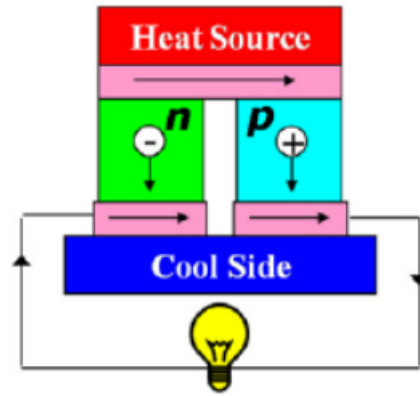


FIGURE 2.11: A scheme representing how the Seebeck effect acts, considering n-doped and p-doped semiconductors: applying a thermal gradient (heat and cool sides), it is possible to generate an induced electromotive force [68].

Here, in Figure 2.12 are reported some values of the Seebeck coefficient for different materials:

Metals	Seebeck Coefficient	Semiconductors	Seebeck Coefficient
	$\mu\text{V/K}$		$\mu\text{V/K}$
Antimony	47	Se	900
Nichrome	25	Te	500
Molybdenum	10	Si	440
Cadmium	7.5	Ge	300
Tungsten	7.5	n-type Bi_2Te_3	-230
Gold	6.5	p-type $\text{Bi}_{2-x}\text{Sb}_x\text{Te}_3$	300
Silver	6.5	p-type Sb_2Te_3	185
Copper	6.5	PbTe	-180
Rhodium	6.0	$\text{Pb}_{0.3}\text{Ge}_{0.30}\text{Se}_{0.58}$	1670
Tantalum	4.5	$\text{Pb}_{0.6}\text{Ge}_{0.36}\text{Se}_{0.58}$	1410
Lead	4.0	$\text{Pb}_{0.9}\text{Ge}_{0.33}\text{Se}_{0.58}$	-1360
Aluminum	3.5	$\text{Pb}_{1.3}\text{Ge}_{0.29}\text{Se}_{0.58}$	-1710
Carbon	3.0	$\text{Pb}_{1.5}\text{Ge}_{0.37}\text{Se}_{0.58}$	-1990
Mercury	0.6	SnSb_4Te_7	25
Platinum	0	SnBi_4Te_7	120
Sodium	-2.0	$\text{SnBi}_3\text{Sb}_1\text{Te}_7$	151
Potassium	-9.0	$\text{SnBi}_{2.5}\text{Sb}_{1.5}\text{Te}_7$	110
Nickel	-15	$\text{SnBi}_2\text{Sb}_2\text{Te}_7$	90
Constantan	-35	PbBi_4Te_7	-53
Bismuth	-72		

FIGURE 2.12: Here are reported some Seebeck coefficients for both metals and semiconductors [69].

Thomson Effect

Twenty years later, William Thomson (mainly known as Lord Kelvin) developed a comprehensive explanation of the thermoelectric effects, and their thermodynamical correlation. This resulted in the following relationship among the Peltier and Seebeck coefficients:

$$\pi = S \cdot T \quad (2.10)$$

Equation 2.10 led to a third thermoelectric effect, known as *Thomson Effect*: it states that heat is produced (or absorbed) when a current flows inside a metal conductor. The Thomson coefficient K is the proportionality constant between the current and the temperature gradient

(Equation 2.11), and is related to the Seebeck coefficient S (Equation 2.12):

$$Q = -K \vec{J} \cdot \nabla T \quad (2.11)$$

$$K = \frac{\partial \pi}{\partial T} - S = T \cdot \frac{\partial S}{\partial T} \quad (2.12)$$

where Q is the heat production rate per unit volume, \vec{J} is the current density and T the temperature.

2.4 Power Supply System

The CERES system requires a power supply system in order to switch on all the devices needed to create an elicoidal and cyclic motion of the FF inside the reactor, like the Peltier modules, but also to activate the sensors used to acquire the temperature of the FF and other output values. In this way, this Section 2.4 explains how the Power Supply System is built and the function of the devices installed.

2.4.1 Power Supplies

To power up all the 32 Peltier modules, 8 linear power supplies (produced by Bel, but commercialized by Power-One) properly plugged to the electric grid (220 V AC). The power supplies are grouped in two groups of 4 by means of screws present on their metallic supports; the metallic support is also used as electric GND, linking it to the right connector of the supply.

From the other connectors, cables are sent towards the voltage regulators: in particular each supply powers up 4 regulators, with a single output voltage of 12 V and 5.1 A as maximum output current.

For the sake of completeness, the case of each power supply has the following dimensions:

$$177.80 \text{ mm} \times 123.70 \text{ mm} \times 83.31 \text{ mm}$$



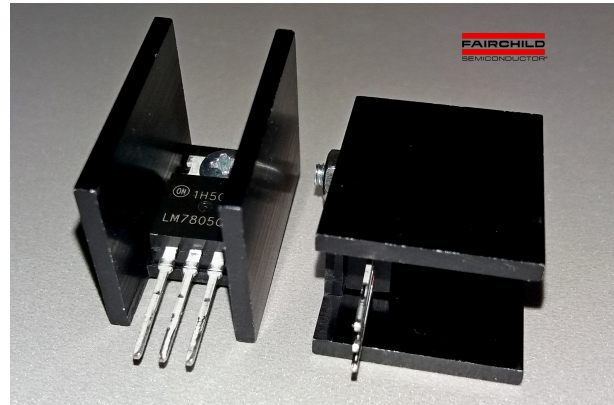
FIGURE 2.13: The power supplies from Bel used for CERES Project, united in groups of 4, front-side and back-side.

2.4.2 1st Stage Voltage Regulators

The 32 voltage regulators LM7805 by Fairchild are used to lower the output voltage (12 V) of the previous power supply stage. These regulators (Figure 2.14(a)) allow to get a typical output voltage reduced to 5 V, with an output current I_{Out} comprised between 5 mA and 1 A, with an output power $P_{Out} \leq 15$ W. Moreover, the voltage regulators can reach a very high temperature ($\approx 130^\circ\text{C}$) due to the large power dissipation; as a consequence, in order to keep low the temperature, a thermal dissipator is mounted on the heat sink of each regulator, as shown in Figure 2.14(b). To furthermore reduce the heat coming from these regulators, a medium size fan is installed near the circuits, providing a continuous air flux.



(a) Voltage regulators, front and back-side views.



(b) Voltage regulators with dissipator, front and backside views.

FIGURE 2.14: Examples of voltage regulators LM7805 by Fairchild.

2.4.3 2nd Stage Voltage Regulators

The output of each LM7805 voltage regulator is linked to the input of another voltage regulator, whose output voltage can be adjusted between 1.2 V and 3.3 V, depending on the resistors inserted in the circuit; the output current provided at the output can be up to 1.2 A. In total, 32 linear voltage regulators ADP7157 by Analog Devices are used. Moreover, it is important to notice the presence of an exposed pad on the bottom surface of the regulator, acting both as GND and thermal heat sink: from this, the need to solder it on the proper socket, an integrated circuit to adapt the linear regulator to the breadboard.

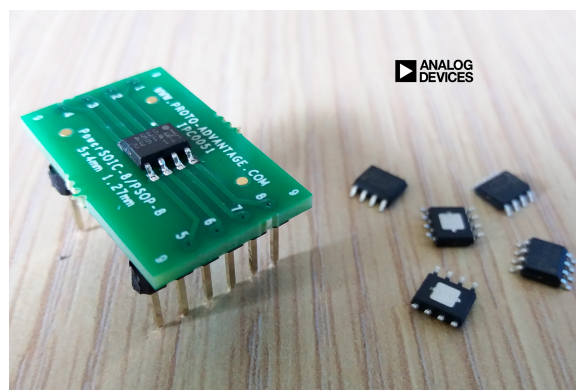


FIGURE 2.15: On the right, the ADP7157 linear voltage regulators standalone with the exposed pad (front-side and back-side), and on the left, one linear regulator soldered on the socket.

Each linear regulator circuit contains two $10\text{ k}\Omega$ resistors, and five $10\text{ }\mu\text{F}$ capacitors used to by-pass some pins to GND in order to have a lower noise. In this way, the measured output voltage is $V_{Out} \approx 2.34\text{ V}$, sufficient to power up one Peltier module.

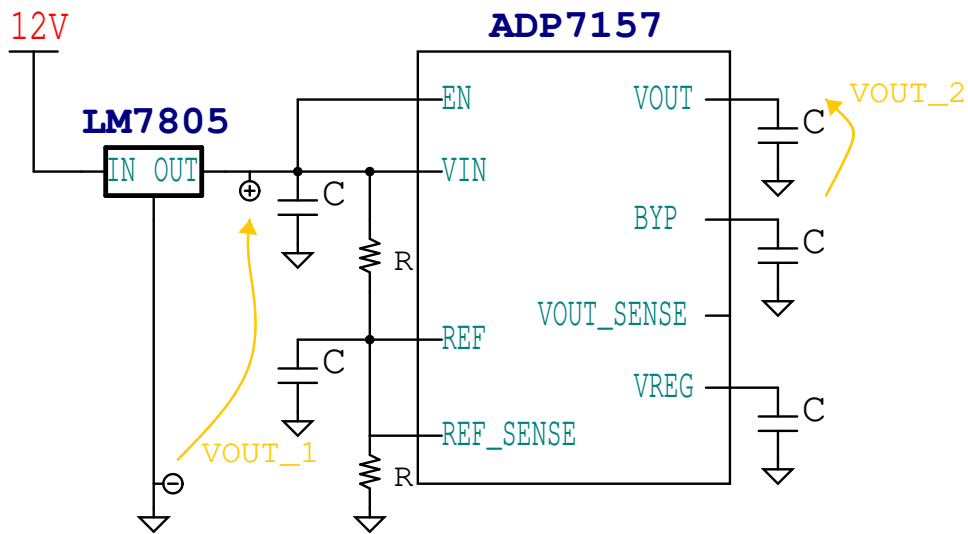


FIGURE 2.16: The schematic of the circuit implemented: the output of the power supply (12 V) is the input of the LM7805 (first stage of voltage regulators), which reduces the input voltage to 5 V (VOUT_1 in the schematic). At this point, the second stage of linear voltage regulators (ADP7157) lowers the 5 V at its input (VIN in the schematic) to 2.34 V (VOUT_2 in the schematic). The voltage divider, made by resistors $R = 10\text{ k}\Omega$, adjusts the output voltage at the desired value.

Moreover, the five capacitors $C = 10\text{ }\mu\text{F}$ are required to have low noise.

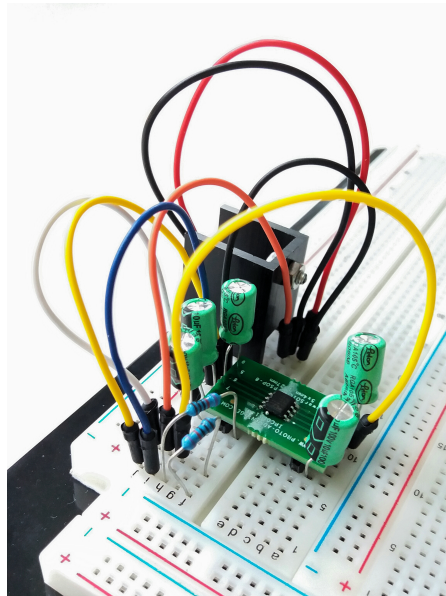


FIGURE 2.17: The real implementation on a breadboard of the circuit reported in the schematic of Figure 2.16. It is possible to notice the two resistors, the five capacitors, the LM7805 with its dissipator (behind) and the ADP7157 mounted on its IC socket. In addition, the coloured jumpers are used to make the circuitry connections. Here, the cables coming from the power supply are missing just for clarity reasons.

2.5 Extraction System

The CERES system aims to harvest energy from thermal gradients and cyclic motion of FF present inside the reactor. When the NPs are circularly moving along the ring, thanks also to the magnetic field generated by the permanent magnets installed all around the reactor, they produce fluctuations of the magnetic field (since they are magnetite NPs), so that it is possible to take advantage of this phenomenon in order to harvest energy.

In particular, this can be performed by means of a proper Extraction System, transforming the reactor into a sort of solenoid: in this way the varying magnetic field will produce an induced EMF (ElectroMotive Force) at the output of the system. Successively, the gained voltage potential, or the charge acquired, could be stored inside some supercapacitors, or other electrical systems.

2.5.1 The Faraday's Law

The electromagnetic induction phenomenon was discovered independently by Micheal Faraday (a British scientist) in 1831, and by Joseph Henry (an American scientist) the following year. However, Faraday was the first to publish the results of his experiment. The first public demonstration occurred on August 29, 1831: Faraday built a simple system consisting of a toroidal iron ring where two wires were wrapped around it (Figure 2.18).

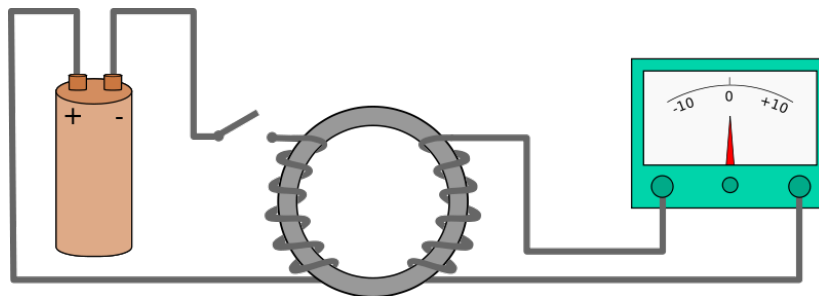


FIGURE 2.18: The apparatus realized by Micheal Faraday for the first public demonstration of his experiment [70]. The left side wire is connected to a battery, while the right one is plugged to a voltmeter, in order to measure the induced EMF on the right wire.

When the battery is disconnected from the left wire, no EMF can be read on the voltmeter, but closing the circuit, a current will flow in the left wire, inducing a transient in the current (and voltage) in the right wire, resulting in a measurable voltage on the voltmeter. This transient in current (or voltage) occurs also when the battery is disconnected. The phenomena (called by Faraday “*wave of electricity*”) are the results of a variation in the magnetic flux $\vec{\Phi}$, occurring when the battery is connected or disconnected.

A qualitative statement of the electromagnetic induction can be the following one:

“Faraday’s Law, which states that the electromotive force around a closed path is equal to the negative of the time rate of change of magnetic flux enclosed by the path” [71].

In order to better understand this explanation, a more quantitative analysis it can be possible taking advantage of [72].

The Faraday’s Law of electromagnetic induction can be expressed as follows:

$$\mathcal{E} = -\frac{d\vec{\Phi}}{dt} \quad (2.13)$$

where \mathcal{E} represents the EMF induced in the circuit, and $\vec{\Phi}$ is the magnetic flux. The latter is defined as reported in Equation 2.14, and can be better visualized in Figure 2.19.

$$\vec{\Phi} = \iint_{\Sigma} \vec{B} \cdot d\vec{\Sigma} \quad (2.14)$$

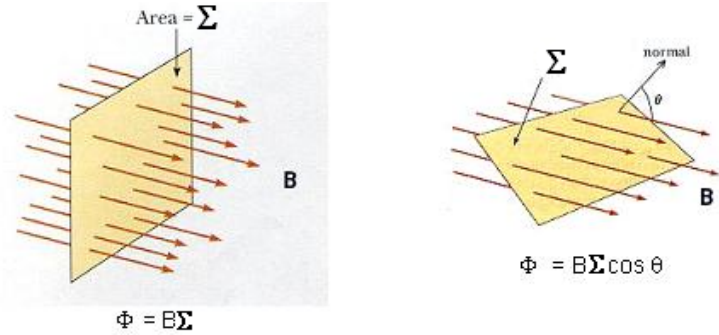


FIGURE 2.19: The magnetic flux $\vec{\Phi}$ across closed surface Σ . $\vec{\Phi}$ is proportional to the number of lines of force of \vec{B} (the red arrows), the magnetic flux density, passing through Σ . As a consequence, the magnetic flux changes if the magnetic flux density varies, or if the surface reduces or enlarges. A further possibility is to tilt the surface, or better, change the angle θ between the field \vec{B} and the versor orthogonal to the surface Σ [73].

At this point, should be remarked that the integral form of Equation 2.13 includes all possible cases (the simple form of Equation 2.13 instead suffers when treating motional cases), among which transformer EMF and motional EMF. In particular, transformer EMF denotes induced EMF due to changes of magnetic field intensity, while motional EMF is caused by moving parts of a circuit within a magnetic field.

Considering a possible change in the magnetic flux across Σ , the complete derivative of $\vec{\Phi}$ could be rewritten into:

$$\vec{\Phi} = \left(\frac{\partial \vec{\Phi}}{\partial t} \right)_{v=0} + \left(\frac{\partial \vec{\Phi}}{\partial t} \right)_{\vec{B}=\text{const}} \quad (2.15a)$$

$$\frac{d\vec{\Phi}}{dt} = \iint_{\vec{\Sigma}} \frac{\partial \vec{\Phi}}{\partial t} \cdot d\vec{\Sigma} - \oint_{\vec{\ell}} [\vec{v} \times \vec{B}] \cdot d\vec{\ell} \quad (2.15b)$$

where Equation 2.15b is Equation 2.15a if considered in standard notation; $\vec{\ell}$ is the path chosen, while \vec{v} is the speed of the moving part of the circuit.

Now, it is possible to get the comprehensive form of the Faraday's Law, if using Equation 2.13:

$$\mathcal{E} = - \iint_{\vec{\Sigma}} \frac{\partial \vec{\Phi}}{\partial t} \cdot d\vec{\Sigma} + \oint_{\vec{\ell}} [\vec{v} \times \vec{B}] \cdot d\vec{\ell} \quad (2.16)$$

Equation 2.16 clearly shows two separate terms, that will be detailed just below.

The first part, also called "volta-electric induction",

$$\mathcal{E}_{\text{transformer}} = - \iint_{\vec{\Sigma}} \frac{\partial \vec{\Phi}}{\partial t} \cdot d\vec{\Sigma} \quad (2.17)$$

describes the case of motionless (transformer) EMF, and corresponds also to the Maxwell's equation for the curl of the electric field \vec{E} , shown in Equation 2.18.

$$\nabla \times \vec{E} = -\frac{\partial \vec{B}}{\partial t} \quad (2.18)$$

The second term,

$$\mathcal{E}_{\text{motional}} = \oint_{\vec{\ell}} [\vec{v} \times \vec{B}] \cdot d\vec{\ell} \quad (2.19)$$

accounts instead as the motional term, known also as “*magneto-electric induction*”, origins from the definition of complete derivative and the Maxwell’s equation, reported just below.

$$\vec{B} \oint d\vec{\Sigma} = 0 \quad (2.20)$$

Moreover, the term inside the integral of Equation 2.19 gives origin to the Lorentz Force, defined in Equation 2.21:

$$\vec{F}_{\text{Lorentz}} = q [\vec{v} \times \vec{B}] \quad (2.21)$$

describing the magnetic force acting on a charge q moving at speed \vec{v} of the conductor, inside a magnetic field \vec{B} . In addition, the *Lenz’s Law*, formulated in 1834 by the Russian physicist of German ethnicity Emil Lenz, affirms that the direction of the induced current in a conductor by a varying magnetic field, creates a magnetic field that opposes to the initial changing magnetic field. In other words, it is the electromagnetic version of the Newton’s Third Law in classical dynamics, and is the explanation of the negative sign in Equation 2.13. Moreover, the Lenz’s Law gives information only about the direction of the induced current, without specifying its magnitude.

2.5.2 Coils

The Extraction System can be realized by rolling up a copper cable (or more) along all the reactor, in order to create a large number of coils. These coils will be the central element to produce the induced EMF, and to detect, at the extremities of the cable, a voltage, quantifiable with a proper voltage measurement system. In Figure 2.20 is reported the CERES reactor with the coils wrapped around it.

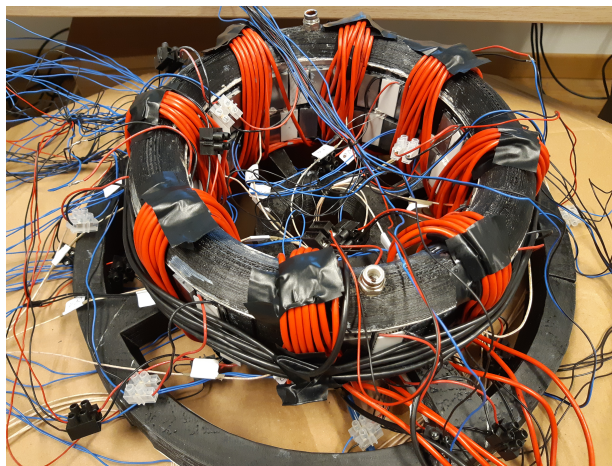


FIGURE 2.20: The coils are rolled up along the entire ring, in the free space among two adjacent Peltier stations; moreover the coils were tilted a little bit in order to have a better coupling between the magnetic field and the coils, resulting in a greater induced EMF. Moreover, it is possible to notice three layers of coils in the poloidal direction (red cables), and one in the toroidal direction (black cable): one red cable and the black one will be used to give an additional push to the FF at starting motion, while the remaining red cables will be connected in series and then to the output measurement system.

Considering that the length of the cable is $l \approx 15$ m, and the perimeter of the section of the CERES reactor corresponds to $p = 37$ cm, the resulting solenoid has approximately $N = 40$ coils, as reported in Equation 2.22:

$$N = \frac{l}{p} = 40 \quad (2.22)$$

Considering the *Ampère's Law*, which relates the integrated magnetic field around a closed loop to the current flowing inside the loop itself, it is possible to determine the current flowing inside a simple solenoid of N coils, knowing the magnetic field \vec{B} within it.

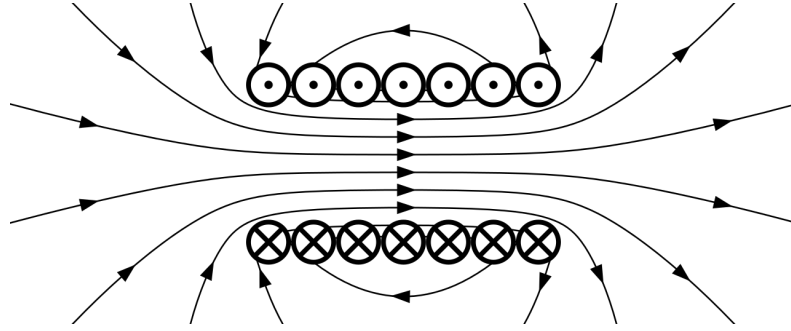


FIGURE 2.21: A graphical representation of the magnetic field created inside a solenoid with $N = 7$ coils. It can be seen that the magnetic field intensity is bigger inside the coils (lines of force are quite dense), while outside decreases drastically, thus, increasing the length of the solenoid, the confinement of the \vec{B} field is better. Furthermore, inside the solenoid the lines of force related to the magnetic field are parallel. Image taken from [70].

Considering the example of a solenoid in Figure 2.21, and computing the line integral of \vec{B} around a closed path γ of length $\vec{\ell}$ (Equation 2.23), where the horizontal components disappear, the current enclosed I_{enc} is obtained:

$$\oint_{\gamma} \vec{B} \cdot d\vec{\ell} = \mu_0 I_{enc} \quad (2.23)$$

Taking into account the number N of coils, and considering the equality $I_{enc} = I$, it is possible to write:

$$B\ell = N\mu_0 I \quad (2.24)$$

Moreover, the magnetic permeability μ_0 appears since the solenoid is in free space (air), thus, if a different material is inserted inside the core of the solenoid, the magnetic permeability will be affected by a variation, as presented in Equation 2.25:

$$\mu = \mu_r \cdot \mu_0 \quad (2.25)$$

Usually the relative magnetic permeability of a ferromagnetic material (magnetite NPs in case of CERES system) is $\mu_r > 1$, so that the resulting magnetic field B inside the solenoid shows an increase; as a consequence, Equation 2.24 rewrites into:

$$B\ell = N\mu_r\mu_0 I = N\mu I \quad (2.26)$$

After data collection, the latter should be verified in order to see if this approximation can be suitable and applied to CERES reactor to compute the output response of the entire system.

Next Paragraph 2.5.3 will describe the system for the measurement of extracted voltage.

2.5.3 Output Voltage Measurement System

The output voltage measurement system forms the so called extraction apparatus of the CERES system. It is composed of devices dedicated to the measurement of important electrical parameters, such as voltages, currents, resistances, inductances and capacitances. In particular, the instruments used are the precision LRC meter E4980A by Agilent (Figure 2.22), and the source meter 2635A by Keithley (Figure 2.23). Furthermore, these instruments are controlled by LabView™ programs, able to initiate (or end) the acquisition and collection of the data.



FIGURE 2.22: The Agilent E4980A LRC meter, with band-pass from 20 Hz to 2 MHz, and used to measure the inductive, capacitive and resistive behaviours of the extraction coils; in addition, the Agilent test fixture 16047A is inserted, in order to have a better coupling between coils and instrument.



FIGURE 2.23: The Keithley 2635A, a source meter used to measure the intensity of the current induced by EME, and flowing across the extraction coils.

2.6 Sensors

The CERES system has a very high degree of complexity, and in this way a certain number of sensors is required in order to keep under control some important parameters. In particular, one of the most relevant parameter is the temperature of the FF inside the reactor, as well the temperature reached by the Peltier modules.

According to this, the system is monitored by temperature sensors, like thermocouples and thermistors, better detailed in Paragraphs 2.6.1 and 2.6.2, respectively.

2.6.1 Thermocouples

A thermocouple is a temperature transducer based on a thermoelectric effect (Paragraph 2.3.2), in particular on the Seebeck Effect. For the sake of completeness, it is remarkable to remember that in a circuit made of two dissimilar conductors, and exposed to a thermal gradient, it is possible to measure a potential difference (voltage).

Taking advantage of this physical phenomenon as well of their low cost, the thermocouples are widely used to measure temperature. They can be used over a quite wide range of temperatures, even if their accuracy is not so precise (rarely it is possible to get an uncertainty lower than 1 °C) and their response is not linear; however they are standardized and can be easily substituted.

In Figure 2.24 is reported a graphical representation of a standard thermocouple.

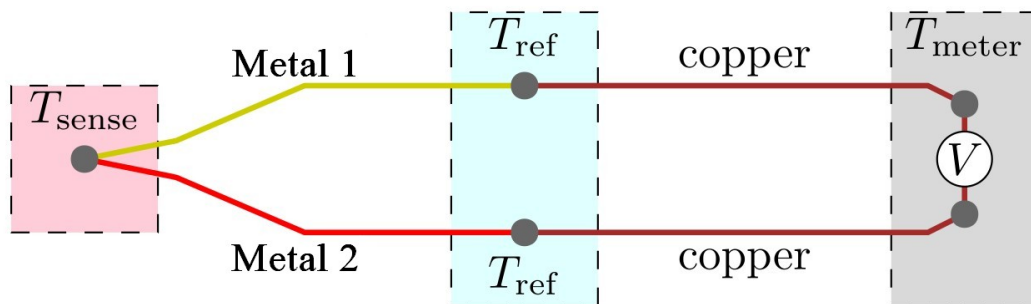
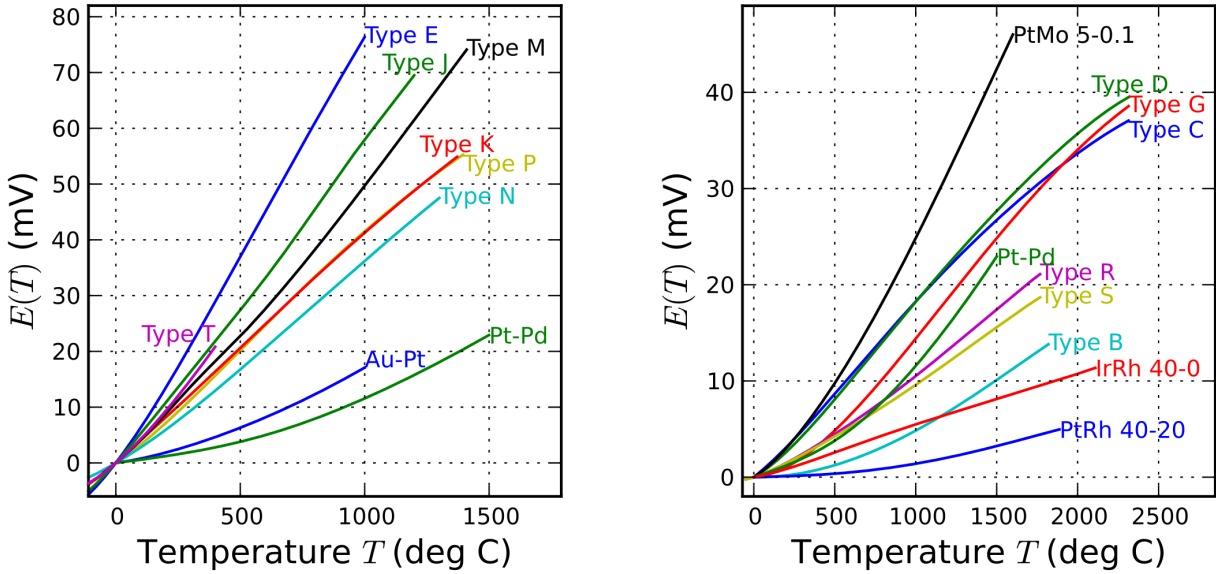


FIGURE 2.24: The circuitual representation of a traditional thermocouple. On the left it is possible to notice the so called *hot junction*, where the temperature is effectively measured, while the junction of Metal 1 and Metal 2 with the copper are said *cold junctions* and are used as reference temperature. This part of the thermocouple is connected with copper wires to the voltmeter, and the measured voltage can be translated into a corresponding temperature. In addition, assuming $T_{sense} > T_{ref}$, the positive electrode is listed firstly, followed by the negative one. Image taken from [70].

In reality, there are many kinds of thermocouples, differing one from the others by the metals used to form the junctions, or by the application field (industrial, medical, scientific...); the most famous (and used) thermocouples are types K, J, T, E, M, N and P. In Figure 2.25(a) are reported the characteristic functions of some well-used thermocouples. Otherwise, for very high temperatures, thermocouples B, R and S are often used (Figure 2.25(b)), since they are made of noble metals or alloys, and have a lower sensitivity. Moreover, they present a very high cost.



(a) The characteristic functions of some relevant thermocouples. The temperature range is intermediate, but differs from type to type, as well as the response (sensitivity and linearity) varies with the type. Image taken from [70].

(b) The characteristic functions of some thermocouples used for high temperature ranges. It can be easily noticed a lower sensitivity with respect to thermocouples for lower temperatures. Image taken from [70].

FIGURE 2.25: The characteristic functions of some most used thermocouples.

Moreover, the two cables made of dissimilar metals must be insulated from each other (except at hot sensing junction), and this can be performed with many materials, like plastics (for low temperatures), or ceramics (for high temperatures).

It is also important to report the general relationship between the temperature and the measured voltage:

$$\Delta T = \sum_{n=0}^N \alpha_n V^n \tag{2.27}$$

where in this polynomial equation the coefficients α_n depend on the materials of the wires, and N depends on the precision needed [74]. The 16 thermocouples used for the CERES system are of type N, sold from RS company, and are inserted all around the ring (8 for the inner wall and other 8 for the outer one), in order to measure the temperature (and the thermal gradient) of the FF. In Figure 2.26 is reported one of the thermocouples used.

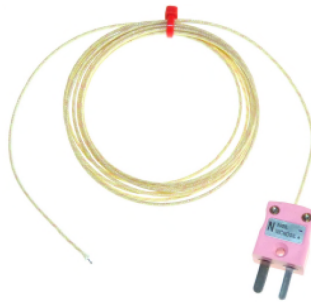


FIGURE 2.26: One of the thermocouples used for the CERES system. A glass fibre acts as an insulator between the two wires; in addition, the pink plug is removed in each device to have a better connection with the DAQ Acquisition System.

All the thermocouples installed on the reactor were properly calibrated, measuring the voltage values corresponding to a certain temperature (Figure 2.27); the obtained values are fitted with a polynomial curve (one for each thermocouple), and its coefficients are the α_n of Equation 2.27. Since the subsequent prototype will work for sure in range 0°C to 100°C , a linear fit can be considered as fully sufficient.

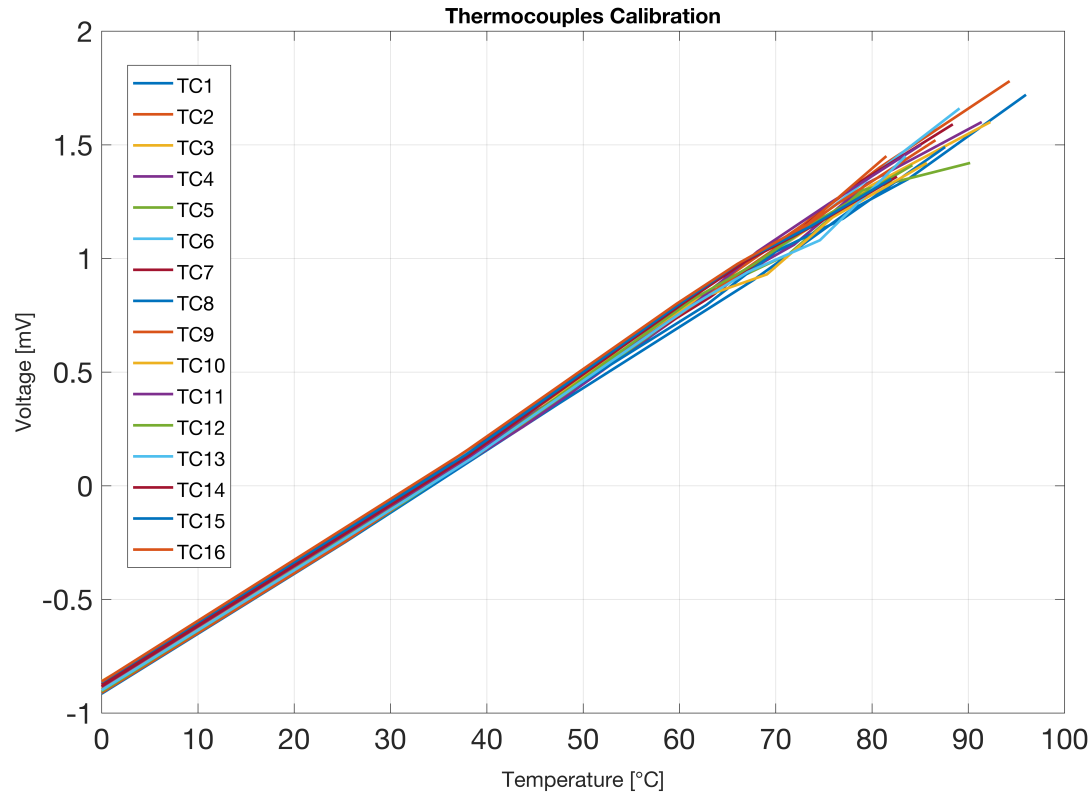


FIGURE 2.27: The Peltier module was calibrated immersing the sensor into hot water ($\approx 100^\circ\text{C}$), and measuring the corresponding voltage ($\leq 2\text{ mV}$); the process was repeated until the water became cold ($\approx 0^\circ\text{C}$), where the voltage dropped to few hundreds of μV . All 16 thermocouples (TCs) followed this procedure, and the relative voltage values were plotted here. As can be seen, the voltage response of these thermocouples can be treated as strictly linear.

2.6.2 Thermistors

The thermistors are used to monitor the temperature of the 16 Peltier stations: 8 are placed in the outer wall, and the remaining 8 in the inner one.

In particular, the thermistor is a device that acts as a sort of resistance thermometer, or in other words, a device which varies its internal resistance according to a change in temperature. Usually they are made of metallic oxides, encapsulated inside an impermeable and quite resistant epoxy, useful to protect the thermistor from the external environment. Furthermore, there exist two main types of thermistors:

- **NTC (Negative Temperature Coefficient):** the electrical resistance of the thermistor decreases when temperature is raised, while when temperature is lowered, the resistance increases; Usually, thermistors with NTC are the most used in application required temperature measurements.

- **PTC (Positive Temperature Coefficient):** the electrical resistance of the thermistor increases together with raising temperature, while lowers when temperature reduces. On the contrary, this type of thermistors are mainly employed as a fuse to protect circuits.

The thermistors ND03N00103KCC installed in the system are from RS-AVX company, and have a base resistance of 10 k Ω at 25 $^{\circ}\text{C}$; in Table 2.6 are reported the most relevant values of this device.



FIGURE 2.28: A picture of thermistor ND03N00103KCC by AVX (sold by RS), installed around the outer wall of the CERES ring.

Thermistor Properties	Value
<i>Series</i>	ND03
<i>Temperature Coefficient Type</i>	NTC
<i>Thermal Coefficient</i>	-4.6 %/ $^{\circ}\text{C}$
<i>Thermal Time Constant</i>	10 s
<i>Base Resistance at 25 $^{\circ}\text{C}$</i>	10 k Ω
<i>Maximum Dissipation at 25 $^{\circ}\text{C}$</i>	0.25 W
<i>Tolerance</i>	$\pm 10\%$
<i>Accuracy</i>	$\pm 3\%$
<i>Size</i>	3.5 mm(Dia.) \times 3 mm
<i>Min Operating Temperature</i>	-55 $^{\circ}\text{C}$
<i>Max Operating Temperature</i>	150 $^{\circ}\text{C}$

TABLE 2.5: Properties of thermistor ND03N00103KCC by RS-AVX [75].

The thermistor does not read directly anything, neither the temperature itself, but is its internal resistance that varies consequently to a change in temperature. The amount of variation depends on the material which the thermistor is made of. Unfortunately, the response of any thermistor is not linear, and the general behavior of these devices is depicted in Figure 2.29.

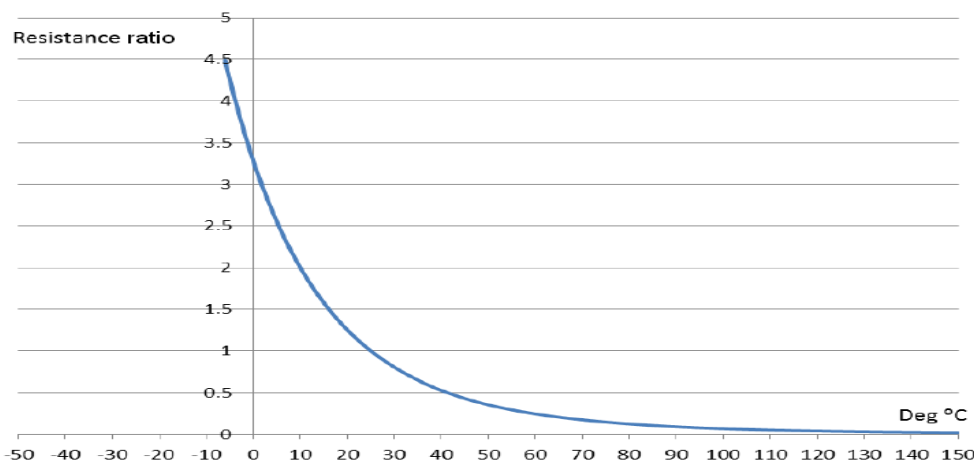


FIGURE 2.29: A picture showing the typical response of a thermistor; in this case a NTC example is reported, since the resistance decreases with temperature.

Since the temperature is better understood, the resistance is usually converted into temperature: the model used is called Steinhart-Hart equation (Equation 2.28), which relates thermistor's resistance to temperature. This equation was derived by John S. Steinhart and Stanley R. Hart in 1968, and sums up a mathematical model of the electrical resistance of a semiconductor for a varying temperature [76].

$$\frac{1}{T} = A + B \left[\ln \left(\frac{R_T}{R_{25}} \right) \right] + C \left[\ln \left(\frac{R_T}{R_{25}} \right) \right]^2 + D \left[\ln \left(\frac{R_T}{R_{25}} \right) \right]^3 + E \left[\ln \left(\frac{R_T}{R_{25}} \right) \right]^4 + \dots \quad (2.28)$$

where R_{25} is the electrical resistance of the thermistor at 25 °C, while R_T is the resistance at a certain temperature T , measured in [K]; then A , B , C , D and E denote the Steinhart-Hart coefficients, changing according to the type of thermistor and temperature range. For completeness, here is present also the term $\ln^2(R_T/R_{25})$, but in many cases it can be neglected, since it is very small with respect to the others.

With a closer look to Figure 2.29, the ratio among R_T and R_{25} changes as in Equation 2.29, meaning that for a typical application in range 0 °C to 100 °C, such as for the first experiment, the electrical resistance of the thermistor satisfies Equation 2.30.

$$\begin{cases} R_T/R_{25} = 2.28 \\ R_T/R_{25} = 0.06 \end{cases} \quad (2.29)$$

$$600 \Omega < R_T < 22.8 \text{ k}\Omega \quad (2.30)$$

It should be noticed that lower the temperature, higher the resistance value (and viceversa), as expected by a NTC thermistor.

Within the experimental setup, the thermistors are connected to a DAQ system, since it is necessary to read the temperature of each Peltier station; the corresponding schematic of a thermistor attached to the DAQ system is reported in Figure 2.30:

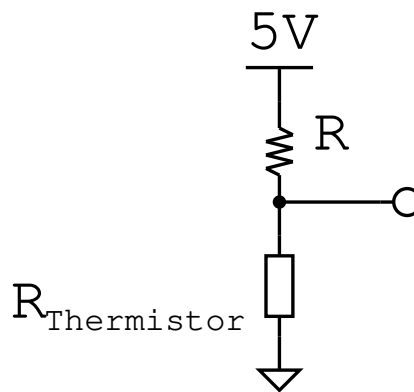


FIGURE 2.30: A circuitual representation of the connection between the thermistor and the DAQ system, used for the acquisition of the temperature values. A dedicated channel of DAQ provides 5 V, then, the potential difference on the thermistor is read thanks to a voltage divider between a resistance $R = 10 \text{ k}\Omega$ and the thermistor itself.

In next Section 2.7, the whole data acquisition system will be described, detailing both hardware and software used.

2.7 Data Acquisition System

The Data Acquisition System completes the experimental setup, and permits to acquire data from the temperature sensors installed around the CERES reactor.

It is composed of an hardware part, mainly a DAQ system by National Instruments, and of a LabView software to control the data collection. They will be described in Paragraphs 2.7.1 and 2.7.2, respectively.

2.7.1 Hardware

The DAQ system constitutes the most important component of the hardware of the overall acquisition system; in particular the acquisition system used is DAQ assistant NI 6289 by National Instruments® (Figure 2.31). It presents 32 channels (single ended) dedicated for the acquisition of analogical signals, that in this case will be fully occupied by 16 thermistors and 16 thermocouples.



FIGURE 2.31: A picture of NI 6289 DAQ acquisition system used.

Moreover, the DAQ assistant NI 6289 is connected to the USB port of a computer, on which is installed the LabView software. This software permits to control the DAQ system together with its sensors, and to collect data from them, and will be detailed in the subsequent Paragraph 2.7.2.

Feature	Value
<i>Type</i>	NI 6289
<i>Number of channels</i>	16 differential / 32 single ended
<i>Digital output</i>	48
<i>Analog output</i>	4
<i>ADC resolution</i>	18 bits
<i>Aggregate sample rate</i>	500 kS/s
<i>Timing resolution</i>	50 ns

TABLE 2.6: Properties of DAQ NI 6289 by National Instruments [77].

2.7.2 Software

The software used to control the DAQ system is LabView 2018. Opening the file `.vi` (vi stands for virtual instrument), a huge and complex set of blocks appears: this is the so called Block Diagram of LabView, where all the operations for running correctly the program are declared by means of function blocks. It is possible to define while and for cycles, if-else statements, blocks to separate or unite channels, and even blocks for computing mathematical equation and plotting graphs with acquired data. In Figure 2.32 is reported the whole program designed for the control of temperature sensors and data acquisition. Looking to Figure 2.32, the program acts as follows:

1. The DAQ block is used to acquire analogical signals, selecting the desired acquisition properties, like sample rate, channels to be used etc.. In addition, a start/stop button is defined in order to initiate (or interrupt) the acquisition of data. Then the 32 channels are divided into two groups, one for the thermocouples (16 channels) and one for the thermistors (16 channels remaining).
2. The thermistors channels contain resistance values that are properly converted into temperature ones by means of Steinhart-Hart equation; in order to perform this conversion, 16 function blocks are used. A similar process is done for the thermocouples, converting their electrical resistances into temperature values. After, the 16 thermocouples channels and the 16 thermistors channels are united and sent towards a Write to Measurement File block, in order to write the future collected data into a spreadsheet `.xlsx` file. Opening the Write to Measurement File block it is possible to chose the filename, the file format, and other many options.
3. All the numerical data acquired are also written in windows showing their instantaneous values, as well in graphs printing the temporal behaviour.

The block diagram window is not the only available in LabView™, but there exists also a Front Panel window, where are present the graphs showing the data collecting in real time (Figure 2.33). Moreover, after having pressed the run button (which compiles and starts the program at the same time), the start button must be pressed if one wants to see data on graphs when collected in real time. In particular, there are four graphs, two for the thermocouples (one for the inner wall fluid, one for the outer wall fluid) and two for the thermistors (one for the inner wall, one for the outer wall). There exist also 32 small windows (16 per each type of sensor) where are reported the instantaneous values acquired.

When the data collection must be ended, it is sufficient to press the stop button and the program stops to run; to see all the data collected it is possible to open the created file, located in the file path defined in the Write to Measurement File block. Then the data can be plotted with other program for data manipulations, like Origin or Matlab, and perform successive data analysis.

In next Chapter 3, detailed mathematical analysis will be presented, as well as some comments about the collected data.

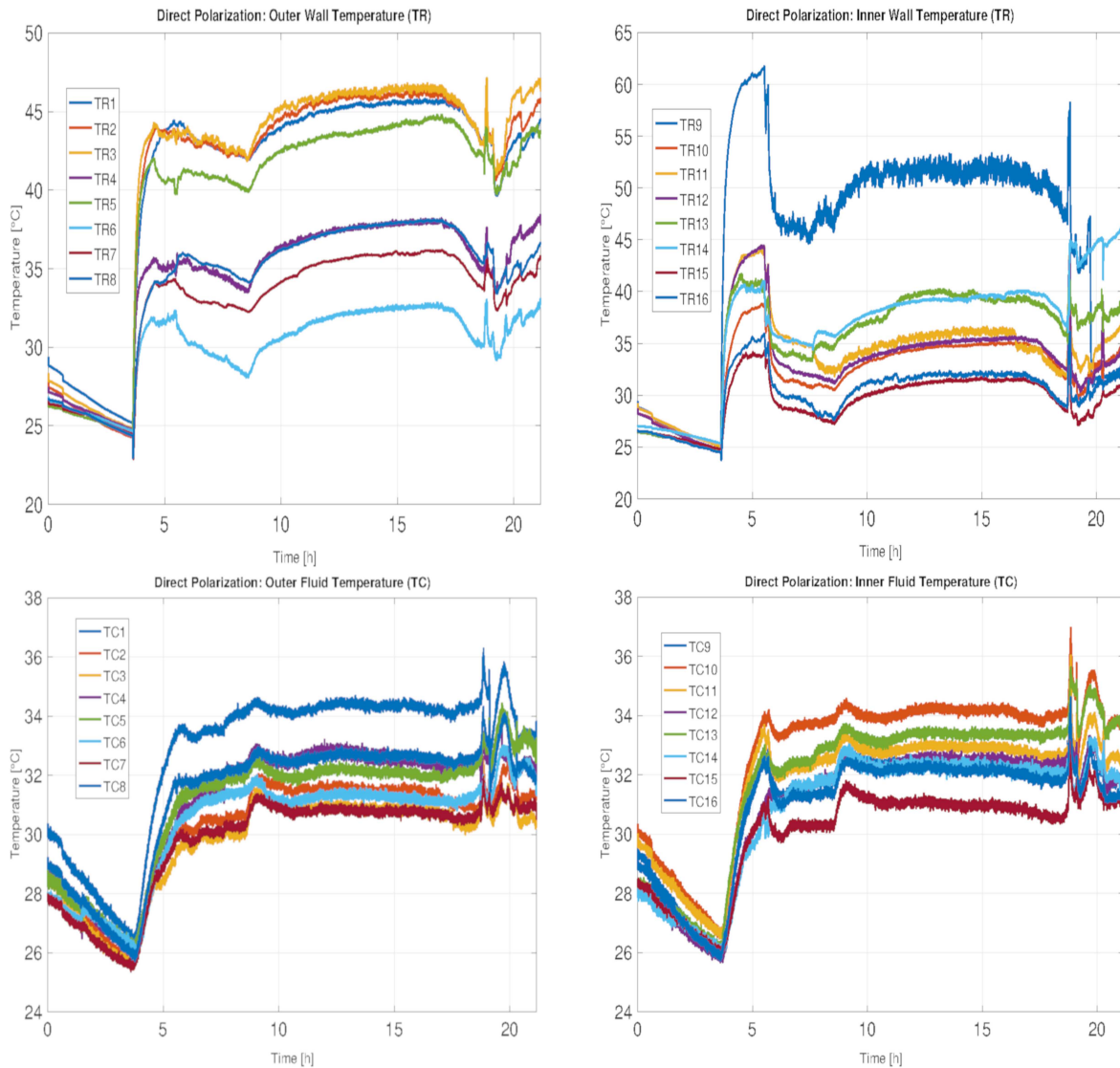


FIGURE 2.33: An alternative view of the Front Panel window, where the data collecting in real time are substituted by graphs made with Matlab. The graphs show an entire acquisition lasted around 21 h: the upper ones refer to thermistors (TR), while the bottom ones to thermocouples (TC).

When the data collection must be ended, it is sufficient to press the stop button and the program stops to run; to see all the data collected it is possible to open the created file, located in the file path defined in the Write to Measurement File block. Then the data can be plotted with other program for data manipulations, like Origin or Matlab, and perform successive data analysis.

In next Chapter 3, detailed mathematical analysis will be presented, as well as some comments about the collected data.

Chapter 3

Data Analysis

3.1 General Overview

In this Chapter 3, the data collected from the measurements devices will be plotted in graphs, which will be consequently commented.

Firstly, the thermal response of the CERES system will be presented, mentioning two combinations of polarization the Peltier modules; then, the impedance behaviour of the system is discussed.

3.2 Thermal response of CERES system

The CERES paradigm is based on the creation of thermal gradients inside the FF, able to generate magnetic cycling forces, and consequently a reusable electric energy.

To do so, the CERES reactor is brought far from thermal equilibrium by Peltier modules, in particular one side is heated while the other one is cooled. In addition, since the Peltier modules are already installed, it is possible to heat/cool the same wall by simply reversing the polarity of the Peltier module: in this way, the same side of this device will change its thermal behaviour.

The two possible cases are described in the following Paragraphs 3.2.1 and 3.2.2.

3.2.1 Peltier modules directly polarized

In this first configuration, the Peltier modules are directly polarized. This means that the side that usually produces heat, is used as designed. The hot side of the Peltier modules is in direct contact with the outer wall of the reactor, while the cool side faces the inner wall. Furthermore, in order to increase the removal of heat coming from the central part of the torus, a small fan (as the ones used in computers) is placed above the central part of the structure.

At this point, all the electronics can be switched on, providing current to the Peltier modules, which starts to cooling/heating, meanwhile the temperature sensors begin to send data, thanks to the LabView™ software.

In order to have a complete behaviour of the temperature within the CERES reactor, the system is left on from the afternoon until the morning, reaching nearly one day of continuous measurements. The average of the curves of the four graphs previously shown in Figure 2.33, will be reported here in Figure 3.1.

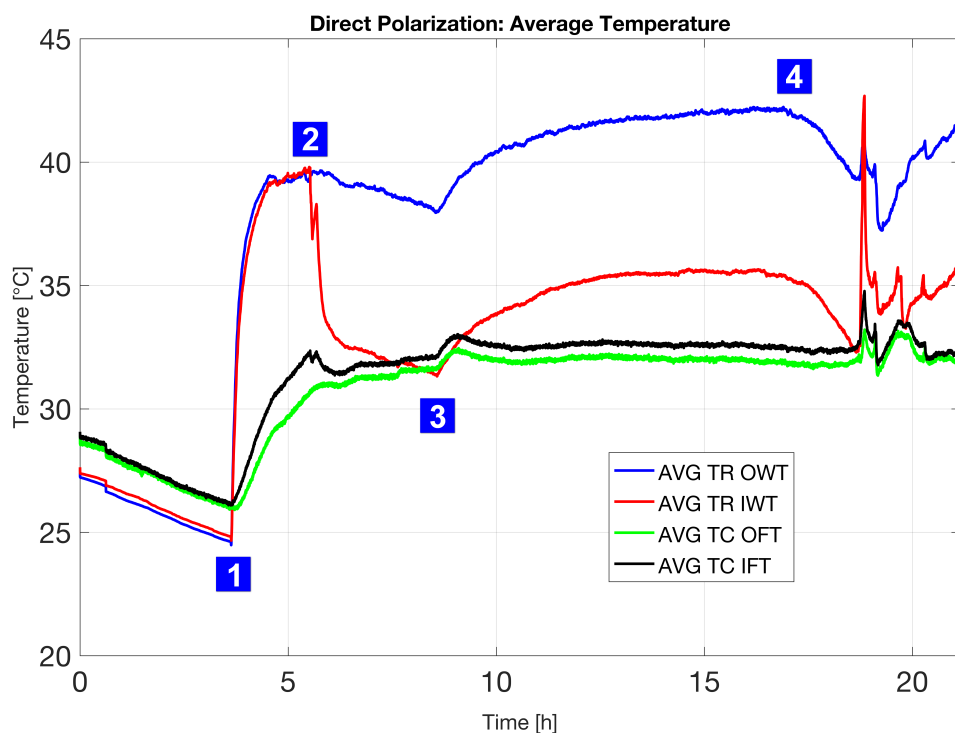


FIGURE 3.1: The average temperatures reached by the walls and the FF in DP (Direct Polarization). In blue the average of thermistors 1-8 (Outer Wall Temperatures, or OWT), in red the average of thermistors 9-16 (Inner Wall Temperatures, or IWT), in green the average of thermocouples 1-8 (Outer Fluid Temperatures, or OFT), and in black the average of thermocouples 9-16 (Inner Fluid Temperatures, or IFT). The first decrease on the left corresponds to the switching on of the medium fan (Peltier modules are turn-off), while the consequent rapid increase (point 1) is related to the switching on of the Peltier stations; the red curve reduces its temperature after the placement of the small fan at the center of the reactor, obtaining in this way a better thermal gradient on the walls (point 2). Point 3 represents the automatic switch off of the air conditioning, while point 4 indicates the air conditioning switched on. Other increases/reductions are mainly due to fluctuations in the automatic air conditioning of the lab.

Here it is possible to notice that the temperature within the FF remains constant from one wall to the other (and practically for the entire measurement), due to the fact that the fluid try to reach a thermal equilibrium by means of convective flux and cyclic motion. However, a thermal gradient appears just at the walls (red and blue curves), as can be expected since the Peltier stations have opposite thermal faces in contact with the reactor. These facts can be better visualized when plotting the behaviours of thermal gradients, simply doing the differences among the blue and red curves (for thermistors), and between black and green curves (for thermocouples). The results are reported in Figure 3.2.

In Figure 3.2(a) is well noticeable the presence of relevant thermal gradient among the inner and outer walls of the reactor, which moreover remains constant for almost the entire night: this is an important result for the first CERES prototype, remarking the feasibility to produce a thermal gradient by means of Peltier modules. On the contrary, Figure 3.2(b) shows that the thermal gradient inside the FF is rather small since the molecules are moving to compensate it (the spikes should not be considered, since in that moments the system was not in thermal equilibrium).

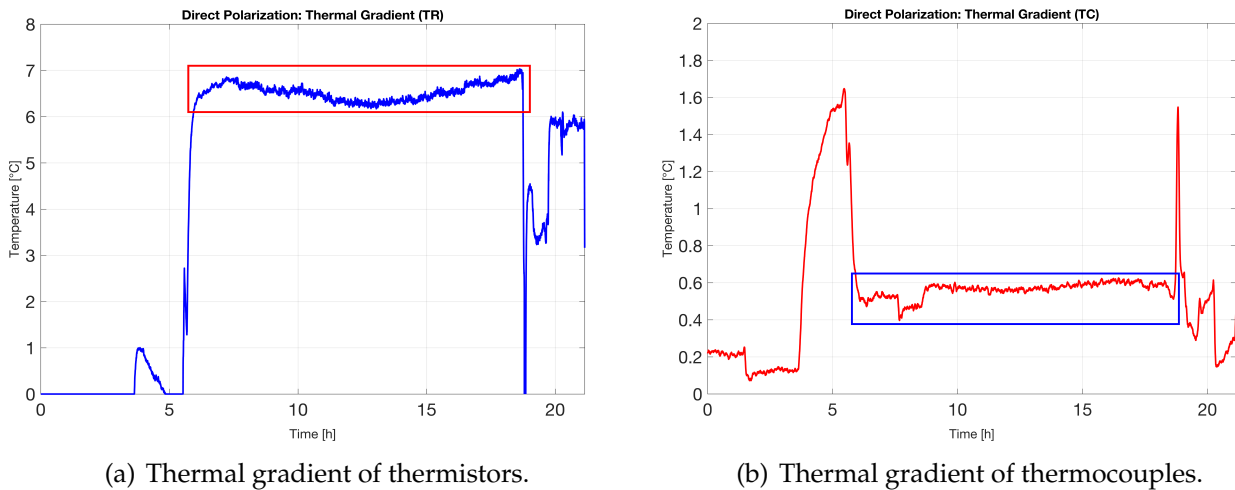


FIGURE 3.2: Thermal gradients with Peltier modules used in DP.

3.2.2 Peltier modules inversely polarized

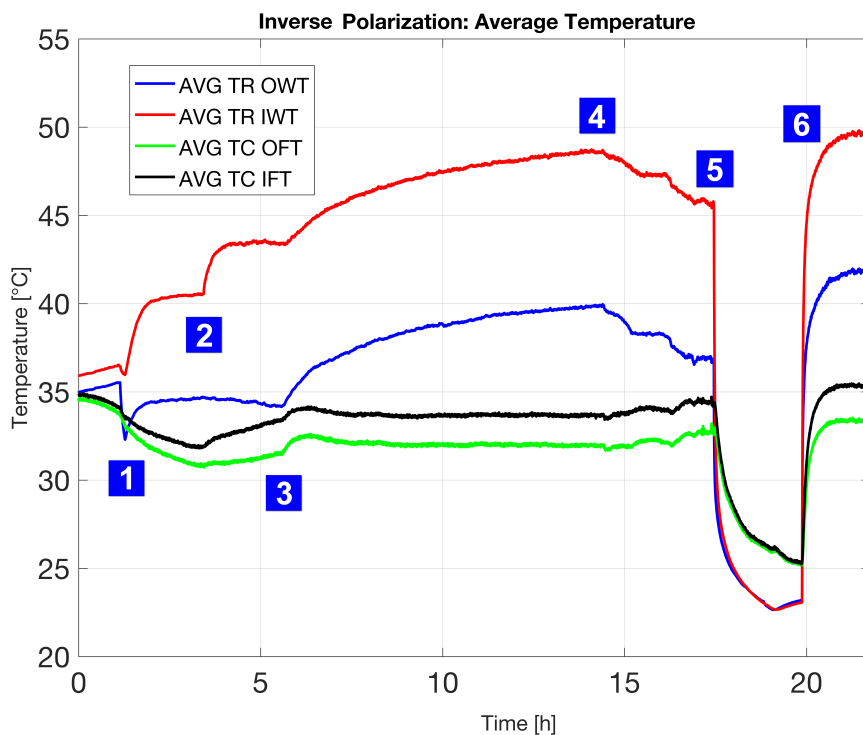


FIGURE 3.3: The average temperatures reached by the walls and the FF in IP (Inverse Polarization). In blue the average of thermistors 1-8 (Outer Wall Temperatures, or OWT), in red the average of thermistors 9-16 (Inner Wall Temperatures, or IWT), in green the average of thermocouples 1-8 (Outer Fluid Temperatures, or OFT), and in black the average of thermocouples 9-16 (Inner Fluid Temperatures, or IFT). Point 1 represents the power on of Peltier modules, point 2 indicates the removal of the small fan from the center of the reactor, point 3 and 4 correspond to the turnin on and off (respectively) of the automatic air conditioning of the lab. The big decrease (point 5) corresponds to the switching off of the electronics (except the temperature sensors), while the subsequent rapid increase (point 6) relates to the new switching on of the Peltier modules (Figure 3.5 better represents this transient).

In this second configuration, the Peltier modules are inversely polarized. This means that the side that usually produces heat, now acts as the cool side. To reverse the polarization it is sufficient to connect the positive electrical terminal of a Peltier module with GND, and the negative one to the place previously occupied by the positive terminal. After this operations is done for each heating element, a measurement analogous to the one performed in DP, but in this case the small fan is removed. The average curves obtained are depicted in Figure 3.3. Reversing the polarization of the Peltier modules, the average temperatures are a bit higher than in the previous case. This increment can be due to the fact that now the external side of the outer Peltier stations is hot, with the possibility to dissipate better the heat to environment, while before the heat was confined in the inner ring of the reactor, even considering the presence of the small fan. However, the rise in temperature can be observed also from the behaviour of thermal gradients in IP configuration, as reported in Figures 3.4(a) and 3.4(b). Here the temperature difference among the walls is raised of more than $1\text{ }^{\circ}\text{C}$ with respect to previous polarization, remaining mostly comprised between $7\text{ }^{\circ}\text{C}$ and $8\text{ }^{\circ}\text{C}$; even the thermal gradient within the FF shows a similar increase.

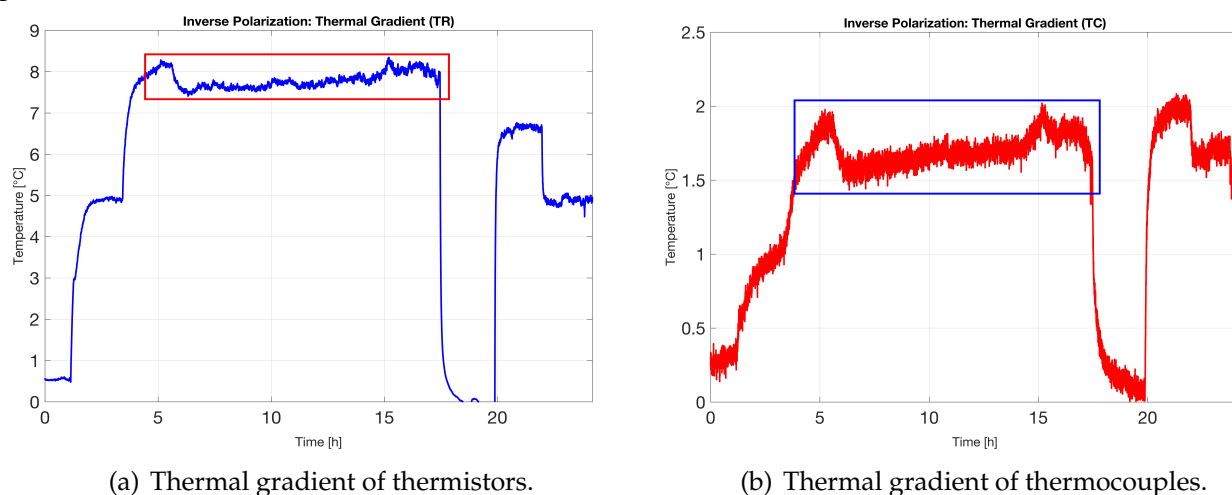


FIGURE 3.4: Thermal gradients with Peltier modules used in IP.

To conclude this Section 3.2, a complete view of the transient responses of the temperature sensors used, from high to low temperature (and viceversa), is reported in Figure 3.5. Here it is possible to see a very fast response of the sensors system, especially for what concerns the heating behaviour.

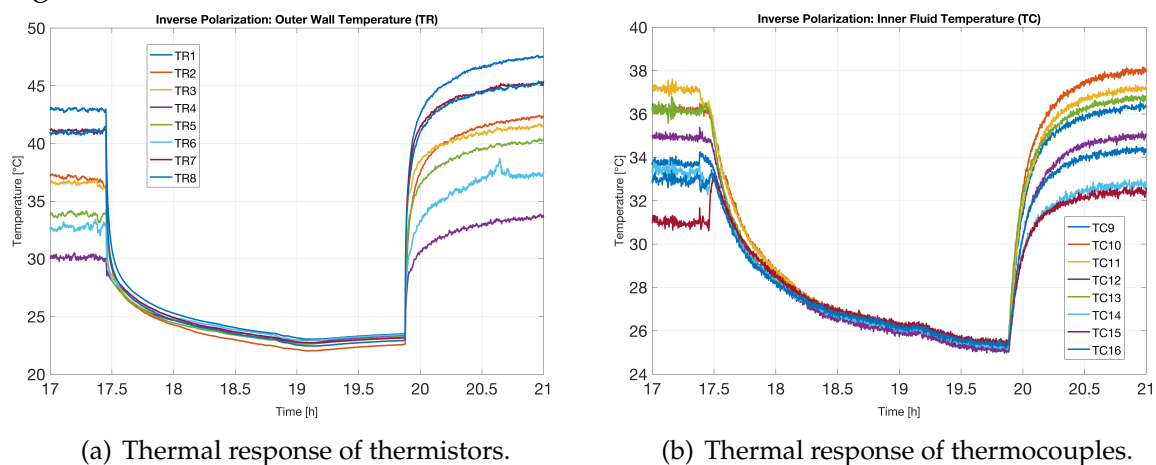


FIGURE 3.5: Thermal transients with Peltier modules used in IP.

3.3 Impedance behaviour of CERES system

An impedance analysis is a very relevant characterization of many (electrical) systems, and given the amount of electronics devices used, including a lot of cables and the coils for the extraction measurement, studying the impedance behaviour of the CERES system is considered fundamental.

Recalling Figure 2.20, it is important to underline that around the CERES reactor there are four wrapped coils, where two of the three poloidal coils are connected in series to perform impedance measurements, and the remaining two (one poloidal and one toroidal) are used to induce a magnetostatic field.

In particular, two main electrical parameters will be analysed in details, and they are the inductance (Paragraph 3.3.1) and the resistance of the system (Paragraph 3.3.2); for what concern the capacitance of the system, the latter is not detailed since, from the impedance measurements, it resulted to be negligible.

3.3.1 Inductive behaviour

The idea to take into consideration the possible existence of a huge (and maybe parasitic) inductance, comes from the presence of a large number of coils and magnetic material. These objects could give origin to phenomena related to magnetic fields and currents, like the mutual induction, in addition to the induced EMF.

According to this, the inductive behaviour of the CERES reactor is studied by measuring the inductance at terminals of the two poloidal coils connected in series. Moreover, during the measurement, some FF is added to the reactor, in order to see some variations in the inductance of the system, as the FF acts as the iron core of a real discrete inductor. This experiment is performed by inserting in the reactor (already filled with water for the first experiments, instead of oleic solvent) 1 mL of FF EFH1: the result is depicted in Figure 3.6.

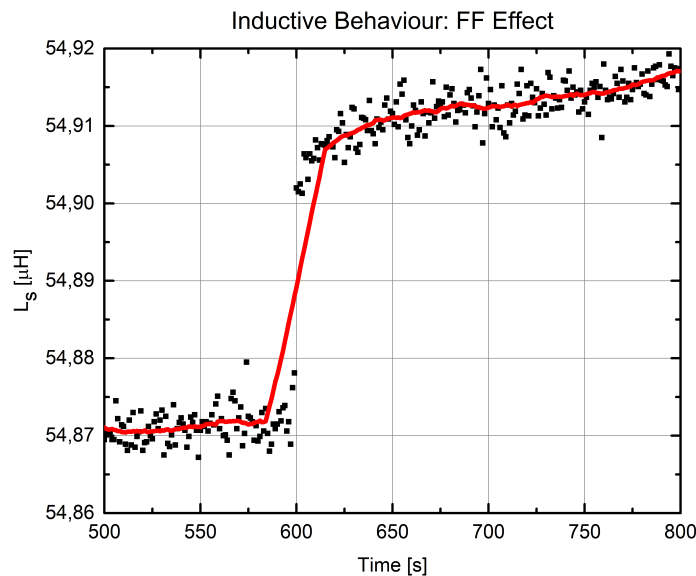


FIGURE 3.6: The result of the addition of 1 mL of FF EFH1 inside the reactor filled with 1 L of water. It is clearly evident the presence of a straight step of the inductance measured on the extraction coil, moving from 54.87 μH to 54.91 μH , and saturating around 54.92 μH . Moreover, the experiment is done by giving a push to the added FF, by turning on the poloidal (inversely polarized with 1.85 A and 5 V) and toroidal (directly polarized with 3.10 A and 5 V) coils with a DC current generator.

This result is very interesting, and strongly confirms the correctness of CERES, especially considering that only 1 mL of FF was added to the reactor paradigm.

Then, a full inductance characterization, lasted around 14 h, is performed: in particular, it is possible to observe the variations occurring in early stages (Figure 3.7), when Peltier modules are switched on, and after ≈ 100 s also the DC current generator is activated.

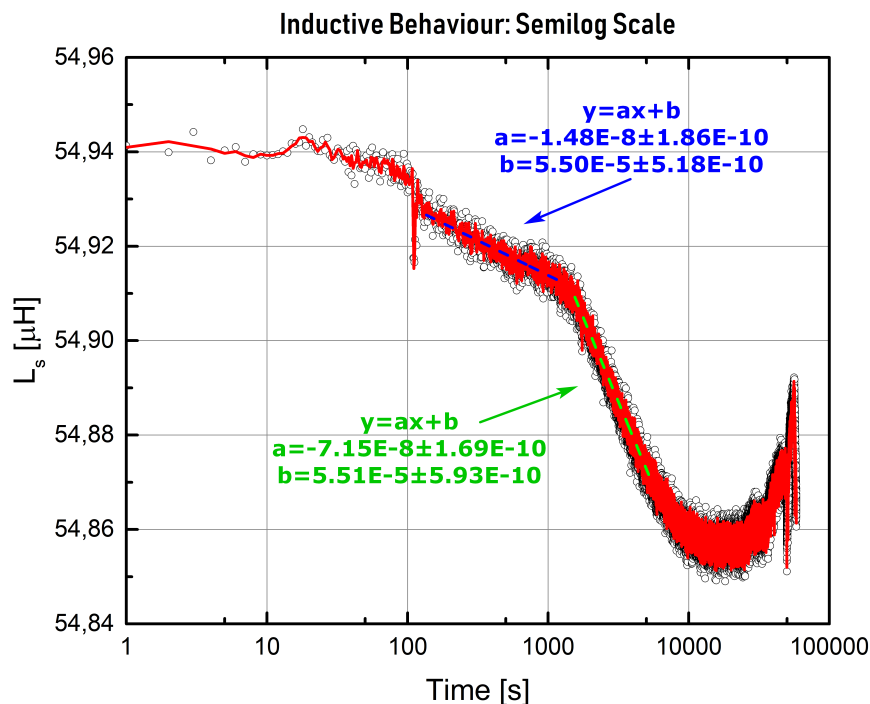


FIGURE 3.7: The behaviour of the inductance in semilogarithmic scale. With this graphical representation, the initial stages can be observed in a better way: in particular, it can be noticed that signal is very stable around 54.94 μH , than it becomes a little bit perturbed by the power on of Peltier stations, successively the DC current starts flowing into the coils and the series inductance makes a decrease following a precise straight line, which slope drastically changes around 1000 s; in the end the signal stabilizes near 54.86 μH . The reasons of the first line must be searched in the Seebeck effect, influencing the electrical parameters of cables when their extremities are subjected to a thermal gradient, but becoming negligible in short time due to the high thermal conductivity of wires. The explanation of the second slope could more difficult, but a possible solution is to consider this variation as a result of the heating FF inside the reactor, which probably requires a certain time to initiate its cyclic motion. When the motion is completely set up, the inductance remains constant at the new value.

After the analysis of the inductance at early stages, the study moves towards the long term. In Figure 3.8 it is possible to find out how the inductance stays constant (when all other parameters remain the same) along all the measurement period, increasing a little bit before stopping the collection of data, maybe due to the switching on of the automatic air conditioning of the lab in the early morning.

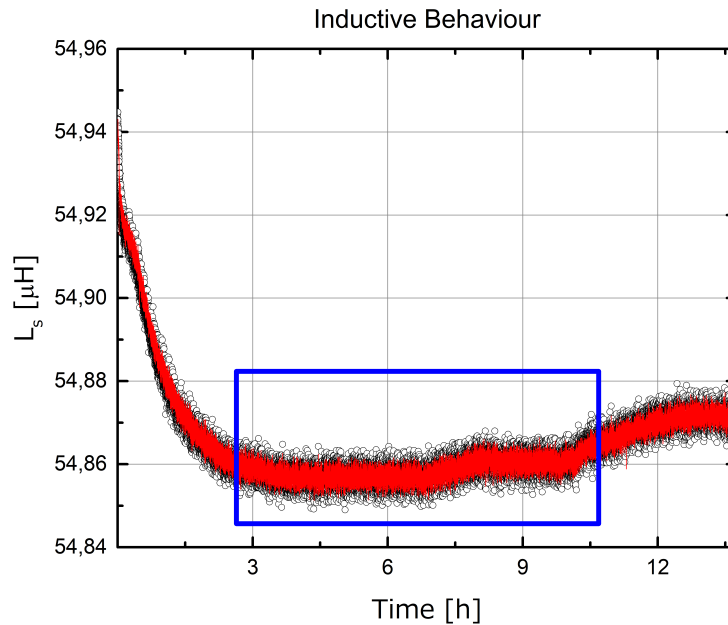


FIGURE 3.8: The inductive behaviour after one night of continuous acquisition; it is possible to see that the inductance stays almost constant, except in the initial and final stages.

3.3.2 Resistive behaviour

Once the inductive behaviour is completed, it is the time to do the same for the resistive behaviour of the CERES system. Here the experiments performed are partially similar to the one just done, but new effects appear.

Firstly, the system resistance is studied in the initial stages: in Figure 3.9 is depicted the startup of the system, and the consequent effects on the resistance.

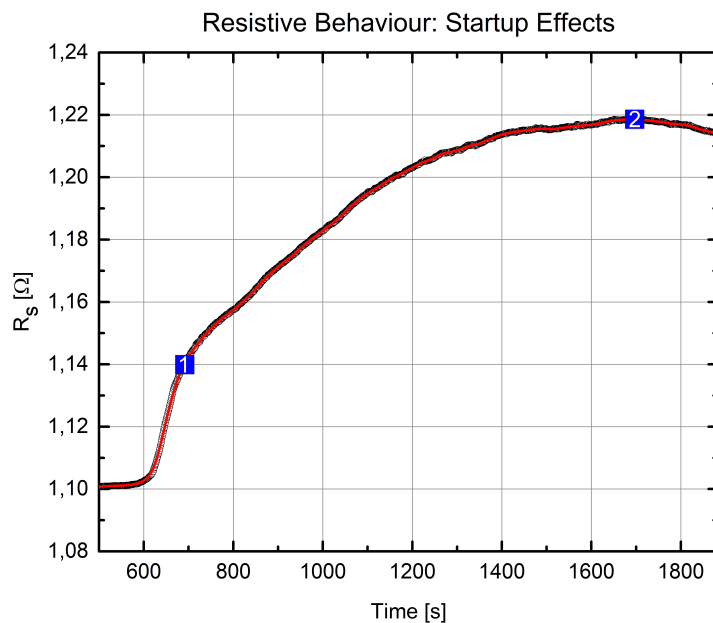


FIGURE 3.9: The measure starts when the signal stabilizes, reaching a resistance value of 1.10Ω ; then, the Peltier modules and the DC generator are powered up, so that the resistance rapidly increases (600 s, point 1), and 100 s after, the resistance variation attenuates, saturating near 1.22Ω (point 2).

The fast rise of the resistance should be explained by means of Seebeck effect, since in the early stages all the cables have not the same temperature along their entire length; however the further increase in the resistance (even if at a smaller rate) could be explained by considering that the FF starts its cyclic motion with a certain delay with respect to the power up of the system. Moreover, this happens with the same delay seen in the case of the inductive behaviour.

Another interesting experiment is done always in early part of another measurement: in this case, after the resistance is stabilized, the CERES system is shaken with hands in order to see if a push in the direction of FF motion can increase the resistance, and the effect of an opposite movement. Figure 3.10 shows these attempts.

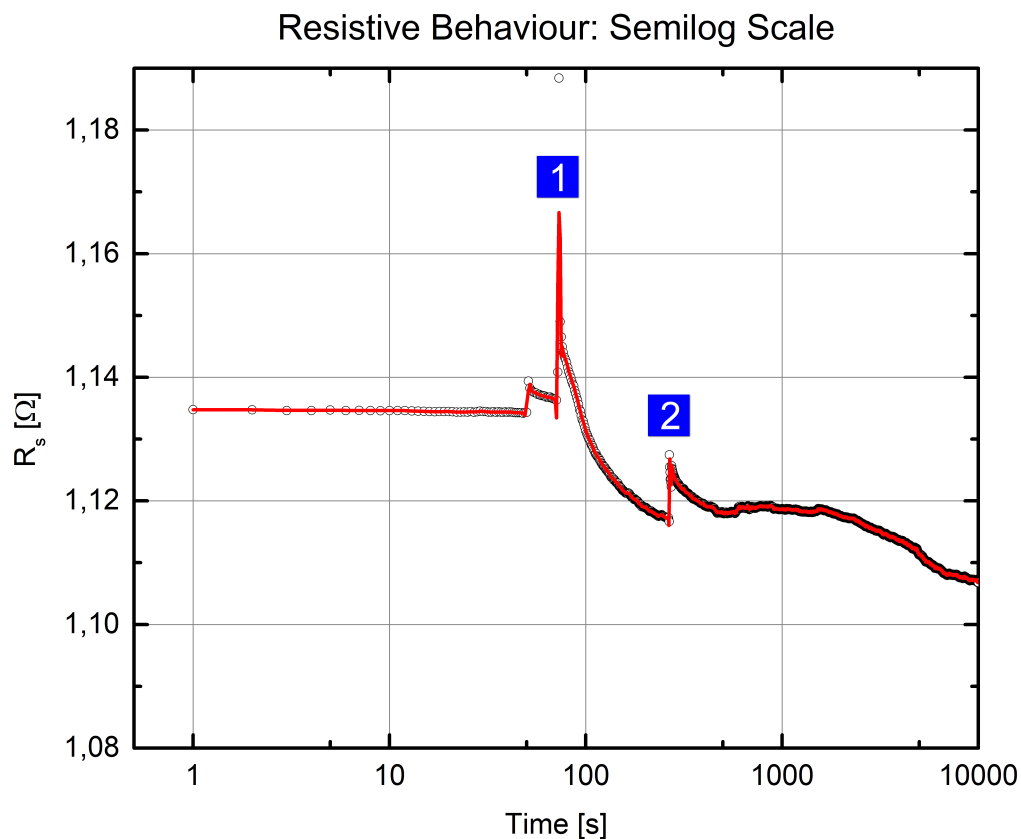


FIGURE 3.10: Resistive behaviour of CERES system when perturbed by hand agitation. Two spikes are present, and are related to the agitation introduced with the hands. The higher one corresponds to an agitation with the same direction of the FF motion, the smaller one relates to an agitation opposite with respect to motion.

When the system is shaken provoking an additional push in the same direction of the motion, the increase in resistance is quite considerable, but when the push tries to oppose to the motion, the resistance increase is lower. However, the reason of this will be detailed in next Paragraph 3.4.

At this point, the long term analysis of the resistive behaviour is reported in Figure 3.11, where the resistance remains almost constant.

In another experiment, the resistance behaves in a way quite particular, after 1 mL of FF is added to the reactor chamber (Figure 3.12).

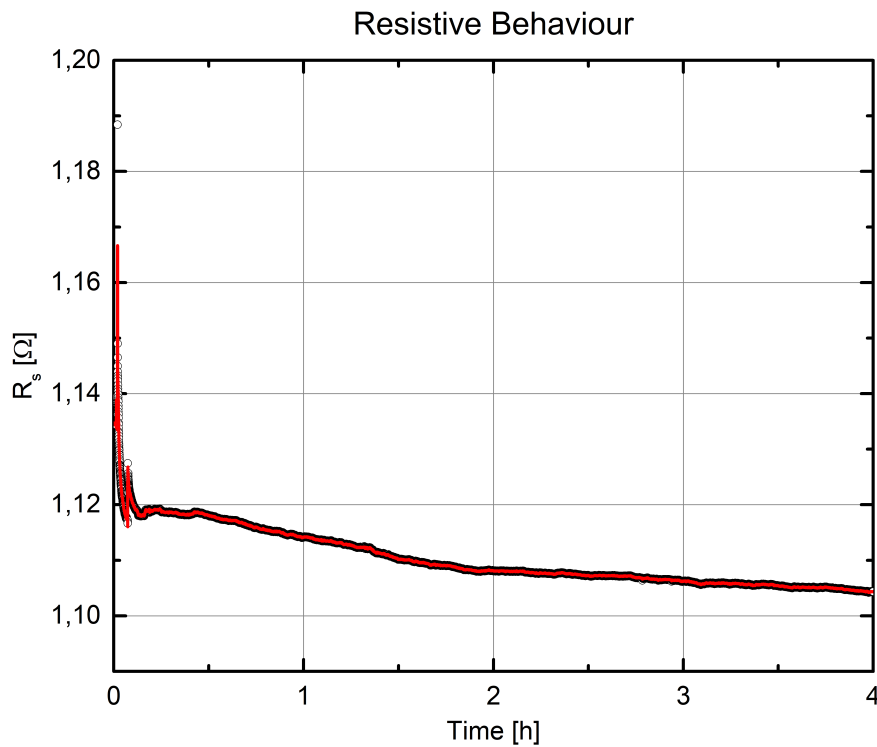


FIGURE 3.11: Resistive behaviour of CERES system for a long measurement time. After the initial variations (due to hands agitation), the resistance shows a very slow transient towards 1.105 Ω .

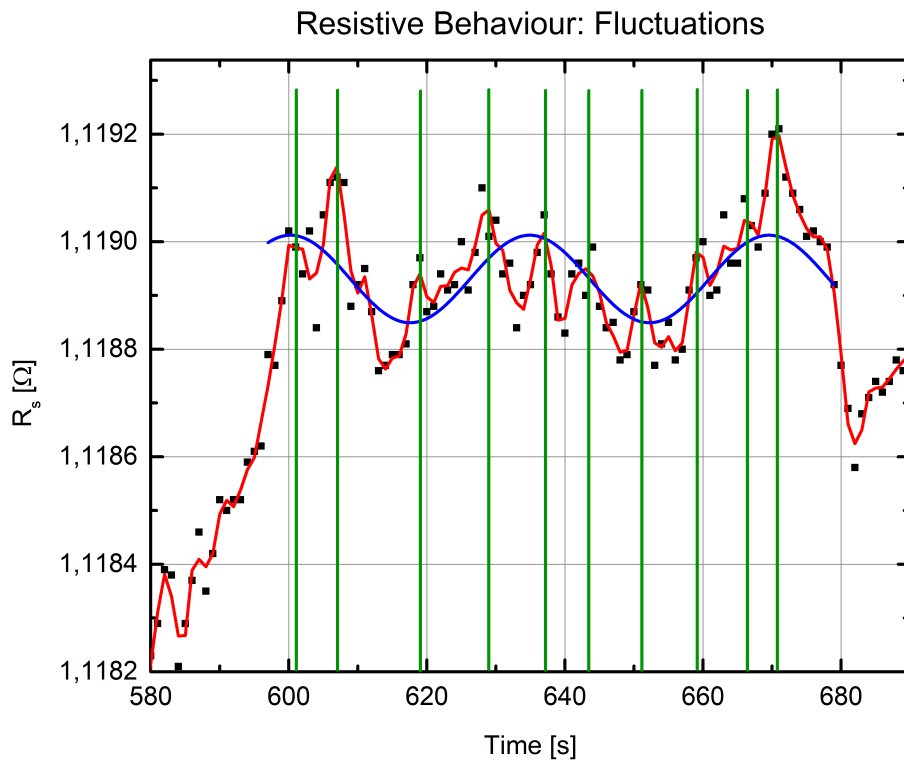


FIGURE 3.12: Resistive behaviour of CERES system with particular fluctuations after the addition of 1 mL of FF, around 600 s. The red curve is obtained by smoothing the scatter plot with Savitzky–Golay method, while the blue curve show a sinusoidal fitting. The green lines shown instead the temporal distance among successive peaks.

It is interesting to see the presence of these peaks, that, even if they could be random in time, they are not, since the green lines show a periodicity of ≈ 8 s. This information is useful to determine the velocity of FF inside the reactor: given the distance between two adjacent windings (≈ 10 cm), the resulting FF speed is roughly 1.25 cm/s. In the case of harmonic signal, the detection of higher order harmonics should be expected. In fact, the sinusoidal fitting presents a period of nearly 35 s, which is quite close to the fundamental period multiplied by 4. Looking better, it is also possible to notice another strange function: the inverse chirp (Figure 3.13).

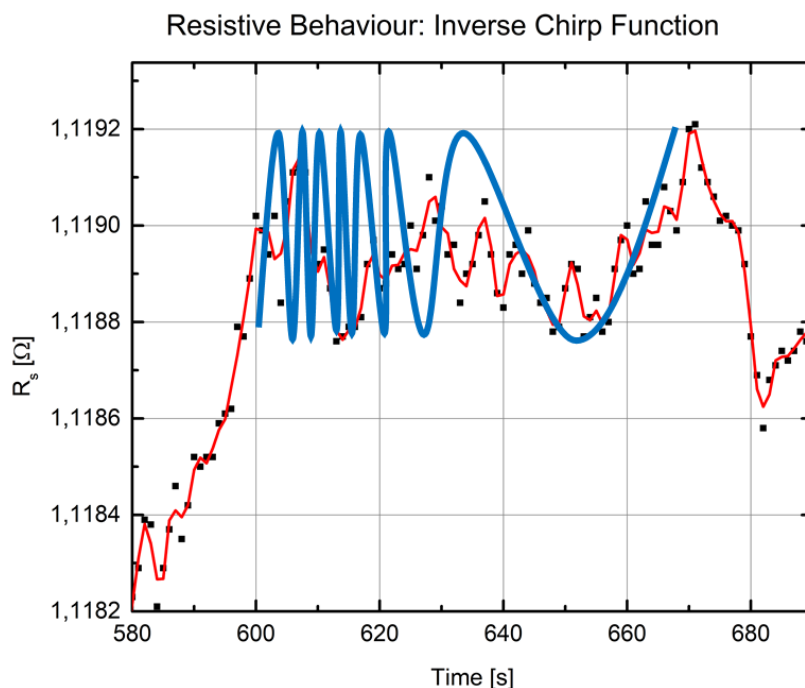


FIGURE 3.13: Graphical representation of an inverse chirp function drawn over the fluctuations appeared in the CERES system, after the addition of 1 mL of FF.

The presence of these harmonic and chirp functions could be the first signal indicating the presence of possible waves within the FF contained inside the reactor. This could be, perhaps, the first experimental detection of the waves theorized by the CERES paradigm, and a strong confirmation of the paradigm itself.

In any case, the next Section 3.4 will detail the current behaviour of the CERES system.

3.4 Current behaviour of CERES system

The behaviour of the current inside the CERES reactor is quite interesting, because of the response of the system to the external environment.

First of all, here will be discussed the concept of fluid inertia mentioned in the previous Paragraph 3.3.2. In particular, the greater/lower increase in resistance (corresponding to a greater/lower voltage induced on the coils) can be explained considering that the FF within the reactor has a certain inertia. When the fluid is put in motion with a certain current, it keeps a certain time to reverse the motion by simply polarizing the coils in the opposite direction. In fact, changing the currents exiting from the DC generator, it is possible to test four combinations since the connected coils are two (poloidal and toroidal). If the first combination has both cables directly polarized, and, changing (after a certain time) to another one combination will have no effect on the intensity of the current induced by EMF extracted from the CERES system.

Another effect comes out when few mL of FF are added to the reactor containing water, and is clearly visible in Figure 3.14.

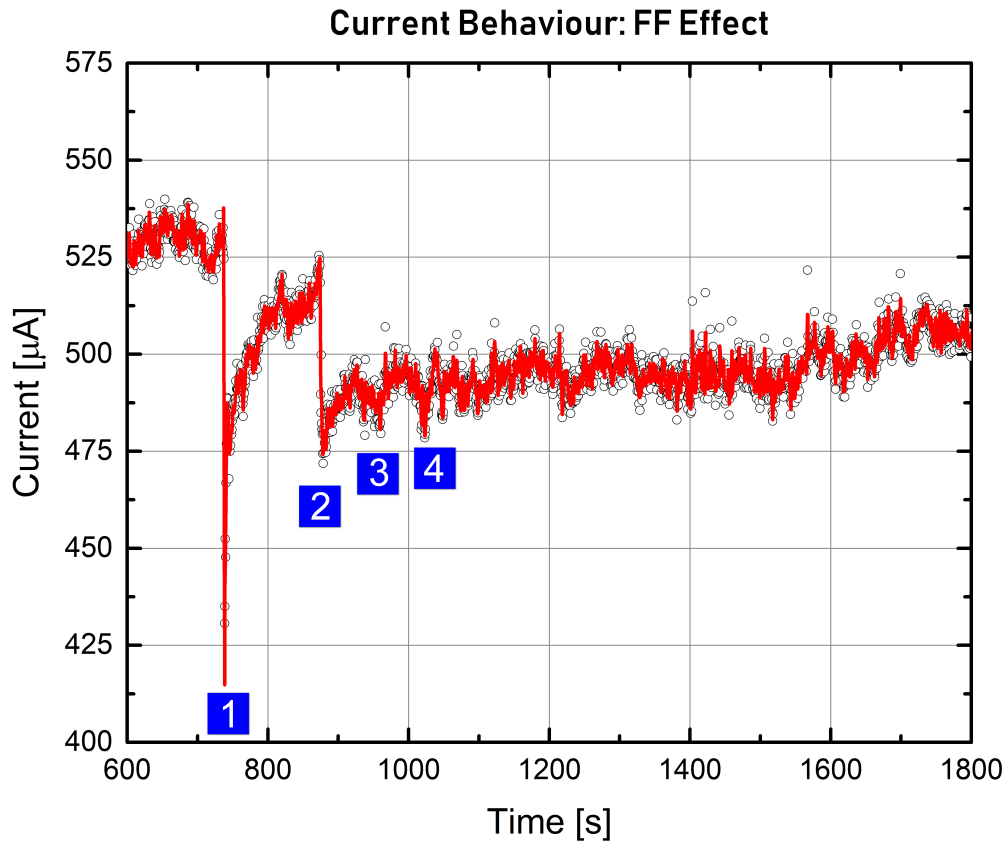


FIGURE 3.14: Behaviour of the current, after the addition of 2 mL of FF inside the reactor. The current drop is well visible at 750 s (point 1) and 890 s (point 2). Looking better, it is possible to distinguish two minor current drops at point 3 and point 4.

In this case, 2 mL of FF are inserted in the reactor, and their effect appears in as a significant drop of the current, passing from 525 μA to 415 μA , with a gap of nearly 100 μA . Then, there are other current drops, which become closer in time and smaller in intensity: also in this situation it is possible to talk about the presence of fluctuations.

However, after the drops, the current stays constant at the new value, lower than the first one for the presence of more FF inside the CERES system.

In the last Chapter 4, a brief computation of the parameters involved and the efficiency of this first prototype will be presented, together with final considerations about the actual status of the system and future optimizations.

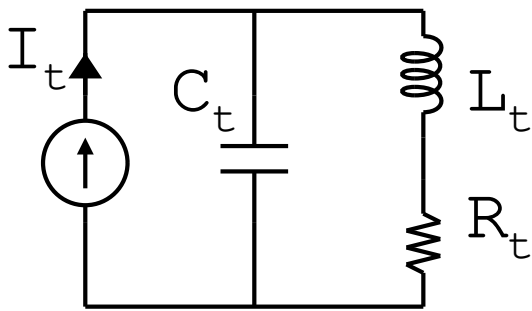
Chapter 4

Conclusions

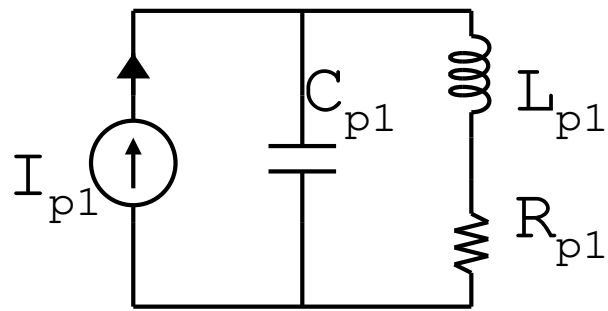
4.1 Efficiency of CERES system

The efficiency of the CERES system can be computed by considering the parameters involved in the electrical characterizations done in Chapter 3.

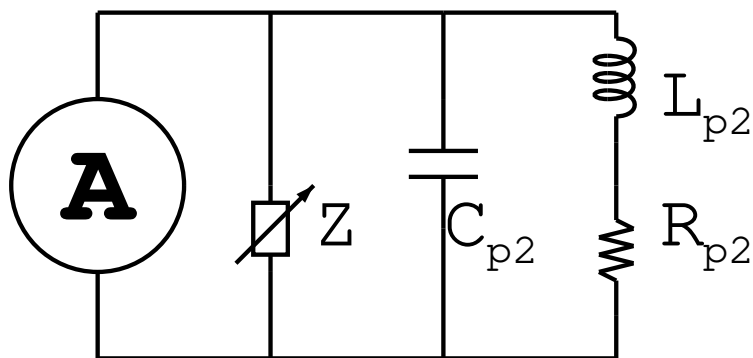
First of all it is important to report the equivalent circuits corresponding to the different coils wrapped around the CERES reactor, which are depicted in Figure 4.1.



(a) Equivalent circuit of the toroidal coil.



(b) Equivalent circuit of the first poloidal coil.



(c) Equivalent circuit of second toroidal coil; here the coil drawn is the series of the two poloidal coils, while A represents an amperometer, which is not always connected to the rest of the circuit, and Z indicates the impedancemeter.

FIGURE 4.1: Equivalent circuits of the coils wrapped around the CERES system.

It should be immediately said that the capacitors present in these circuits can be treated as negligible, and are drawn for completeness; Figures 4.1(a) and 4.1(b) denote the two coils

connected to the DC current generator.

The impedance Z_{p2} of circuit in Figure 4.1(c) can be measured by means of an impedancemeter, and correspond to:

$$Z_{p2} = R_{p2} + jX_{p2} \quad (4.1)$$

where R_{p2} is the resistance, and X_{p2} is the reactance (imaginary part) of the inductance L_{p2} ; the relationship between inductance and reactance is:

$$X_{p2} = j\omega L_{p2} \quad (4.2)$$

Other way to compute the inductance of a solenoid can be found in books of elementary Physics, and using Equation 4.3 it is possible to get:

$$L_{p2} = \frac{\mu AN^2}{\ell} \quad (4.3)$$

For the system considered, $A = 120.7 \text{ cm}^2$, $\ell = 294 \text{ cm}$, $N = 80$ and $\mu = \mu_r \cdot \mu_0$ depends on the magnetic permeability of the material contained within the coils. In case of simple air, $\mu_r = 1$, and the result will be $L = 33 \text{ }\mu\text{H}$. If the reactor would be completely filled with magnetite NPs, whose magnetic permeability corresponds to $\mu_r = 3.64$, the resulting inductance will be $L = 118 \text{ }\mu\text{H}$. It is important to remember that μ_r comes from the magnetic susceptibility χ_m :

$$\mu_r = 1 + \chi_m \quad (4.4)$$

where in case of FF EFH1 $\chi_m = 2.64$. Because of the inductance measured in Chapter 3 is around $54 \text{ }\mu\text{H}$ (when 1 mL of FF is added to the reactor), the magnetic permeability of CERES system must be $\mu_{r,eff} = 1.00666$. As a consequence, the addition of a so small amount of FF corresponds to an increase of μ_r of 1 %, with respect to the case of empty reactor.

In other words, the addition of 1 mL FF EFH1 at a concentration of 7.9 % in volume, or $80 \text{ }\mu\text{L}$ of Fe_3O_4 , relates to an increase of the mass inside the reactor of 10 ppm, which is able to produce a consequent gain of the relative magnetic permeability of 1 %. Moving towards the electrical part, it could be useful to consider the variation of the AC resistance reported in Figure 3.9, among points 1 and 2. Since $R_{AC1} = 1.14006 \text{ }\Omega$ and $R_{AC2} = 1.21889 \text{ }\Omega$, the resulting change in resistance is approximatively $\Delta R_{AC} = R_{AC1} - R_{AC2} = 0.07883 \text{ }\Omega$.

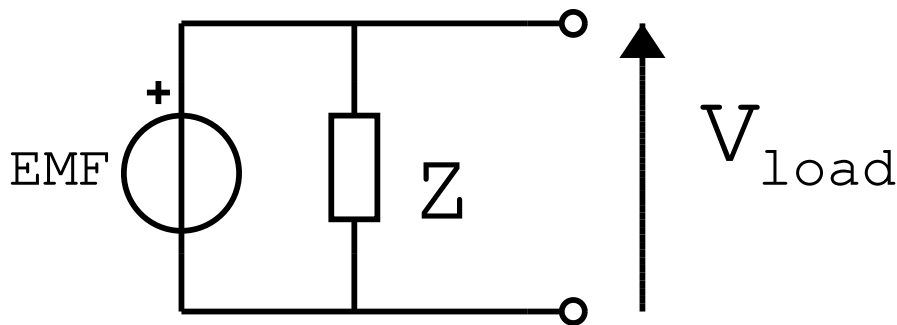


FIGURE 4.2: Graphical representation of a simple circuit involving an impedance Z containing DC and AC resistance terms, and EMF as voltage source.

Taking into account the circuit of Figure 4.2, it is possible to derive the following relationships:

$$I_{meas}^{\Re} = \frac{V_{load}^{\Re}}{R_{AC}} \quad \Rightarrow \quad R_{AC} = \frac{V_{meas}^{\Re} + \text{EMF}}{I_{meas}^{\Re}} \quad (4.5)$$

where I_{meas}^{\Re} represents the real part of the measured current, V_{meas}^{\Re} is otherwise the real voltage measured, V_{load}^{\Re} is the real part of the voltage drop across the load, while R_{AC} corresponds to the AC value of the resistance measured. Solving with respect to EMF:

$$\text{EMF} = R_{AC} \cdot I_{meas}^{\Re} - V_{meas}^{\Re} \quad (4.6)$$

The current and the voltage provided by the impedancemeter are 0.5 mA and 0.4 mV, respectively. In this case:

$$\text{EMF}_1 = 20.9445 \text{ mV} \quad \text{EMF}_2 = 17.0030 \text{ mV} \quad \Rightarrow \quad \Delta\text{EMF} = 3.94150 \text{ mV} \quad (4.7)$$

According to this, and given $R_{DC} = 1.229150 \Omega$, the electrical power at the output will be:

$$P_{el}^{out} = \frac{(\text{EMF})^2}{R_{DC}} = 12.6392 \mu\text{W} \quad (4.8)$$

considering that the overall amount of FF inside the reactor is around 10 mL, which correspond to 800 μL of magnetite NPs, or to 4.14 g (their specific gravity is 5.175). Moreover, since the greatest thermal gradient between the walls is nearly 8°C between 37°C and 45°C , the relative Carnot efficiency η (of a thermal machine) is:

$$\eta = 1 - \frac{T_{low}}{T_{high}} = 1 - \frac{310.15 \text{ K}}{318.15 \text{ K}} = 0.02515 \approx 2.5\% \quad (4.9)$$

In order to compute a reasonable input thermal power (at Peltier module level), a thermal gradient of 50 K produced by the Peltier modules is considered, corresponding to a COP (Coefficient Of Performance, [78]) when operating with 0.5 A and 2.3 V. The heat absorbed by the cold side will be:

$$Q_C = \frac{COP}{P_{el}} = 0.4348 \text{ J} \quad (4.10)$$

Since the CERES reactor is covered with 32 Peltier modules, the overall thermal energy provided is equal to 13.91 J. However, the thermal conductivity of PLA is nearly 10 W/mK, the input thermal power P_{th}^{in} on the CERES reactor corresponds to 1.4 W.

4.2 Future optimizations of CERES 1.0 system

The most relevant parameters of CERES 1.0 are summed in Table 4.1:

CERES Properties	Value
P_{th}^{in}	1.4 W
P_{el}^{out}	12.64 μW or 15.8 mW/L
FF V_{eff}	800 μL
FF m_{eff}	4.14 g

TABLE 4.1: Main properties of CERES 1.0.

A lot of things can be done without changing the prototype, and in particular are focused on the largest possible increase of the output electrical power.

A short list of successive improvements is the following one:

- Increase m_{eff} of 100 times, in order to reach an output power of ≈ 1 mW.
- Saturate better the NP magnetization, resulting in a factor 10 to 100, reaching an output power in range 10 mW to 100 mW.
- Use NPs with very high saturation, to reach a value of P_{el}^{out} comprised between 50 mW and 500 mW.
- Provide a larger input electrical power, in order to increase Q_C . Then, if $COP = 5$, Q_C enlarges of 10 times, and the output power achieves 0.5 W to 1 W. Considering that, in this case, the thermal input power arises up to 140 W, and given the upper efficiency limit equal to η previously found, the maximum electrical power that could be extracted from CERES 1.0 is 3.25 W.

4.3 Future optimizations of CERES 2.0 system

The prototype CERES 2.0 will probably introduce some relevant changes in the geometry, in particular the gap between the walls could be reduced, and the walls curved, as reported in Figure 4.3. This should help the FF to sense the thermal gradient coming from the Peltier stations.

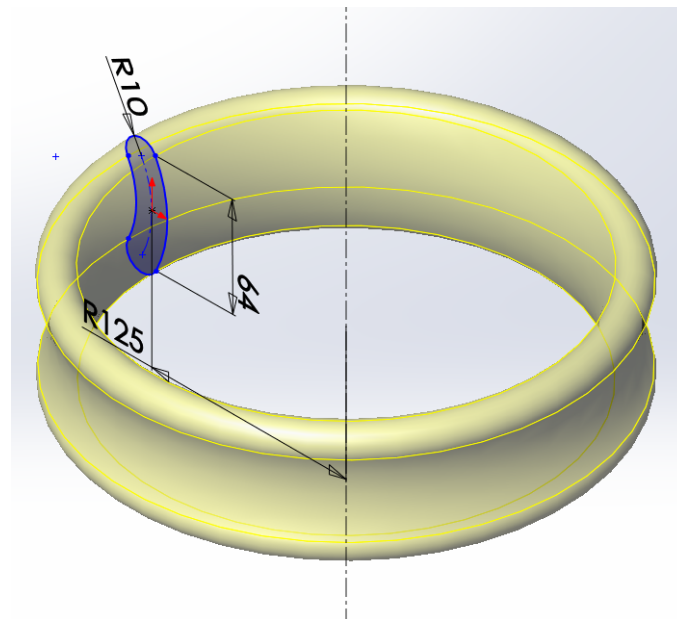


FIGURE 4.3: Graphical rendering of a futuristic new geometry of CERES reactor.

Then, the Peltier modules could be coupled to thermal dissipators.

Moreover, an upgrade on the thermal control should be necessary, as well the integration of the electronics inside an IC (Integrated Circuit).

For what concerns the temperature sensors, they could be installed in other ways, to simplify the mounting process.

Appendix A

Insights about physical background

A.1 Energy harvesting from FFs

Figure A.1a shows that the height has practically zero influence on V_{out} for given magnetic field and input acceleration. The reason of this behaviour lays in the fact that the largest waves (and deformations) occur at the surface, so the dipoles close to liquid surface are the most critical ones for the harvesting process; in particular the number of magnetic dipoles is mainly defined by the cross-section of the tank and by the percentage of dipoles per unit volume of the fluid. It is important to notice that peaks on the left side of Figure A.1a are related to f_{11} (symmetric mode), and the two other small peaks on the right are the ones of f_{12} (asymmetric mode).

Figure A.1b investigates the dependence of the magnetic field on the output voltage. The field can be easily changed by distantiating the bottom magnet from the tank (always along the vertical direction). In that a clear dependence is visible: if the magnetic induction at liquid surface reduces, becoming negative, the frequency peaks shift towards left (lower frequency values), because the effective acceleration g^* is overall decreased. This is very appreciable when the frequency must be adjusted and tuned for getting an optimal configuration. This explanation can be more useful if analysing also Figure A.2: here it is noticeable the influence of the coupling intensity between the field and the magnetic dipoles of the the fluid on the harvester's output voltage. Three cases appear:

- **a)** The magnetic field is positive along the whole fluid column, so all the dipoles are aligned in the same direction parallel with the external applied field. If external excitations are present, all dipoles are rotated in the same direction as the propagating wave: the variation of the magnetic flux related to the rotation of each dipole adds up and the harvester's output voltage enlarges.
- **b)** The magnetic field changes direction inside the FF, and some dipoles experience a weaker magnetic field: these dipoles orient in a randomly way and the resulting net magnetic flux is small compared to **a**).
- **c)** When the lower magnet is placed at a even larger distance from the bottom side of the container, the magnetic field at liquid surface becomes so large (in absolute value) that the surface experience a very intense coupling with the external field. In this case very large accelerations are needed to create sufficient rotations with respect to the field, and as a consequence the influence on the output voltage is even worse.

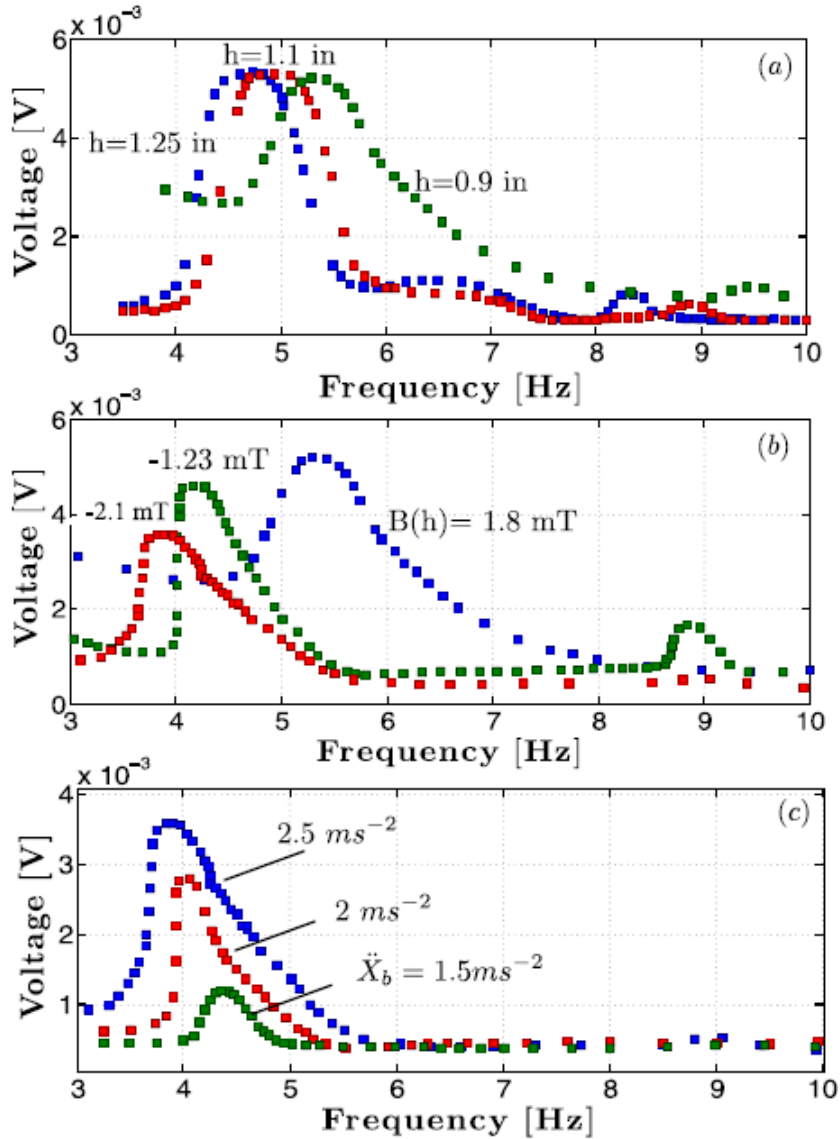


FIGURE A.1: Output voltage vs frequency responses curves for different parameters [43]: **a)** Varying the height, a constant output electric potential is got in all cases, but the peaks shift little towards left; 1 in=2.54 cm. **b)** Reducing the magnetic field, different output electric potentials are obtained and peaks shift towards left, for negative field. **c)** Increasing the mechanical excitation (acceleration), an greater output voltage is reached, with peaks little shifting towards left.

Figure A.3a shows the relevant increase of the harvester's output voltage when the FF surface is enlarged, confirming the important role played by the number of dipoles close to the surface on the output voltage value.

Figure A.3b confirms that power around $1 \mu\text{W}$ can be reached if an optimal resistance close to 35Ω is chosen (the container should stay horizontal).

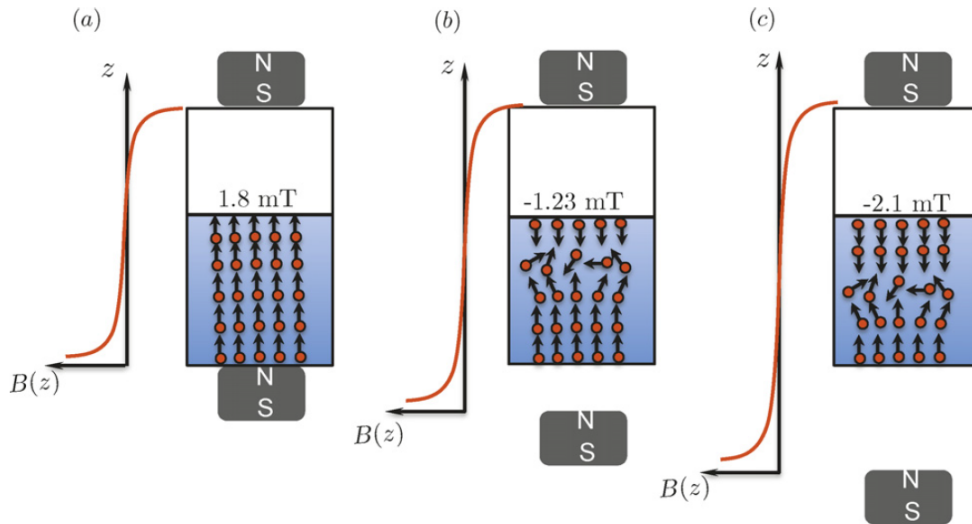


FIGURE A.2: Distribution of the magnetic induction inside the liquid, according to three different situations **a)**, **b)** and **c)** [43].

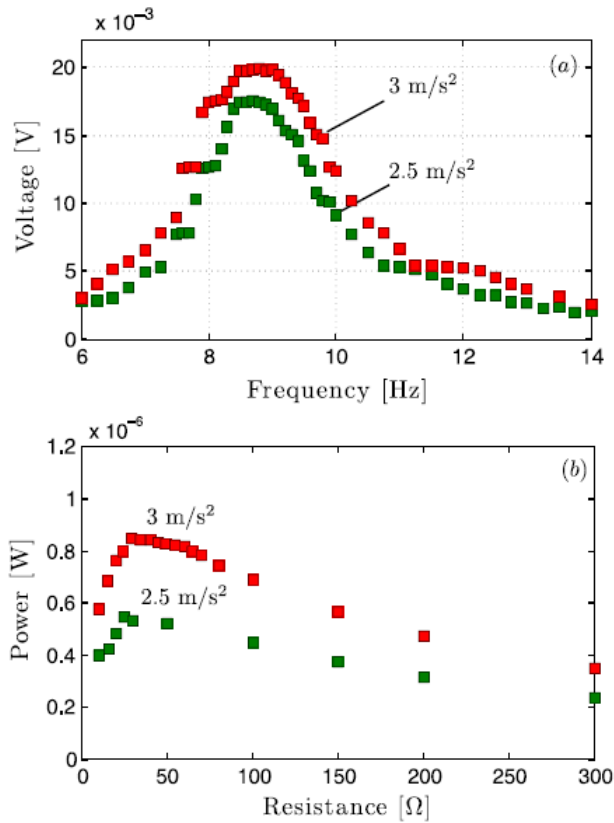


FIGURE A.3: Considering a frequency of 9 Hz and two acceleration levels (2.5 m/s^2 and 3 m/s^2), the following graphs are obtained [43]: **a)** Output voltage vs frequency showing the higher values of V_{out} obtained when the container is tilted by 90° , to increase the liquid surface. **b)** Power vs resistance curves indicate the presence of power peaks corresponding to an optimal resistance value.

A.2 Molecular Dynamics

MD simulations are a particular type of computer simulations, that can be performed in order to obtain the results shown in Figure 1.19, Paragraph 1.4.3.

A subset of identical particles, included between two impenetrable walls able to act also as heat source/sink, is considered for a MD simulation example. As a consequence, the overall number of particles in the simulation is $N = N_s + N_w$, where N_s indicates the number of solution particles (the first one is the optically trapped particle), while N_w corresponds to the number of particles forming the wall. The coordinates $(\vec{q}_1, \vec{q}_2, \dots, \vec{q}_N, \vec{p}_1, \vec{p}_2, \dots, \vec{p}_N)$ of the phase space are computed from the following equations:

$$\dot{\vec{q}}_i = \frac{\vec{p}_i}{m} \quad for 1 \leq i \leq N \quad (\text{A.1})$$

$$\dot{\vec{p}}_i = \sum_{j \neq i}^N \vec{F}_{ij} + \delta_{1i} \vec{F}_{opt} \quad for 1 \leq i \leq N_s \quad (\text{A.2})$$

$$\dot{\vec{p}}_i = \sum_{j \neq i}^N \vec{F}_{ij} + \vec{F}_i^w - \alpha \vec{p}_i \quad for (N_s + 1) \leq i \leq N_w \quad (\text{A.3})$$

The interaction force among the particles i and j separated by a distance q is given by Equation A.4a, while the potential energy is expressed by Equation A.4b:

$$\vec{F}_{ij} = -\frac{d\phi(q)}{d\vec{q}} \quad (\text{A.4a})$$

$$\phi(q) = \begin{cases} 4(q^{-12} - q^{-6}) & \text{if } q \leq 2^{1/6} \\ 0 & \text{otherwise} \end{cases} \quad (\text{A.4b})$$

$$\vec{F}_{opt} = -k[\vec{q}_1 - \vec{q}_0(t)] \quad \text{for the first particle} \quad (\text{A.4c})$$

$$\vec{F}_i^w = -k^w[\vec{q}_i - \vec{q}_i^{crystal}] \quad \text{for the wall particles} \quad (\text{A.4d})$$

$$\vec{q}_0(t) = \begin{cases} \vec{q}_0(0) + \vec{v}_{opt}t & \text{if } 0 < t < t_{max} \\ \vec{q}_0(0) & \text{otherwise} \end{cases} \quad (\text{A.4e})$$

\vec{F}_{opt} (Equation A.4c) acts only on the first particle trapped at position $\vec{q}_0(t)$ during the simulated trajectory or it is stationary for all other times. Equation A.4d is a force restoring the wall particles to their crystalline initial condition, while α is the Nosé-Hoover thermostat multiplier. Once a single trajectory has been completely recorded, the system is set again to its initial conditions and ready for a successive simulation. The simulation results are reported in Figure A.4.

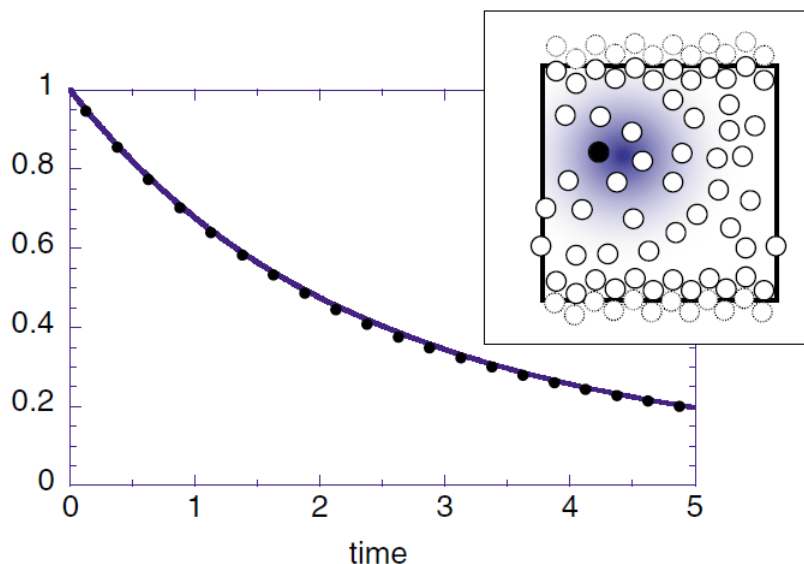


FIGURE A.4: The MD simulations for 343 500 simulated trajectories show a behaviour very similar to the experimental one depicted in Figure 1.19. The figure on the top-right represents the trapped particle (black filled circle) enclosed between the impenetrable walls, while the coloured shaded zone denotes the optical trap [50].

Figure A.5 indicates that the probability ratio of finding a trajectory with a produced entropy A over the probability of finding a trajectory with the same absolute value of entropy variation (consumed or generated).

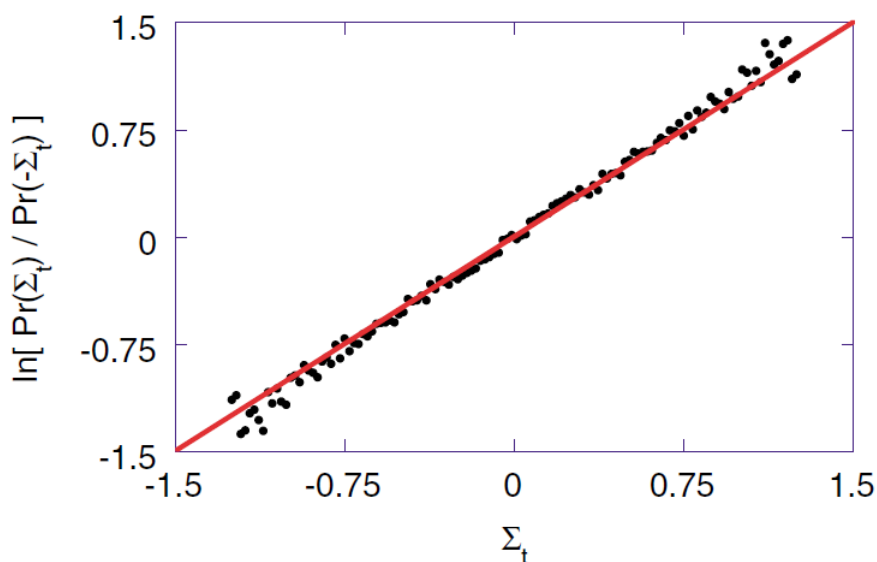


FIGURE A.5: Behaviour of the ratio between entropy producing trajectories over entropy consuming trajectories from a set of 310 000 MD simulations [50].

A.3 Derivation of exergy

Considering a system A , as the one reported in Figure A.6, surrounded by its environment A_0 ; each of them is characterized by some intensive properties (temperature T , pressure p and chemical potential μ), and by some extensive properties (internal potential energy U , volume V , entropy S and moles of chemical elements).

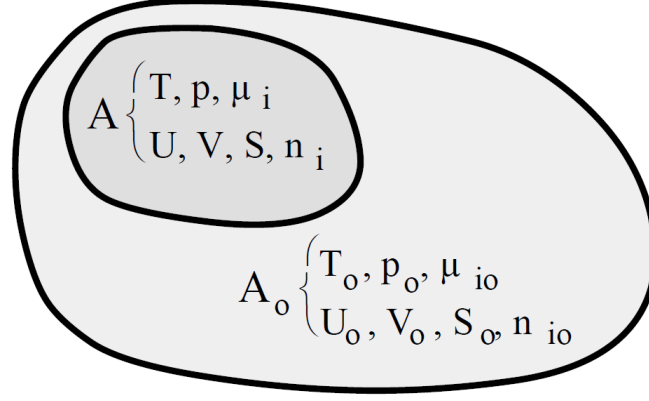


FIGURE A.6: The system A , with its parameters and the surrounding environments A_0 with its properties [53].

The parameters of the system A are assumed to be much greater than the ones of the environment, and can be summed into Equation A.5:

$$\begin{cases} U \ll U_0 \\ V \ll V_0 \\ n_i \ll n_{i0} \end{cases} \quad (\text{A.5})$$

Moreover, the comprehensive system $A+A_0$ is supposed to be isolated (no exchange of both energy and matter is possible with the outside), except for the work W extracted from A ; Equation A.6 underlines better this concept:

$$\begin{cases} dU + dU_0 + dW = 0 \\ dV + dV_0 = 0 \\ dn_i + dn_{i0} = 0 \end{cases} \quad (\text{A.6})$$

Since system A is smaller than A_0 , the intensive parameters of A_0 are not subjected to variations (Equation A.7):

$$\begin{cases} dT_0 = 0 \\ dp_0 = 0 \\ d\mu_{i0} = 0 \end{cases} \quad (\text{A.7})$$

The corresponding differential entropy of A_0 is:

$$\begin{aligned} dS_0 &= \frac{1}{T_0} \left(dU_0 + p_0 dV_0 - \sum_i \mu_{i0} dn_{i0} \right) \\ &= -\frac{1}{T_0} \left(dU + p_0 dV - \sum_i \mu_{i0} dn_i \right) - \frac{dW}{T_0} \end{aligned} \quad (\text{A.8})$$

while the differential and total entropies of the complete system are:

$$\begin{aligned} dS_{tot} &= dS + dS_0 = -\frac{1}{T_0} \left(dU + p_0 dV - T_0 dS - \sum_i \mu_{i0} dn_i \right) - \frac{dW}{T_0} \\ &= -\frac{1}{T_0} (dE + dW) \end{aligned} \quad (\text{A.9a})$$

$$\Delta S_{tot} = -\frac{1}{T_0} (-E + W) \geq 0 \quad (\text{A.9b})$$

where the exergy E has just been introduced, and defined in Equation A.10:

$$\begin{aligned} E &= U + p_0 V - T_0 S - \sum_i \mu_{i0} n_i \\ &= S(T - T_0) - V(p - p_0) + \sum_i n_i (\mu_i - \mu_{i0}) \end{aligned} \quad (\text{A.10})$$

The second equality in the latter equation is possible by means of the following relation:

$$U = TS - pV - \sum_i \mu_i n_i \quad (\text{A.11})$$

Furthermore Equation A.10 shows that exergy disappears when equilibrium is reached ($T=T_0$, $p=p_0$, $\mu_i=\mu_{i0}$). Other possibility is that the equilibrium is reached without work ($dW=0$), so the entropy variation will be:

$$S_{tot}^{eq} - S_{tot} = -\frac{(-E)}{T_0} \quad (\text{A.12})$$

which leads to the following relationship, where Σ indicates the negentropy:

$$E = T_0(S_{tot}^{eq} - S_{tot}) = T_0 \Sigma \geq 0 \quad (\text{A.13})$$

From the last term of Equation A.13 can be noticed that exergy can be simply represented as the product among temperature of the environment and negentropy. Then, if the entropy variation is ΔS_{tot} and the extracted work is W , Equation A.9b could be rewritten into Equation A.14:

$$W = E - T_0 \Delta S_{tot} \quad (\text{A.14})$$

Since entropy change is zero only in reversible transformation, otherwise $\Delta S_{tot} > 0$, from Equation A.14 the following important relation is derived:

$$W \leq E \quad (\text{A.15})$$

The latter relationship (Equation A.15) is fundamental because it states that the maximum amount of work that can be extracted from a system A , while approaching towards the equilibrium, coincides with the exergy E . Subtracting the equilibrium conditions from Equation A.10, it is possible to derive the following Equation A.16, which is quite useful for practical determination of exergy:

$$E = U - U_{eq} + p_0(V - V_{eq}) - T_0(S - S_{eq}) - \sum_i \mu_{i0}(n_i - n_{i,eq}) \quad (\text{A.16})$$

Moreover, in Table A.1 are reported some useful expressions for special cases of the exergy, according to different thermodynamic conditions.

Case	$\Delta E = \Delta X$	Definition of X	Usually named
$\Delta n_i = 0$	$\Delta E = \Delta G_0$	$G_0 = U + p_0V - T_0S$	--
$\Delta n_i = 0, \Delta V = 0$	$\Delta E = \Delta F_0$	$F_0 = U - T_0S$	--
$\Delta n_i = 0, \Delta S = 0$	$\Delta E = \Delta H_0$	$H_0 = U + p_0V$	--
$\Delta n_i = 0, p = p_0, T = T_0$	$\Delta E = \Delta G$	$G = U + pV - TS$	Gibbs Free Energy
$\Delta n_i = 0, \Delta V = 0, T = T_0$	$\Delta E = \Delta F$	$F = U - TS$	Helmholtz's Free Energy
$\Delta n_i = 0, \Delta S = 0, p = p_0$	$\Delta E = \Delta H$	$H = U + pV$	Enthalpy

TABLE A.1: Here are reported several forms of exergy according to different kinds of thermodynamic potentials [53].

After that, an additional case is to consider a further system included into A_0 and which contains system A, as depicted in Figure A.7:

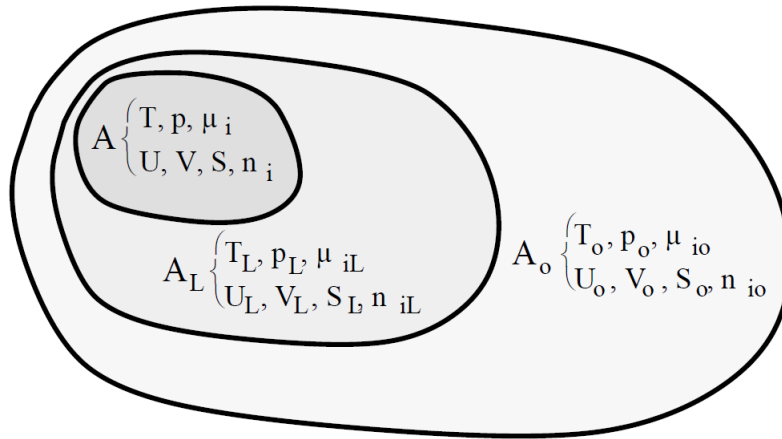


FIGURE A.7: The system A, with its parameters placed inside a local system A_L , enclosed at its time within the surrounding environments A_0 with its properties [53].

Also here, a local exergy E_L can be defined as follows in Equation A.17 and related to the global exergy by Equation A.10:

$$E_L = U + p_L V - T_L S - \sum_i \mu_{iL} n_i \quad (\text{A.17})$$

Moreover, Equation A.18 describes the deviation of the local environment from the global one:

$$E_{L0} = E - E_L = (T_L - T_0)S - (p_L - p_0)V + \sum_i (\mu_{iL} - \mu_{i0})n_i \quad (\text{A.18})$$

It is remarkable that E_{L0} is not a function of the exergy, and also to consider that the concept itself of exergy has an important role in the information theory (Paragraph 1.5.4).

Bibliography

- [1] <https://bit.ly/2x14k8W>,
- [2] <https://bit.ly/1iY8OnJ>,
- [3] <https://bit.ly/2FL5X04>,
- [4] A. Elson, R. Tidball, and A. Hampson, "Waste heat to power market assessment", 2015.
- [5] <http://www.usetute.com.au/hallhero.html>,
- [6] A Chiolerio and M. B. Quadrelli, "Smart fluid systems: The advent of autonomous liquid robotics", *Advanced Science*, vol. 4, no. 7, 2017.
- [7] E. Warburg, "Magnetische untersuchungen", *Annalen der Physik*, vol. 249, no. 5, pp. 141–164, 1881.
- [8] Tegus, <https://iop.fnwi.uva.nl/cmp//klaasse/Tegus/Tegusthesis.pdf>,
- [9] H. B. Callen, *Thermodynamics and an Introduction to Thermostatistics*. Wiley, 1985.
- [10] <https://bit.ly/2wZxpRM>,
- [11] M. Thorade and A. Saadat, "Partial derivatives of thermodynamic state properties for dynamic simulation", *Environmental earth sciences*, vol. 70, no. 8, pp. 3497–3503, 2013.
- [12] P. W. Bridgman, "A complete collection of thermodynamic formulas", *Physical Review*, vol. 3, no. 4, p. 273, 1914.
- [13] <https://at.virginia.edu/2Qhm3Sg>,
- [14] R. P. Lungu, "Thermodynamics of electric and magnetic systems", in *Trends in Electromagnetism - From Fundamentals to Applications*, InTech, 2012.
- [15] <https://bit.ly/2O25mse>,
- [16] <https://bit.ly/2wVol0H>,
- [17] V. Nizhankovskii, V. Mokerov, B. Medvedev, and Y. V. Shaldin, "An investigation of the effect of a magnetic field on the chemical potential of electrons in bismuth and in a GaAs-Al_xGa_{1-x}As heterojunction", *Zh. Eksp. Teor. Fiz*, vol. 90, pp. 1326–1335, 1986.
- [18] <https://bit.ly/2MXfq9A>,
- [19] <http://www.damtp.cam.ac.uk/user/tong/statphys/five.pdf>,
- [20] N. D. M. N. W. Ashcroft, *Solid State Physics*. Elsevier, 2014.
- [21] <https://bit.ly/2wULGPZ>,
- [22] M Mekata, H Kuriyama, Y Ajiro, S Mitsuda, and H Yoshizawa, "First-order magnetic transition in Co₂", *Journal of Magnetism and Magnetic Materials*, vol. 104, pp. 859–860, 1992.
- [23] P Khuntia and A. Mahajan, "Magnetic susceptibility and heat capacity of a novel anti-ferromagnet: Lni₂p₃o₁₀ and the effect of doping", *Journal of Physics: Condensed Matter*, vol. 22, no. 29, p. 296 002, 2010.
- [24] V Tsurkan, M Mücksch, V Fritsch, J Hemberger, M Klemm, S Klimm, S Körner, H.-A. K. von Nidda, D Samusi, E.-W. Scheidt, *et al.*, "Magnetic, heat capacity, and conductivity studies of ferrimagnetic MnCr₂S₄ single crystals", *Physical Review B*, vol. 68, no. 13, p. 134 434, 2003.
- [25] M. S. Bishwas and P. Poddar, "Study of magnetic entropy and heat capacity in ferrimagnetic Fe₃Se₄ nanorods", *Journal of Physics D: Applied Physics*, vol. 49, no. 19, p. 195 003, 2016.

- [26] B Detlefs, S. Wilkins, P Javorský, E Blackburn, and G. Lander, "Multi-k magnetic structures in u sb 0.9 to 0.1 and u as 0.8 se 0.2 observed via resonant x-ray scattering at the u m 4 edge", *Physical Review B*, vol. 75, no. 17, p. 174 403, 2007.
- [27] C. L. M. Snow, "The heat capacity and thermodynamic properties of the iron oxides and their relation to the mineral core of the iron storage protein ferritin", 2010.
- [28] E. F. Westrum Jr and F. Grønvold, "Magnetite (fe_3o_4) heat capacity and thermodynamic properties from 5 to 350 k, low-temperature transition", *The Journal of Chemical Thermodynamics*, vol. 1, no. 6, pp. 543–557, 1969.
- [29] E. Verwey and P. Haayman, "Electronic conductivity and transition point of magnetite (fe_3o_4)", *Physica*, vol. 8, no. 9, pp. 979–987, 1941.
- [30] J.-H. Lee, J.-t. Jang, J.-s. Choi, S. H. Moon, S.-h. Noh, J.-w. Kim, J.-G. Kim, I.-S. Kim, K. I. Park, and J. Cheon, "Exchange-coupled magnetic nanoparticles for efficient heat induction", *Nature nanotechnology*, vol. 6, no. 7, p. 418, 2011.
- [31] R. E. Rosensweig, "Heating magnetic fluid with alternating magnetic field", *Journal of magnetism and magnetic materials*, vol. 252, pp. 370–374, 2002.
- [32] J. D. Slavin, J. M. Shull, and M. C. Begelman, "Turbulent mixing layers in the interstellar medium of galaxies", *The Astrophysical Journal*, vol. 407, pp. 83–99, 1993.
- [33] R. D. Shull, "Magnetocaloric effect of ferromagnetic particles", *IEEE transactions on magnetics*, vol. 29, no. 6, pp. 2614–2615, 1993.
- [34] G. F. Goya and M. Morales, "Field dependence of blocking temperature in magnetite nanoparticles", in *Journal of Metastable and Nanocrystalline Materials*, Trans Tech Publ, vol. 20, 2004, pp. 673–678.
- [35] <https://bit.ly/2CAAdv6b>,
- [36] R. Zheng, H. Gu, B. Xu, and X. Zhang, "The origin of the non-monotonic field dependence of the blocking temperature in magnetic nanoparticles", *Journal of Physics: Condensed Matter*, vol. 18, no. 26, p. 5905, 2006.
- [37] D. Chen, S Patel, and D. Shaw, "Effect of magnetic particle chain formation on the entropy change in superparamagnetic nanocomposite systems", *Journal of magnetism and magnetic materials*, vol. 134, no. 1, pp. 75–78, 1994.
- [38] A. Tishin, *Handbook of Magnetic Materials*. Elsevier, 1999.
- [39] R. Kaiser and R. E. Rosensweig, "Study of ferromagnetic liquid", 1969.
- [40] J. G. Monroe, E. S. Vasquez, Z. S. Aspin, J. D. Fairley, K. B. Walters, M. J. Berg, and S. M. Thompson, "Energy harvesting via ferrofluidic induction", in *Energy Harvesting and Storage: Materials, Devices, and Applications VI*, International Society for Optics and Photonics, vol. 9493, 2015, 94930G.
- [41] S. Chae, S Ju, Y Choi, S Jun, S. Park, S Lee, H. Lee, and C. Ji, "Electromagnetic vibration energy harvester using springless proof mass and ferrofluid as a lubricant", in *Journal of Physics: Conference Series*, IOP Publishing, vol. 476, 2013, p. 012 013.
- [42] P. Bajpai and A. Varshney, "Review of different models of ferrofluid generators",
- [43] A Bibo, R Masana, A King, G Li, and M. Daqaq, "Electromagnetic ferrofluid-based energy harvester", *Physics Letters A*, vol. 376, no. 32, pp. 2163–2166, 2012.
- [44] A Bozhko and G Putin, "Thermomagnetic convection as a tool for heat and mass transfer control in nanosize materials under microgravity conditions", *Microgravity Science and Technology*, vol. 21, no. 1-2, pp. 89–93, 2009.
- [45] Golla, <http://www.ijmetmr.com/olaugust2015/GollaNagaJogaRao-JNagaraju-91.p>
- [46] S. A. Suslov, A. A. Bozhko, G. F. Putin, and A. S. Sidorov, "Interaction of gravitational and magnetic mechanisms of convection in a vertical layer of a magnetic fluid", *Physics Procedia*, vol. 9, pp. 167–170, 2010.

- [47] A. Bozhko, G. Putin, A. Sidorov, and S. Suslov, "Convection in a vertical layer of stratified magnetic fluid", *Magneto hydrodynamics*, vol. 49, no. 1, pp. 143–152, 2013.
- [48] E. Broda and L. Gay, "Ludwig boltzmann man, physicist, philosopher", 1983.
- [49] D. J. Evans and D. J. Searles, "The fluctuation theorem", *Advances in Physics*, vol. 51, no. 7, pp. 1529–1585, 2002.
- [50] G. Wang, E. M. Sevick, E. Mittag, D. J. Searles, and D. J. Evans, "Experimental demonstration of violations of the second law of thermodynamics for small systems and short time scales", *Physical Review Letters*, vol. 89, no. 5, p. 050 601, 2002.
- [51] J. Loschmidt, "J. sitzungsber. der kais. akad. d.w. math. naturw", 1876.
- [52] D. Carberry, J. C. Reid, G. Wang, E. M. Sevick, D. J. Searles, and D. J. Evans, "Fluctuations and irreversibility: An experimental demonstration of a second-law-like theorem using a colloidal particle held in an optical trap", *Physical review letters*, vol. 92, no. 14, p. 140 601, 2004.
- [53] G. Wall, *Exergy-a useful concept within resource accounting*. Chalmers tekniska högskola, Göteborgs universitet, 1977.
- [54] Z. Rant, "Exergie, ein neues wort fur "technische arbeitsfaehigkeit" (exergy, a new word for technical availability)", *Forschung auf dem Gebiet des Ingenieurwesens A*, vol. 22, no. 1, pp. 36–37, 1956.
- [55] H. D. Baehr, *Energie und Exergie: die Anwendung des Exergiebegriffs in der Energietechnik*. VDI-Verlag, 1965.
- [56] E. T. Jaynes, "Information theory and statistical mechanics", *Physical review*, vol. 106, no. 4, p. 620, 1957.
- [57] R. D. Robinett III and D. G. Wilson, "Collective systems: Physical and information exergies.", Sandia National Laboratories, Tech. Rep., 2007.
- [58] <http://www.daviddarling.info/encyclopedia/F/ferromagnetism.html>,
- [59] K. J. Buschow, R. W. Cahn, M. C. Flemings, B. Ilschner, E. J. Kramer, and S. Mahajan, "Encyclopedia of materials", *Science and technology*, vol. 1, p. 11, 2001.
- [60] V. Nikolaev and A. Shipilin, "On the thermal expansion of nanoparticles", *Physics of the Solid State*, vol. 42, no. 1, pp. 112–113, 2000.
- [61] A. Józefczak, T. Hornowski, and A. Skumiel, "Temperature dependence of particle size distribution in transformer oil-based ferrofluid", *International Journal of Thermophysics*, vol. 32, no. 4, pp. 795–806, 2011.
- [62] C. M. Oldenburg, S. E. Borglin, and G. J. Moridis, "Numerical simulation of ferrofluid flow for subsurface environmental engineering applications", *Transport in Porous Media*, vol. 38, no. 3, pp. 319–344, 2000.
- [63] <https://ferrofluid.ferrotec.com/products/ferrofluid-emg/oil/emg-911/>,
- [64] <https://bit.ly/2HLQ1ZZ>,
- [65] T. Kruse, H.-G. Krauthäuser, A. Spanoudaki, and R. Pelster, "Agglomeration and chain formation in ferrofluids: Two-dimensional x-ray scattering", *Physical Review B*, vol. 67, no. 9, p. 094 206, 2003.
- [66] <https://www.sigmaaldrich.com/italy.html>,
- [67] D. M. Rowe, *Thermoelectrics handbook: macro to nano*. CRC press, 2005.
- [68] S. Lee, J. A. Bock, S. Trolier-McKinstry, and C. A. Randall, "Ferroelectric-thermoelectricity and mott transition of ferroelectric oxides with high electronic conductivity", *Journal of the European Ceramic Society*, vol. 32, no. 16, pp. 3971–3988, 2012.
- [69] <https://www.electronics-cooling.com/2006/11/the-seebeck-coefficient/>,
- [70] <https://www.wikipedia.org/>,
- [71] E. Jordan and K. Balmain, "Electromagnetic waves and radiating systems, prentice hall", *Englewood Cliffs, New Jersey*, 1968.

- [72] I. Galili, D. Kaplan, and Y. Lehavi, "Teaching faraday's law of electromagnetic induction in an introductory physics course", *American journal of physics*, vol. 74, no. 4, pp. 337–343, 2006.
- [73] <https://brilliant.org/wiki/magnetic-flux-and-faradays-law-quantitative/>,
- [74] <https://bit.ly/2NvO6P2>,
- [75] <https://docs-emea.rs-online.com/webdocs/0de2/0900766b80de2e1b.pdf>,
- [76] J. S. Steinhart and S. R. Hart, "Calibration curves for thermistors", in *Deep Sea Research and Oceanographic Abstracts*, Elsevier, vol. 15, 1968, pp. 497–503.
- [77] <http://www.ni.com/pdf/manuals/375222c.pdf>,
- [78] <https://www.meerstetter.ch/compendium/peltier-element-efficiency>,